The development of tip-enhanced Raman spectroscopy for defect characterisation in graphene.

Rickman, Robert

Swansea University
Prifysgol Abertawe

The Development of Tip-Enhanced Raman Spectroscopy for Defect Characterisation in Graphene

Robert Rickman

MPhys

Submitted to Swansea University in fulfilment
of the requirements for the Degree of Doctor of Philosophy

2013

ProQuest LLC.
789 East Eisenhower Parkway
P.O. Box 1346
Ann Arbor, MI 48106 – 1346

Abstract

Tip-enhanced Raman spectroscopy (TERS) is a scanning probe technique that utilises a confined, evanescent field at the tip apex to conduct optical characterisation of a surface at length-scales below the diffraction limit. This thesis details the development of a new TERS system based upon a shear-force scanning probe microscope (SPM) which sits atop an inverted microscope configured for bottom illumination geometry and coupled to a Raman spectrometer. The system has been optimised for use with solid silver probes and 532 nm illumination.

Measurement procedures, automated scripts and data analysis software have been developed that allow reliable alignment of the tip; complex automated mapped measurements; and post processing which produces visual summary sheets to facilitate rapid review of a TERS experiment. Enhanced TERS spectra have been demonstrated on ultra-thin Rhodamine 6G films, self assembled monolayers (SAM) of thiophenole molecules, ultra-thin graphitic films and on multilayered graphene. Improvements in fabrication and alignment procedures have reduced the setup time between fabrication and approach to 20 minutes and improved the reliability of TERS tips with $\sim 50\%$ of tips demonstrating TERS activity.

Using TERS, heightened defect sensitivity was observed on graphene edges, folds and overlapping regions. The TERS contrast of the defect induced D band was ~ 7.5 times the contrast of the graphene G band. Calculations show that the phonons correlating to the D and G bands interact differently with the enhanced TERS field and that the for certain defect types the D band experiences greater enhancement. Defects play an important role in tailoring the electronic and chemical properties of graphene which is key to the development of graphene based devices. The localised structural and spectral information makes TERS a highly promising tool for the characterisation of defects in graphene. This work demonstrates the potential of TERS for this exciting and important application.

Declarations

This work has not previously been accepted in substance for any degree and is not being concurrently submitted in candidature for any degree.

Signed. .....(candidate) Date. 5/2/14

Statement 1:

This thesis is the result of my own investigations, except where otherwise stated. Where correction services have been used, the extent and nature of the correction is clearly marked in a footnote(s). Other sources are acknowledged by explicit references. A bibliography is appended.

Signed. .....(candidate) Date. 5/2/14

Statement 2:

I hereby give consent for my thesis, if accepted, to be available for photocopying and for inter-library loan, and for the title and summary to be made available to outside organisations.

Signed. .....(candidate) Date. 5/2/14

Contents

Acknowledgements

This thesis would not have been possible without the continued support, advice and expertise of my supervisor Dr Peter Dunstan. His enthusiasm, commitment and guidance has provided constant motivation to progress the project and develop my own scientific expertise and interests. I am sincerely grateful to Peter for furthering my love of science and making the PhD a thoroughly enjoyable and rewarding experience.

I would like to thank all members of staff in the Physics Department who have been highly supportive and made Swansea University an exciting, dynamic and productive place to work. Particular thanks goes to the technical personnel, namely Julian Kivell, Hugh Thomas and David Payne, for their assistance throughout this project.

My thanks goes to all the PhD students that I have had the pleasure to work with. Special thanks goes to Jonathon Lloyd whose work this thesis builds upon and who has provided invaluable advice around the more technical aspects of this project; Adam Williams, Kate Wellsby and Gregory Burwell for many helpful discussions in the lab; Timothy Mortenson for his wit and assistance with code; Mark Round for dealing with my theoretical shortcomings; and Adam Deller for combining physics discussions with lessons in the hydrodynamics of a closeout.

I would like to thank my family for their continued support and my wife, Kate, for her ongoing patience, enthusiasm and encouragement particularly at the latter stages of this project where the end has been in sight but never quite in reach.

I would finally like to acknowledge the EPSRC for funding my PhD studentship and The Centre for NanoHealth which has provided equipment and support. The Centre of Nanohealth is funded by the European Regional Development Fund via the Welsh European Funding Office.

Chapter 1

Introduction

1.1 Light

Light has been of absolute, fundamental importance for the development of life, intelligence and a vast amount of diverse and magnificent creatures on this planet. Light from the sun maintains a climate warm enough to sustain the chemical reactions that facilitate our existence. 3.7 billion years ago, when the origins of life began to evolve, cyanobacteria developed the ability to capture photons and use the energy to split water and carbon dioxide to produce its own useful energy source for cell function. From here on organisms became sensitive to light to optimise photosynthesis then later gained the ability to focus it, using a lens, enabling competition. Sight became a key tool in the battle between predator and prey and ultimately survival.

In the modern world manipulating light with lenses and mirrors has enabled us to understand structures much smaller than can be seen by the eye alone and at the other end of the scale far into the depths of space. This has allowed us to learn the mechanics of the universe we live in, to comprehend our origins and to exploit the physical rules of materials, structures and organisms. Understanding these physical laws has enabled the development of a staggering diversity of technological innovations that impact all aspects of our life.

This thesis is based in the field of nanotechnology, a field that has grown

rapidly in the last decade presenting numerous advances in computing, sensing, energy and healthcare amongst many others. Nanotechnology emerged in the 80's when key tools began to be developed to manipulate and image structures on large molecular length scales right down to the single atom.

The quantum mechanical rules of propagating light, however, do not allow access to these small length scales optically since it is forbidden by the uncertainty principle at what is known as the diffraction limit. Pohl et al. [1984] demonstrated for the first time, with scanning near-field optical microscopy (SNOM), that optical imaging could be achieved on nano-meter scales by extending the optical collection and illumination into the evanescent, non propagating regime. This exploits a loop hole in the uncertainty principle that opens up momentum space and so allows greater certainty in the position of each photon. The available optical resolution is extended to well below the diffraction limit as a result.

The cost of this trick is that the techniques required to access these non-propagating, evanescent fields present considerable technical challenge. Progress has been slow particularly by comparison to other techniques such as atomic force microscopy (AFM) which, despite having been conceived at a similar time, have now become entirely commonplace methods of imaging on the nanoscale. The technique explored in this thesis is tip-enhanced Raman spectroscopy (TERS). This technique combines the high spatial resolution of scanning probe microscopy (SPM) with the rich optical information provided by Raman spectroscopy. Light is coupled to the SPM probe which creates an enhanced, and crucially, a highly localised evanescent field at the tip apex. This enables the collection of optical measurements on length scales of 10's of nm's.

1.2 Raman

The core optical technique utilised in this work is Raman spectroscopy. The Raman effect was discovered by Raman [1928] for which he won the Nobel prize for Physics in 1930, becoming the first Indian to be awarded it. Raman spectroscopy is a spectroscopic technique that analyses the shift in energy of

light following inelastic scattering with a sample. The sample is illuminated by a focused monochromatic laser beam, light scattered by the molecules or crystalline structure at the laser focus is collected by an objective and spectrally analysed. This gives a unique and characteristic fingerprint that describes the chemical and physical nature of the sample.

The energy level diagram presented in Figure 1.1 shows three scattering mechanisms for photons interacting with matter. In all cases the incident photon first excites a short lived, virtual energy state. For Rayleigh scattering, which is an elastic scattering mechanism and the most prevalent, the virtual energy state relaxes back to its original state and the photon is scattered with no change to its energy. Stokes scattering on the other hand is inelastic and the molecule relaxes back to a higher vibrational energy state. The photon loses some energy in this case, which manifests itself as a detectable shift in its wavelength.

The Stokes scattering process imparts energy on the molecule leaving it in a higher vibrational state. These excited states correspond to particular vibrational modes of the molecular bonds which can include stretching modes, rotational modes and breathing modes in a molecule or phonons (lattice vibrations) in a crystalline structure. The intensity of Stokes scattering generated by each of these modes is measured by a spectrometer to produce a spectrum. The spectral peaks therefore inform us of the bonds present along with other physical properties of the molecular or crystalline structure such as orientation and stress.

The final scattering mechanism is anti-stokes scattering which is the inverse of Stokes scattering. The molecule starts in a high vibrational energy state and the scattering of a photon causes it to relax to a lower state. This means that the photon gains energy, again the scattering can be spectrally analysed however this process is weaker than Stokes scattering.

Both Stokes and anti-Stokes are examples of Raman scattering. For the purpose of this work we will only be considering Stokes shifted light and this shall be assumed whenever the term Raman is used. Raman provides a wealth of information and is a powerful technique that has many applications. Raman measurements can be conducted on a standard optical microscope that

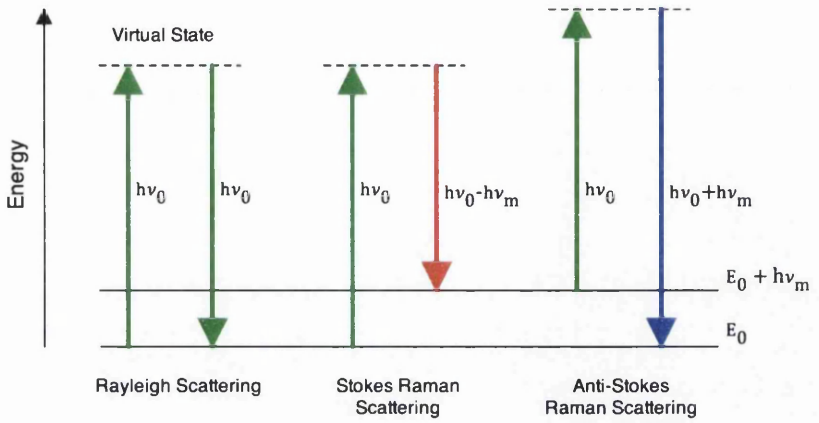

Figure 1.1: Energy level diagram depicting photon scattering mechanisms. Rayleigh scattering is an elastic process where the energy of the scattered photon remains unchanged. Stokes and anti-Stokes Raman are inelastic scattering processes where the scattered photon looses or gains energy, respectively, to vibrational modes ($h\nu_m$) of the molecule.

has been adapted to allow focused laser illumination at the sample and that incorporates a return path that directs the scattered light to a spectrograph. As a result it is an accessible technique that is cheap, quick and readily used in both material and biological sciences. We will see however that it is not always a clear cut technique that will produce a discrete or unambiguous outcome. Interpretation of Raman spectra can be challenging, measurements must be designed and samples chosen that take advantage of the strengths of the technique.

This thesis presents the development and characterisation of a new system that extends the capabilities of Raman to spatially localised measurements that are below the diffraction limit. TERS measurements have been successfully conducted on molecular monolayers and on ultra-thin crystalline films. We will discuss how TERS lends itself to high resolution optical characterisation of a sample and how this fits in as a complimentary technique to other nanoscale forms of imaging such as scanning probe microscopy (SPM) and scanning electron microscopy (SEM).

1.3 Graphene

The practical application of this project has been to demonstrate TERS as a suitable tool for the characterisation of defects in graphene. The aims of the project have needed to strike a balance between trying to understand, improve and optimise our technique whilst also exploring this exciting application.

Graphene is a remarkable material which posseses a range of unique properties. The isolation of Graphene by Novoselov [2004] sparked a large amount of experimental interest. The potential applications of this material are vast and if its properties can be fully controlled and exploited it will pave the way for some incredible devices. We have chosen it as one of our prime materials for three main reasons. Experimentally it is flat, easy to scan and at first glance has a strong Raman signature, although as will be discussed later this is not strictly be the case for TERS since the planar symmetry leads to only weak enhancement of the in-plane vibrational modes. A significant amount of the early TERS work was carried out on carbon nanotubes (CNT's) and so it is a sensible progression to look at graphene from which CNTs are derived. Finally, controlling the electronic properties of graphene is of huge importance for making devices. One of the ways that this can be achieved is by carefully engineering lattice defects into the crystalline sheet or ribbon. TERS presents a very powerful tool for studying these nanoscale defects and so could potentially make a considerable contribution to the electronic engineering of graphene.

1.4 Thesis Outline

The progress and success of this work can be split in to two strands. The first is the development of a new TERS system from non-operational to achieving successful and repeatable TERS enhancements on multiple samples. Progress includes the development of a number of software solutions to enable complex measurements and rapid, bulk analysis. The second strand of success is the application of TERS to defect characterisation in Graphene where we have demonstrated preferential TERS enhancement of the defect peak. We return

to the subject of Graphene throughout the thesis since it is this sample we have in mind when optimising the technique and designing procedures and protocol and it is this application which represents a new contribution to the field of material science.

The relevance, fabrication and optical characterisation of graphene is reviewed in Chapter 2. This sets the scene for the experimental developments that have been undertaken and presented in this thesis. A detailed discussion of the Raman modes of graphene is presented which forms the basis for our understanding and interpretation of the TERS results on ultra-thin graphite films and multilayered graphene presented in Chapter 8.

Chapter 3 explores the theory and background behind TERS. This details a mathematical description of the optical field using the angular spectrum representation and looks at how the diffraction limit is broken by introducing near-field components. We look at how the optical field at the tip can excite a surface plasmon resonance and the factors that determine the magnitude of the enhanced field at the tip apex. Understanding the mechanisms that produce a localised EM field and the nature of this field becomes important in both choosing how to optimise the optical side of our system and providing logical explanations for the preferential TERS enhancement of lattice defect states that we have observed for graphitic films.

The development and details of the TERS system are discussed in Chapter 4. The developments of the SPM are presented first, we discuss how feedback sensitivity has been achieved when operating in shear-force mode; reliable distance control is vital to ensure that the sample is correctly positioned in the enhanced field at the tip apex. The second half of the chapter considers the optical developments that have been implemented to improve beam conditioning at the focus and to obtain better collection efficiency. Aspects of tip fabrication are also included to show how procedures have been adapted to reduce the time between tip fabrication and TERS measurements and optimised to achieve good tip reproducibility.

Chapter 5 describes the methods and procedures that are employed when undertaking a TERS measurement. This presents the final optimised procedure that was developed and adapted over the course of the project.

Chapter 6 presents the software developments that have been achieved as part of this work. Software has become a substantial part of the system development and has enabled reliable and complex measurements to be undertaken. The chapter looks at the software solution we have developed to collate data from the non-integrated software packages that run the SPM and the Raman systems. Bulk processing software is demonstrated that undertakes a number of processing steps and produces a visual output that presents the spectral data in the context of the SPM topography images allowing rapid review of large mapped measurements.

The first results chapter is presented in Chapter 7 and looks at TERS enhancements on molecular films. The first sample is a thin film of Rhodamine 6G in both gap-mode (on gold) and non gap-mode (on glass) configuration. Rhodamine 6G is a responsive dye molecule that has produced modest enhancements. The homogeneity of the surface allows measurement procedures to be easily tested. The second half of the chapter looks at TERS results from a self assembled monolayer of thiophenole molecules when operating in gap-mode configuration. Thiophenole is non resonant and has a weak Raman cross section. Enhanced data was successfully obtained on this sample and demonstrates the sensitivity of our system. Alongside standard TERS measurements an alternative wavelength and tip design are trialled. The origins of temporal fluctuations that can be observed in TERS measurement are also discussed.

The second results chapter, Chapter 8, demonstrates the sensitivity of TERS to defects on graphitic films. There are two main samples of interest. The first is an ultra-thin HOPG film. The second is of multilayered graphene. We observe that the D band in graphene is more sensitive to the enhanced field and exhibits greater enhancement than the G band. We conduct calculations to show that this cannot be explained by the difference in optical volumes between the small spatial extent of defects which produce the D band and the G band which originates from the entire volume of the graphitic lattice illuminated by the evanescent field. We conclude that the increased sensitivity to defect states in graphene, leading to preferential enhancement of the D band, must result from a fundamental difference in the optical interaction.

The final chapter, Chapter 9, discusses the strengths and successes of the project and evaluates the shortcomings of the system. An outlook is presented that details a roadmap for future development. This again falls into two categories; firstly how to overcome the remaining hurdles that are presented by the TERS instrument and secondly how to take forward the success that has been presented in this work conducting TERS on graphene.

Chapter 2

Introduction to Graphene

2.1 Allotropes of carbon

Carbon is a tetravalent non metal that has 4 electrons capable of forming covalent bonds. It is able to form very long, stable chains of C-C bonds whilst still readily bonding with other elements which makes it the key building block for organic compounds and ultimately the basis for all terrestrial life. It is for this same reason that it is also of great interest to material scientists. C-C bonds are very strong, allowing certain carbon allotropes to be among the strongest and hardest materials in existence. Carbon's ability to bond with itself via up to 4 covalent bonds allows a diversity of remarkable, fully carbon based, structures to be formed. Common allotropes of carbon are graphite, amorphous carbon and diamond. However since 1980 there has been much research effort surrounding more exotic allotropes including carbon nanotubes and 'Buckyballs' (Buckminster fullerenes). These consist of a sheet of hexagonally ordered sp^2 hybridised carbon atoms that are seamlessly rolled to form hollow tubes or, with the addition of pentagons, balls, as seen in fig 2.1. They have found application in electronics [Avouris et al., 2007], batteries [de las Casas and Li, 2012], composites [Ajayan and Tour, 2007], solar cells [Hoppe and Sariciftci, 2011] and drug delivery [Bakry et al., 2007] amongst many others. The unrolled 2D sheets of carbon atoms, which are called graphene, were not however isolated and identified until 2004 when

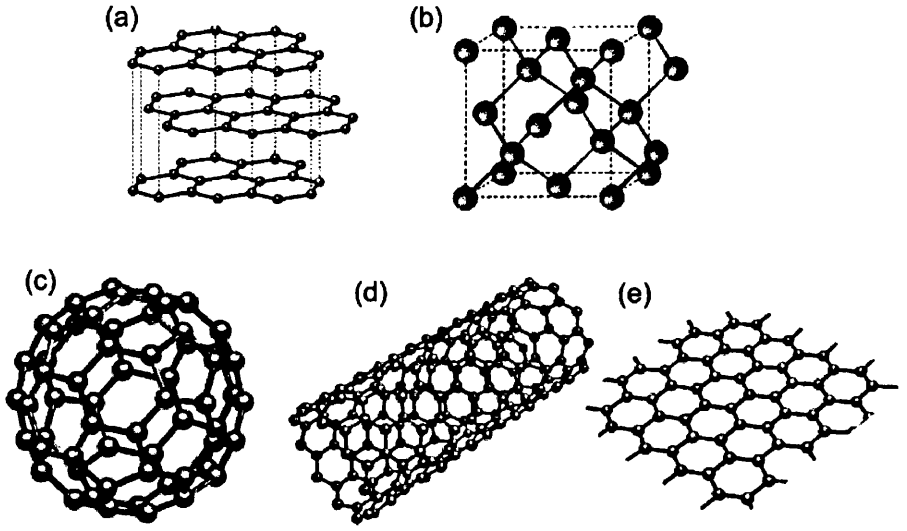

Figure 2.1: Image showing allotropes of carbon: a) Multilayered A-B stacked graphene; b) diamond; c) Fullerene (C_{60}), otherwise known as a 'bucky ball'; d) single walled carbon nanotube; and e) single layered graphene. [Scarselli et al., 2012]

scotch tape was used to exfoliate graphite and deposit a single monolayer lattice of carbon atoms onto a substrate [Novoselov et al., 2005]. Graphene was the first stable 2D crystal to be isolated and its discovery went on in 2010 to win the Nobel prize [Novoselov, 2004]. This incidentally was the second Nobel prize for carbon allotropes, as the 1996 Nobel prize for chemistry was awarded for the discovery of fullerenes [Kroto et al., 1985].

The class of carbon allotropes based upon various configurations of the single layer graphene sheet are of fundamental interest to material scientist since their electronic properties are dominated by quantum confinement effects. Fullerenes and graphene flakes $< 10nm$ in x and y represent zero dimensional systems. SWNTs and thin strands of graphene $< 50nm$ wide, known as nano ribbons, represent one dimensional systems [Chen et al., 2007] and the unrolled graphene result in a two dimensional system [Terrones et al., 2010]. These graphene based allotropes can feature properties such as ballistic conduction, tuneable metallic or semi-conducting behaviour and high electron mobility. The material also exists in 3D in the form of graphite which consists of many stacked layers of graphene which are held by weak van

der Waals forces. The layers thus come apart easily and it is characterised as a soft material despite the strong bonds in the graphitic lattice. As such graphite is highly anisotropic and its properties remain dominated by the planar symmetries. The unique electrical properties of single-layer graphene are lost in the bulk 3D material.

The melting temperature of thin films was experimentally shown to decrease rapidly with the decreasing thickness of the film and as such it was thought that due to thermal fluctuations the films would become unstable, disintegrate and lose their long range order at thicknesses below 10's of atomic layers making single layered crystals impossible at room temperature. This work was first undertaken by Landau and Peierls over 70 years ago, Mermin [1968] followed this up with a proof that long range crystalline order could not exist in 2D crystals. The discovery of graphene was thus unexpected. Shortly after it was identified other 2D crystals were isolated including $BN, MoS_2, NbSe_2$ and $Bi_2Sr_2CaCu_2Ox$ [Novoselov et al., 2005]. Two-dimensional films are in fact stable as a result of crumpling effects, long range phonons and the fact they are left in a metastable state due to their extraction from bulk materials [Meyer et al., 2007]. They do not actually fully contravene the theory since these additional contributions produce a stable state that is not represented by a perfect, flat 2D crystal. It is the strong interatomic bonds that ensure that thermal fluctuations do not lead to disintegration of the crystal.

The challenging part in the manufacture of 2D crystals is not in their fabrication, since drawing with a pencil may often leave single layer material, but finding and identifying them. They are exceptionally thin and hard to locate using optical or scanning probe microscopies. It was here that Geim and Novosolelov found their critical breakthrough. By exfoliating onto a Si/SiO_2 substrate they created a system that exploits phase contrast whereby a single layer alters the optical path of reflected light sufficiently to cause a change in the interference colour as show in fig 2.2. By fine-tuning the thickness of the SiO_2 layer, single layer graphene can be readily identified in a standard optical microscope [Geim and Novoselov, 2007].

Once discovered many techniques were employed to optimise the identifica-

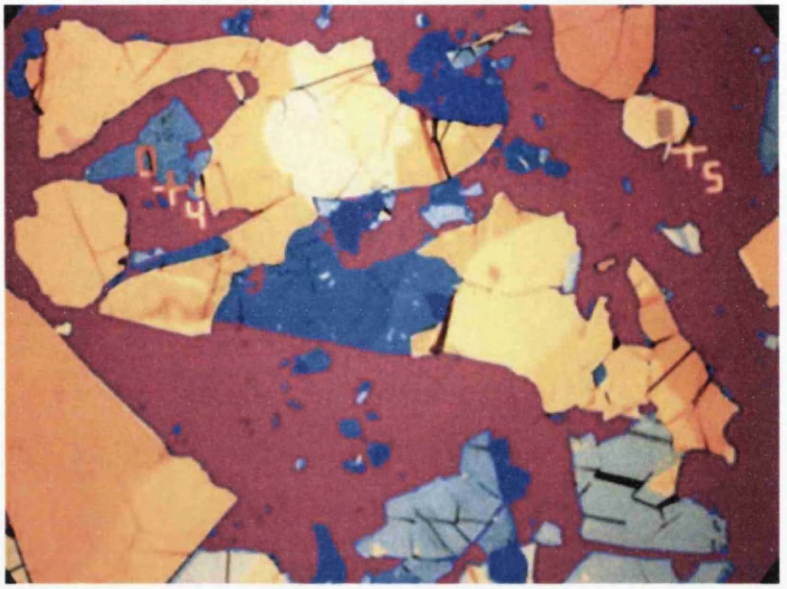

Figure 2.2: White-light image of graphitic flakes on $Si/Si0_2$ wafer, flakes range from a few graphene mono layers (purple) to flakes up to 100 nm in thickness (yellow) [Novoselov, 2011]

tion and characterisation of the material. Science had shown that single-layer graphene was stable and so further fabrication methods were shortly developed including epitaxial growth, chemical vapour deposition and chemical synthesis. The expansion of fabrication techniques has facilitated the production of graphene on various substrates [Reina et al., 2009], in liquid suspension [Zhu et al., 2009] and as suspended membranes [Meyer et al., 2007], additionally techniques have been developed to pattern it [Abramova et al., 2013], to create channels and circuits [Lin et al., 2011] and even use it as a conductive ink for printing [Kordás et al., 2006]. This chapter will go on to explore the optical, physical and electrical properties of single and multilayered graphene.

2.2 Applications of graphene

In a very short space of time a number of working prototypes have been demonstrated that show the range of potential applications for this material.

It is the transparent, flexible and conductive nature of graphene that is likely to draw the first applications in the form of touch screens and flexible circuits. Here the flake quality is less vital and cheaper techniques can be used such as chemical reduction or CVD to create large areas of coverage and where crystallite domains will not hinder the device properties.

Graphene, due to its incredibly high electron mobility of $200,000 cm^2V^{-1}s^{-1}$ (compared to $1,400 cm^2V^{-1}s^{-1}$ in silicon), draws great excitement as a potential replacement for silicon in processors. The fundamental limits of transistor size in silicon, around 5 - 7 nm, are close to being reached bringing with it an end to Moore's Law for silicon devices [Thompson and Parthasarathy, 2006]. The processor speed is restricted by the speed of the electron propagation through the material, due to its intrinsic resistance, hence the need for ever smaller transistors. Graphene can counter this since the propagation of electrons is in effect unimpeded; electrons undergo very little scattering. Graphene exhibits a resistivity lower than any other material at room temperature and 35% less than that of copper. Greater processing speeds are therefore possible without requiring such tight constraints on the transistor size. Furthermore graphene presents more favourable properties for miniaturisation than silicon with an order of magnitude decrease in channel size possible plus heat dissipation is greatly improved which is a severe limitation to silicon chips; modern processors have a large amount of 'dark silicon' where often whole cores can't be switched on as the temperature rise, due to the large power density of smaller architectures, would lead to permanent damage to the chip [Esmaeilzadeh et al., 2011]. Transistors have already been demonstrated in graphene achieving operational frequencies of 100-300 GHz [Liao et al., 2010] however they currently aren't suitable for logic applications due to poor on/off ratios. This is a consequence of the zero band-gap band structure where by a band gap of at least 0.4 eV must be created to prohibit current flow. The anomalous behaviour as a result of the Klein paradox causes an increased tunnelling probability at a potential barrier which contributes to the significant challenge of restricting current flow in graphene [Castro Neto et al., 2009].

Interesting applications in development include label free DNA sequencing

using a graphene nano-pore enabling the DNA molecule to be analysed with sub nanometer resolution [Venkatesan and Bashir, 2011]; metrology where the quantum hall effect allows graphene to be used as a standard for resistance; and supercapacitors which benefit from graphenes high conductance and chemical resistance. The optical absorption coefficient of graphene is practically independent of wavelength making it suitable for large bandwidth photo-detectors, optical modulators and mode locked lasers [Liu et al., 2011]. Despite low reactivity it is also a favourable material for a range of chemical sensors. The electronic structure of the material mean that there are very few charge carriers flowing in the undoped material creating an incredibly low noise environment. The introduction of just a few additional charge carriers can thus produce a detectable current leading to high levels of sensitivity, single molecule sensitivity has been shown using graphene based sensors [Schedin et al., 2007]. It is possible to improve the selectivity of the sensor by functionalising the surface broadening its suitability across a range of applications, sensitivity can also be improved by introducing defects and dopants [Zhang et al., 2009]. Furthermore graphene is sensitive to strain and is able to stretch by 20% before failure making it a prime candidate for strain sensing [Zhao et al., 2012].

Scientists envisage that full integrated circuits could be fabricated from graphene. If we combine this with the fact that graphene can be used for touch screens, photo-emitters, photo-detectors, sensors and in battery/super capacitor technology it becomes clear why so much research effort is being channeled into this material. To top this off graphene is a great conductor of heat; strong; flexible; chemically un-reactive; and most importantly carbon is a highly abundant element so that once production level fabrication techniques are achieved it will most likely be far cheaper to produce than its alternatives.

2.3 Electronic properties of graphene

2.3.1 Hybridisation of the carbon atom

The electronic ground state of carbon is $1s^2 2s^2 2p^2$. The first 2 electrons fill the inner shell which is tightly bound to the nucleus and so does not contribute to chemical reactions. The 4 valence electrons occupy the outer shell where it is more energetically favourable to first fill the lower energy 2s orbital leaving 2 electrons in the 2p orbital. In the presence of other atoms however one electron is promoted from the 2s to the 2p orbital since the energy gain from a covalent bond is greater than this initial outlay. A carbon atom in the excited state thus has 4 quantum mechanical states $|2s\rangle, |2p_x\rangle, |2p_y\rangle$ and $|2p_z\rangle$.

When undergoing bonding a superposition of these states occurs known as hybridisation, the resulting hybrid states now have the same energy but differ in orientation. In graphene, graphite and CNTs the bonds are sp^2 hybridised, meaning that the hybrid states are a superposition of 1 s state and 2 p states. The outcome of which is shown by equations 2.1-2.3, the hybridised sp^2 states lie in a plane separated by 120° and form covalent σ bonds with neighbouring carbon atoms. The remaining unhybridised p_z state is unaffected by this hybridisation, the orbital lies at right angles to the plane and forms a weaker π bond. It is this π bond that dominates graphene's electrical properties when it undergoes dispersion on the formation of the crystal lattice.

$$|sp_1^2\rangle = \frac{1}{\sqrt{3}}|2s\rangle - \sqrt{\frac{2}{3}}|2p_y\rangle \tag{2.1}$$

$$|sp_2^2\rangle = \frac{1}{\sqrt{3}}|2s\rangle + \sqrt{\frac{2}{3}}\Big(\frac{\sqrt{3}}{2}|2p_x\rangle + \frac{1}{2}|2p_y\rangle\Big) \tag{2.2}$$

$$|sp_3^2\rangle = -\frac{1}{\sqrt{3}}|2s\rangle + \sqrt{\frac{2}{3}}\Big(-\frac{\sqrt{3}}{2}|2p_x\rangle + \frac{1}{2}|2p_y\rangle\Big) \tag{2.3}$$

It is hybridisation that facilitates the hexagonal symmetry of the graphene lattice. Freestanding C=C (double) and C-C (single) bonds have a length of 0.135 and 0.147 nm respectively due to the difference in bond strength. The separation between carbon atoms in a graphene lattice however is a

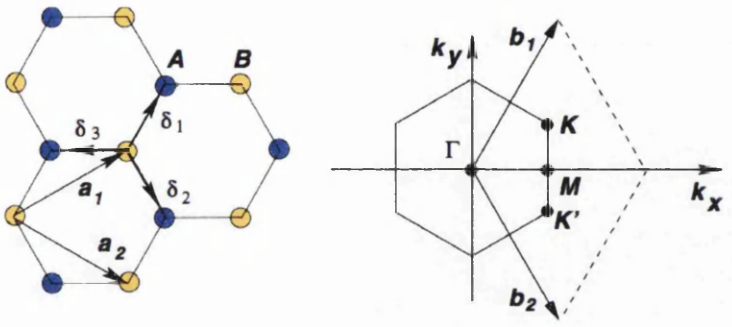

Figure 2.3: Left: The honeycomb lattice structure of graphene is defined by two triangular lattices represented by blue and yellow carbon atoms. The unit vectors are defined by a_1 and a_2. The nearest neighbour vectors are defined by $\delta 1$, $\delta 2$ and $\delta 3$. Right: The corresponding Brillouin zone Castro Neto et al. [2009].

constant 0.142 nm which is close to an average of the two and a direct result of carbons ability to hybridise enabling it to retain full hexagonal symmetry. Other allotropes of carbon take on alternative hybridisation, diamond is sp^3 hybridised and features a 3D tetrahedral symmetry; since all valence electrons are used in covalent bonds it is an insulator. Molecules such as ethene contain sp^1 hybridised carbon bonds.

Graphene's honeycomb lattice is shown in Figure 2.3a. Each unit cell of single-layer graphene contains 2 atoms. The lattice is formed of 2 triangular sub-lattices which introduces an important symmetry condition which we will see later results in the zero band gap. The corresponding Brillouin zone is shown in Fig. 2.3b which has high symmetry points at Γ, K, K' and M.

2.3.2 Band structure

Despite now no longer being the only 2D crystal to have been isolated, graphene still draws the bulk of the scientific attention. This is due to its unique electronic and physical properties. It is described both as a zero band-gap semiconductor or as a zero overlap semimetal. Both terms pointing at the same physical nature but reflecting on the varied manner in which scientists

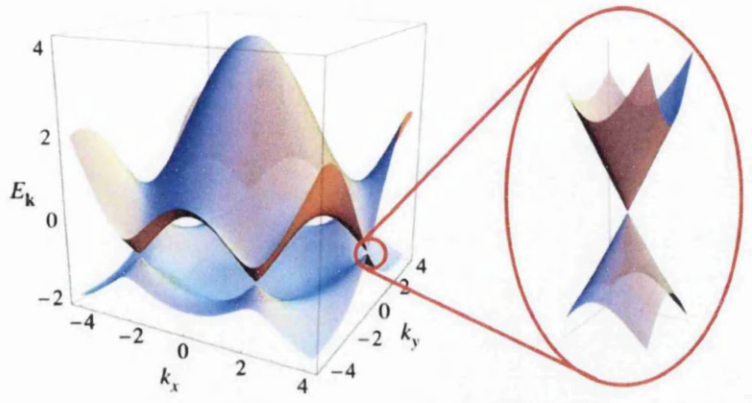

Figure 2.4: A 3D representation of the electronic dispersion in graphene. Right shows a zoomed image of the energy bands close to the Dirac points demonstrating linear dispersion. Castro Neto et al. [2009].

wish to exploit graphene's electrical properties. The concepts discussed here are based upon the tight binding approximation, a full derivation of the single-layer band structure can be found in ref [Castro Neto et al., 2009].

As already discussed, single particle electron states are separated into 2 classes π and σ. The π states are the electronically active states in graphene which lie near the fermi-level and are cylindrically symmetric in the graphene x-y plane. The π and π^* bands correspond to the bonding and anti-bonding molecular orbitals respectively and are represented by the lower (valence) and upper (conduction) bands in the electronic dispersion. The electronic dispersion of single-layer graphene is shown in Figure 2.4. At k and k', also known as the Dirac points, the valence band touches the conduction band and exhibits a linear dispersion. The linear dispersion, which is a function of momentum, implies that the speed of the electrons is constant.

In undoped graphene the conduction band is empty and the valence band is full, the fermi level sits directly between the two bands. Graphene is therefore neither a metal, which requires an overlap of the valence and conduction bands or a semiconductor, which requires a band gap. However even very low energy excitations will raise an electron into the conduction band and in single layer material the current flow can be moderated by applying a perpendicular gate

voltage. The lack of a band-gap makes it impossible to switch the current off entirely. Graphene's conductivity never falls below a minimum value determined by the quantum unit of conductance even as the density of charge carriers approaches zero. Charge carriers can be electrons or holes with their density proportional to the applied gate voltage. Concentrations can reach $10^{13} cm^{-1}$ whilst maintaining high electron mobilities of $15,000 cm^2 V^{-1} s^{-1}$. Transport is ballistic, meaning electrons can propagate without scattering, on the sub-micron scale $\simeq 0.3 \mu m$. This has been demonstrated experimentally by Novoselov [2004].

Furthermore due to the linear dispersion at the dirac points the charge carriers behave like massless Dirac fermions, they are effectively analogous to particles with zero rest mass that travel at the speed of light. States in the conduction and valence bands are in effect described by the same wavefunction. Electrons and holes are linked by charge conjugation and as such the quasiparticles maintain a chiral symmetry which is similar to the relationship between particles and anti-particles in QED. This is an exciting development for theorists since the analogous behaviour of quasiparticles in graphene to relativistic particles allows aspects of QED, that were previously challenging if not impossible to observe, to be experimentally tested in graphene.

The relativistic behaviour also introduces effects such as the Klein paradox whereby the electrons have an increased probability of tunnelling through a potential barrier compared to their non-relativistic equivalents. This can be seen as reduced backscattering since massless relativistic particles always move with constant velocity and backscattering requires the velocity to pass through zero. This unimpeded tunnelling enhances graphene's conductivity.

2.3.3 Graphene layers

The properties of graphene are altered by the number of layers that are stacked upon each other. The most energy favourable stacking geometry, and hence most common, is A-B Bernal stacking where each carbon atom lies at the centre of the hexagonal ring below it. Layers are held together by

weak van der Waals forces and feature a stacking height of $0.335nm$ per layer [Obraztsova et al., 2008, Pimenta et al., 2007]. The underlying electronic structure is sensitively dependant on the number of layers N and the stacking regime as demonstrated in Fig 2.5a. Beyond 10 layers the properties are indistinguishable from bulk graphite. Moving to few or multilayered material widens the potential applications of graphene since the altered band structure can be exploited depending upon the specific requirements of the application.

Bi-layer graphene is the only known semiconductor with a gate tuneable band-gap. A band gap can be opened by altering the symmetry between the layers by applying a voltage across them. This breaks the equivalence between layers, hence influencing the electronic structure. Gaps of up to 0.5eV can be opened. This is currently limited by the quality of the bi-layer samples. The band-structure for biased and unbiased bi-layer graphene can be seen in Figures 2.5a and 2.5b respectively. The additional bands in the band structure occur due to the increased complexity of the unit cell which now features 4 atoms. Hopping can occur not only between the sub-lattices but also between the layers causing the electronic branches to split into two components. The symmetry is however maintained between electron and holes ensuring the electronic spectrum is symmetric about the x axis.

By adding another layer to produce tri-layer graphene the electronic properties become that of a semimetal with a gate tuneable band overlap, this progression is seen in Figure 2.5a. Conductivity can thus be increased through application of a gate voltage perpendicular to the graphene plane. Each increase in the number of layers requires additional hopping parameters to be introduced to account for coupling between the π orbitals in the different layers. This results in the evolution of the band structure. It is this, as we will see later, that enables accurate identification of the layer number N since it directly influences the Raman signature.

2.3.4 Epitaxial graphene

It is worth noting that there are other mechanisms that can cause significant variation in the electronic properties of graphene samples. Mechanical exfoli-

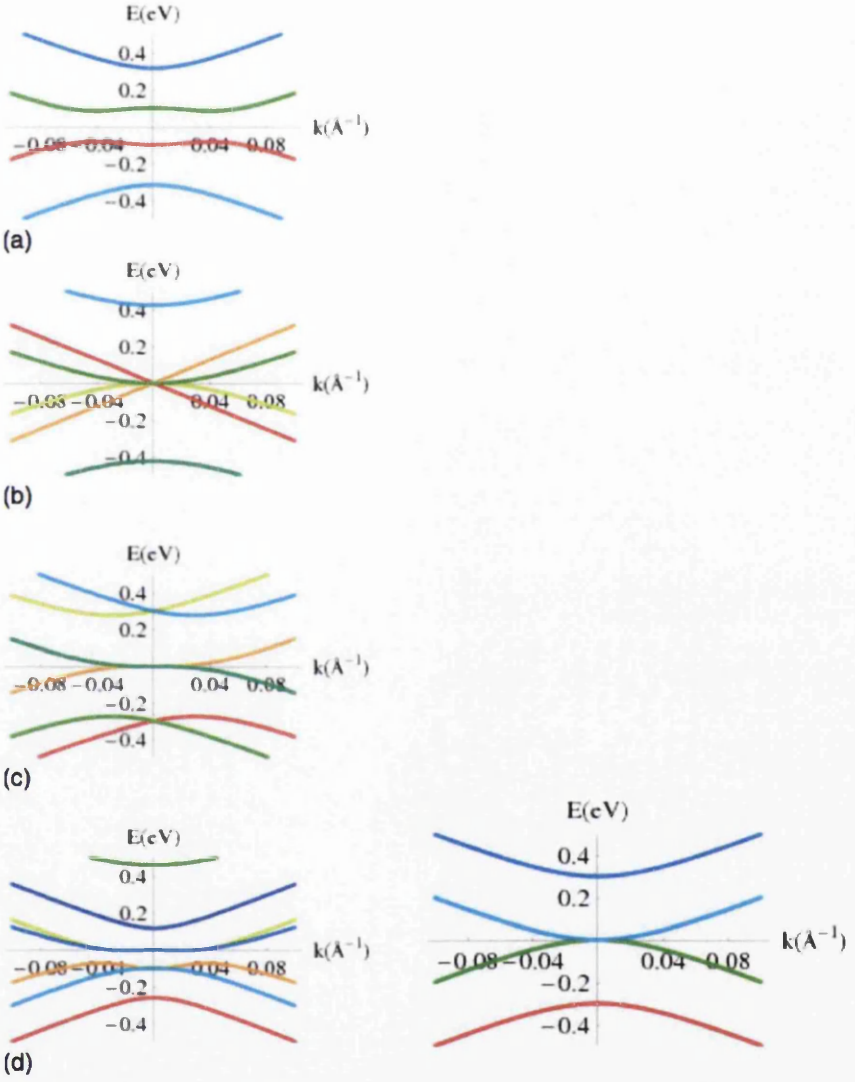

(a) a) Biased bilayer, b) trilayer (Bernal), c) trilayer (orthorhombic), d) 4 layer (top and bottom layers are shifted in energy 0.1eV relative to the middle layers)

(b) Unbiased bilayer

Figure 2.5: Electronic band structure of multilayered graphene configurations Castro Neto et al. [2009].

ation produces the highest quality flakes however this process is limited to small flake sizes and a significant effort is required to find them. We have already come across alternative techniques to fabricate graphene that may be better suited for high-yield production of which epitaxial growth is the most common. This process creates mono-layers of graphene on the surface of SiC. By annealing the SiC crystal at high temperatures in vacuum conditions, the silicon from the top layers desorbs leaving behind graphene flakes. The flake quality and number of layers can be controlled by tuning the temperature and heating time and by selecting the SiC face to be used. It is here that we see pronounced variation in the electronic properties. Growth from the carbon face produces few layers but causes a low electron mobility compared to growth from the Si face which produces thicker, metallic flakes with a high mobility [Hass et al., 2008].

These observations reveal that the SiC forms an integral part of the whole epitaxial graphene system. The bottom layer of graphene is tightly bound to the upper SiC face, it is known as the buffer layer and expresses no π band. This layer is bonded to the Si atoms and is sp^3 hybridised. The distance between this layer and the SiC face has been determined as $0.20nm$ and $0.17nm$ for the Si and C terminated faces respectively which are both far smaller than the the inter-layer separation of $0.34nm$ found in normal crystalline graphene [Varchon et al., 2007]. Also of interest is the fact that additional sheets in multilayered epitaxial material exhibit a larger than usual inter-layer separation of $0.39nm$. This results in a charge imbalance between the sheets which produces the modification in electron mobility stated above. Interaction with the bulk SiC substrate causes charge transfer which results in a heavy electron doping in the first layer whilst subsequent layers remain more or less uncharged.

Experimentally the top layers have been shown to express increased amounts of rotational disorder [Meng et al., 2012], this combined with the increase separation leads us to believe that multilayers of epitaxial graphene behave more like weakly interacting stacked mono-layers. A final observation of epitaxial graphene is that the electrical properties do not show strong homogeneity. Local fluctuations are thought to occur due to topographic variations

originating from defects, terraces and lattice reconstructions which can cause local differences in the doping. These deviations in the electronic properties mean that the dependance of the Raman signature on the layer number follows different rules on epitaxial graphene than on exfoliated material.

2.4 Raman

Since the initial discovery of graphene Raman has been used as the principle characterisation tool. Raman can rapidly determine the layer thickness and the crystalline quality. As we will see in this section there is a wealth of knowledge that can be determined from the graphene spectrum including amongst others: crystallite size, defects, chemical impurities, the optical band gap, doping, strain and edge type. It is thus an incredibly useful tool for characterising the material. Carbon based materials have a large Raman cross-section and give a strong spectral response allowing for quick acquisitions and low laser powers. There is no need for an overly sophisticated Raman system making this a very accessible technique for material classification.

2.4.1 Raman modes of graphene

The Raman spectra of graphite and graphene can share four main peaks D, G, D' and G' at $1350cm^{-1}, 1600cm^{-1}, 1620cm^{-1}$and $2700cm^{-1}$ respectively. Typical spectra, for a single layered graphene lattice containing defects, are shown in Figure 2.6. The D and D' peaks indicate the presence of disorder in the graphene lattice. The G peak is a signature of all sp^2 carbon and originates from the $C-C$ stretching mode. The G' peak can be used to determine the number of layers in the graphene sample. The intensity ratio of I_D/I_G is often used to quantify defect concentrations and domain size.

The phonon dispersion for single layer graphene is shown in Figure 2.7. The unit cell is unaltered from earlier discussions and contains 2 carbon atoms. The phonon dispersion consists of 6 phonon branches split into 3 acoustic (A) and 3 optical (O) modes. The branches are then defined by their vibrational orientation. The out of plane (oTO, oTA) branches oscillate

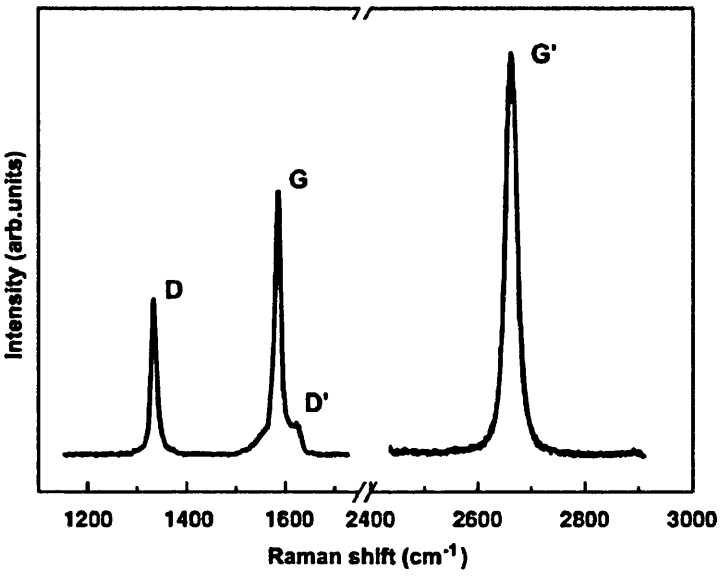

Figure 2.6: Typical Raman spectrum of monolayer graphene with lattice defects. The D, G, D' and G' bands are highlighted for clarity [Malard et al., 2009]

perpendicular to the plane whilst the longitudinal (iLO, iLA) and transverse (iTO, iTA) oscillate in plane with the transverse and longitudinal directions defined relative to the direction of the nearest carbon atom which in this case sits on the other sub lattice. A full discussion of the origin of each of the graphene Raman bands will be undertaken in this section, the processes involved are depicted schematically in Figure 2.8.

G band

At the zone centre (Γ point) the iLO and iTO modes are degenerate and belong to the E_{2g} symmetry group and as such are Raman active. The degeneracy does not exist away from the Γ point. This mode is a first order process, as illustrated in Figure 2.8, which gives rise to the G band at $1582cm^{-1}$ and is present in all structures containing sp^2 hybridised carbon. The mode describes vibrations between sub lattice A against B and hence represents the $C - C$ stretching mode of the single carbon bonds.

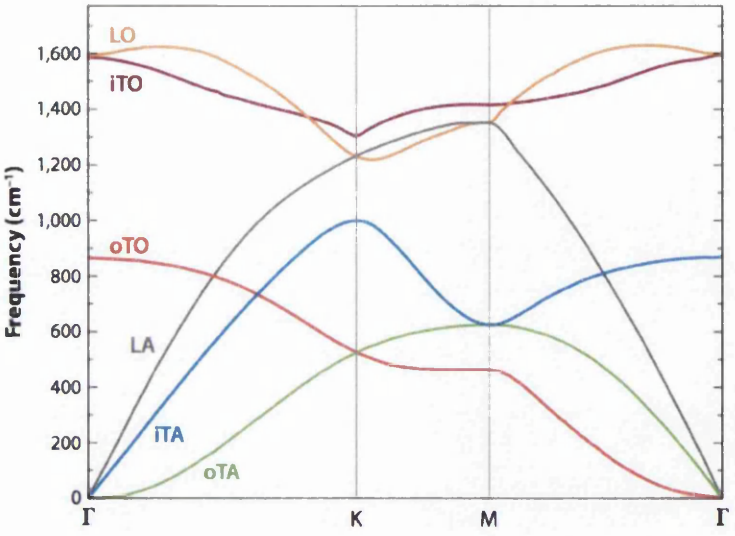

Figure 2.7: Graphene dispersion showing the LO, iTO, oTO, LA, iTA, and oTA phonon branches [Dresselhaus et al., 2010].

D, D' and G' bands

The D and the G' bands are determined by phonon modes around the K point and involve the iTO phonon branch which is non-degenerate in this region of the Brillouin zone. Both are inter valley double resonance processes since they connect neighbouring K and K' points. The mechanism involves an electron with wave vector k absorbing a photon whereby the electron is scattered by a phonon or a defect with wave vector q to the circle surrounding the K' point. The resulting wave vector is $k+q$. The electron is subsequently backscattered to the K point where it re-combines with a hole and emits a photon. It should also be noted that this Raman process is equally valid for the scattering of holes.

In a double resonance processes there are 3 scattering events however 2 resonance conditions must be met. For the D and G' band the intermediate $k+q$ state and either the initial or final k state must be a real electronic state. This links the phonons and electrons in the graphene phonon dispersion and, as we will see with multiple layers, the G' peak is highly dependant on the underlying electronic structure at the Dirac points. Additionally these

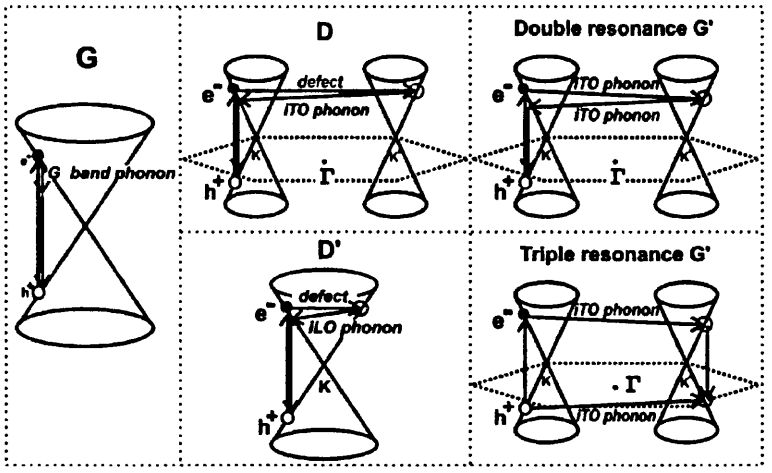

Figure 2.8: Phonon scattering processes that occur for each Raman band in single layered graphene [Malard et al., 2009].

resonance conditions cause both the D and G' bands to be dispersive since the initial excitation is dependant on the energy of the incident photon.

The D band consists of one elastic scattering event by defects in the lattice and one inelastic scattering event due to the emission or absorption of an iTO phonon. It is activated when structural disorder is present in the lattice and represents the ring breathing A_{1g} vibrations of sp^2 rings. The D' band is a double resonant intra valley process that connects two points within the same circle at K or K'. It involves scattering by a defect and an iLO phonon and so is activated by the presence of lattice defects. The G' band is likewise a double resonant process and requires 2 inelastic scattering events creating 2 iTO phonons. It is an inter valley process that connects points in circles around 2 inequivalent K and K' points in the first Brillouin zone.

Identification of layer number

In single layer graphene the G' peak originates from a triple resonant process as a result of the symmetry between the π and π^* electronic bands about the fermi-level at the Dirac points K and K'. This occurs when instead of the electron being scattered from K' to K by a phonon with wave vector $-q$ a phonon with wave vector $+q$ scatters the hole to a resonant state

at K'. Recombination will occur at K' and for this process to occur the scattering of both the electron and hole must be resonant and the initial electron hole generation must also be resonant. The triple resonant process in single-layer graphene may well explain the increased intensity of the G' peak for single-layer material.

In bi-layer graphene the phonon branches split into two corresponding to the in phase (symmetric) and out of phase (anti-symmetric) vibrations of the atoms in each layer. This is significant as it alters the resonant states available in the G' scattering mechanism which alters the line shape of the G' peak. The additional scattering transitions are shown in Figure 2.9. Due to the splitting of the electronic structure around the k points there are now 4 available scattering mechanisms to take into account all possible transitions between the π branches. The G' peak thus contains 4 contributions as opposed to the single peak that is generated by mono-layer graphene.

in tri-layer graphene the peak shape requires the fitting of 6 lorentzians due to a further splitting of the electronic structure. This demonstrates the clearly defined progression of line shape between single, double and triple layer graphene. When analysing the shape of the G' peak the peak is fitted with lorentzians with a FWHM of $24cm^{-1}$ based upon the width of the peak in single layer graphene. Sticking to this rule allows the number of transitions to be measured by the number of lorentzians it takes to match the G' line shape.

Four layer graphene marks the turning point towards bulk properties. The G' peak in this instance is fitted with 3 peaks. The G' spectrum for HOPG is split into 2 peaks with the larger wavenumber peak featuring a greater intensity. The progression in the line shape with layer number of the G' peak is shown in Fig 2.10. What Raman struggles to do is to accurate identify the layer number when it exceeds 3 layers. As such graphene is usually defined as single layer, few layer or multilayer where multilayer encompasses the full range from 4 - 10 layers. 10 layers is generally considered the threshold for graphene beyond which the properties become indistinguishable from bulk HOPG.

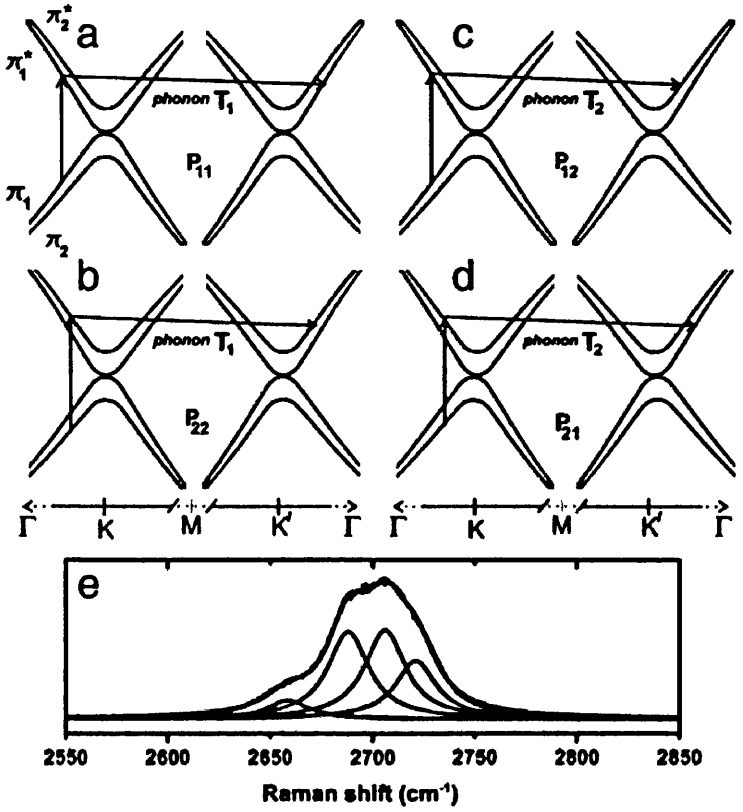

Figure 2.9: Double resonant phonon scattering events that occur in bilayer graphene to produce the broadened lineshape of the G' Raman peak [Malard et al., 2009].

2.5 Summary

This chapter has discussed the potential of graphene to supersede silicon and become the basis for a range of new, exciting electronic devices. We have also seen how Raman has become one of the primary tools for its characterisation with sensitivity to layer number and defects. It is for this reason that we have chosen to use graphene as the principle material studied in this work. The development of tools to further the understanding of graphene and tools for routine characterisation are a fundamental requirement if the material is to reach its technological potential.

The ability to tune the electronic properties of graphene has been touched

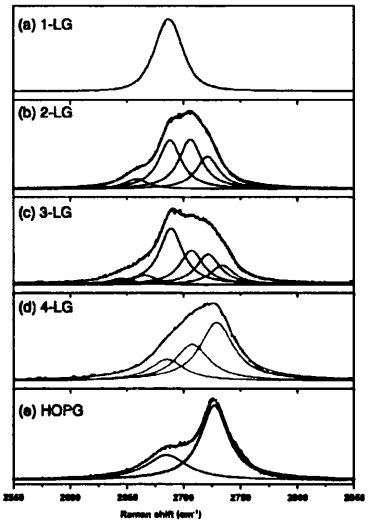

Figure 2.10: Evolution of the G' peak with increasing layers [Malard et al., 2009]

upon, as have the hurdles that need to be overcome. The most pressing challenge is to engineer methods that switch off the current flow; this is not straight forward due to graphene's zero band gap and the Klein paradox. The zero band gap requires that graphene must be physically modified to create devices, broadly there are two principle approaches. The first is to use multiple layers and apply bias to open a band gap. Heterostuctures can be produced that combine graphene with other 2D crystals which can be conductive, insulating or semiconducting this allows the bulk properties of the resulting stack to be engineered. The second approach is to utilise lattice defects. Intrinsic defects will scatter electrons and so influence the conduction and can be used both to enhance and restrict current flow and tune the sheet properties between metallic and semiconducting. Extrinsic defects can inject charge into the graphene lattice.

The focus of this work is to show that there is potential for TERS to be of use to this second approach to device engineering. Chapter 8 continues the discussion of the role of defects in graphene and presents results which demonstrate that TERS can exhibit heightened sensitivity to certain defects in multilayered graphene.

Chapter 3

Introduction to TERS

3.1 From far-field to near-field

Optical microscopy remains one of the most common techniques for the investigation of matter on the micron-scale. Nanotechnology seeks to investigate material properties at nanometer dimensions probing properties that extend from the atomic and molecular regime. Classical optical microscopy, however, is diffraction limited and so unable to reach these length scales. Diffraction effects occur when light encounters obstructions resulting in bending of its path and self interference, these diffraction effects are most prominent on length scales of the order of the fields wavelength. As a result the image of small, sub-micron, objects become broadened and blurred in high magnification systems. More pressingly objects at close separations become indistinguishable placing a fundamental restriction on the obtainable optical resolution and hindering our ability to make optical observations at length-scales below a few hundred nanometers.

In this chapter we will explore the theory leading to the diffraction limit and understand why little can be done to further improve the spatial resolution of a conventional microscope. We will also see how this does not present an absolute dead end and that physics has left a few tricks that allow us to penetrate this barrier and extend our optical measurements into the classically forbidden, nano-scale regime.

Tip-enhanced Raman spectroscopy (TERS) is one of a small number of techniques that can optically probe the nanoscale and it is the central technique investigated by this thesis. Nanotechnology requires a range of complimentary techniques in order to reach the full potential of the discipline and enable characterisation, manipulation and understanding of physical systems on these scales.

There are two dominant approaches; electron microscopy, which exploits the smaller de Broglie wavelength of high energy electrons to produce rich images and extract chemical information; and scanning probe microscopy (SPM) which uses an ultra-sharp probe that is raster scanned whilst in near-contact with the surface to build a 3D topographic image. TERS is an extension of this latter technique, it uses the positional control of SPM whilst coupling light to the surface of the metallic probe to produce a confined field at the apex that enables localised optical measurements with spatial resolution of the order of 10's of nanometers. The localised nature of the optical field requires us to operate in the near-field regime. In the near-field light is no longer propagating and decays exponentially from its source; this both opens up high resolution optical measurements and creates numerous experimental headaches. The advantage of TERS is that we can extract detailed information about the chemical molecular structure and physical properties of the sample. We will explore in this chapter the mechanisms that enable TERS and discuss the experimental challenges that are an inherent part of the technique.

3.2 Angular spectrum

The angular spectrum representation of an optical field plays a central role in this evaluation of the optical processes involved in microscopy. The angular spectrum allows any optical field to be described by the superposition of plane and evanescent waves. The plane and evanescent components relate to the far-field and near-field components respectively. Any field is therefore just an expansion of plane and evanescent waves with variable amplitudes and wave-vectors. This representation is particularly helpful when considering

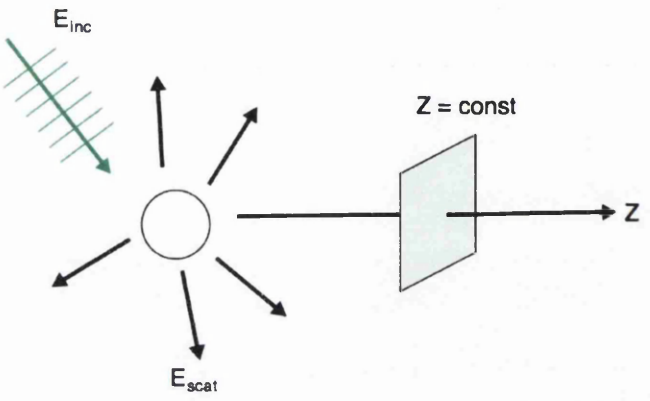

Figure 3.1: Schematic of a scattering event. In the angular spectrum representation the scattered field is analysed through a plane perpendicular to the z axis, where $z = const$. This plane is known as the image plane.

the limit of focusing or scattering of light and is hence of great benefit to the TERS discussion. The key concepts and equations are presented in this chapter; the full derivations can be found in Novotny and Hecht [2006].

The optical field at any point in space is denoted by $E(\boldsymbol{r})$ where $\boldsymbol{r} = (x, y, z)$. A scattering event is simply the sum of incoming and outgoing waves such that $E = E_{inc} + E_{scat}$. To analyse the field in the angular spectrum representation an arbitrary direction, z, is chosen and the field is evaluated in the plane where $z = const$ which is called the image plane as shown in Figure 3.1. A 2D Fourier transform is taken across this plane, shown in equation 3.1, which allows the field to be represented by the reciprocal coordinates k_x and k_y which are known as spatial frequencies.

$$\hat{\boldsymbol{E}}(k_x, k_y; z) = \frac{1}{4\pi^2} \iint_{-\infty}^{\infty} \boldsymbol{E}(x, y, z) e^{-i[k_x x + k_y y]} \, \mathrm{d}x \, \mathrm{d}y \tag{3.1}$$

An inverse Fourier transform is used to return to cartesian space.

$$\boldsymbol{E}(x, y, z) = \iint_{-\infty}^{\infty} \hat{\boldsymbol{E}}(k_x, k_y; z) e^{i[k_x x + k_y y]} \, \mathrm{d}k_x \, \mathrm{d}k_y \tag{3.2}$$

A propagation term must be introduced to describe the nature of the field in the z direction. It is derived by ensuring that the time-harmonic optical

field satisfies the Helmholtz equation (eqn 3.3). For a homogenous medium that is isotropic, linear and source free the Helmholtz equation is the primary condition placed on the field.

$$(\nabla^2 + k^2)\boldsymbol{E}(\boldsymbol{r}) = 0 \tag{3.3}$$

Where $k = (\omega/c)n$ and n is the refractive index, $n = \sqrt{\mu\epsilon}$.

This condition is met by inserting the Fourier representation of $E(r)$, equation 3.2, into the Helmholtz equation, equation 3.3, and utilising $k_z \equiv \sqrt{(k^2 - k_x^2 - k_y^2)}$. This leads to the description of the evolution of the Fourier spectrum along the propagation axis:

$$\hat{\boldsymbol{E}}(k_x, k_y; z) = \hat{\boldsymbol{E}}(k_x, k_y; 0)e^{\pm ik_z z} \tag{3.4}$$

This equation, equation 3.4, introduces the most important aspect of this derivation; the term $exp(\pm ik_z z)$ which is known as the propagator in reciprocal space and describes the nature of the propagation. The spectrum in the image plane (z = const) is equal to the field in the object plane (z=0) multiplied by the propagator therefore the purpose of the propagator is to account for the phase and amplitude changes that occur in the field on reaching the image plane. There are two solutions indicated by the $\pm$ which describe the forward and backwards propagation of the field.

The full angular spectrum representation, equation 3.5, is produced by inserting equation 3.4 into the inverse Fourier transform, equation 3.2.

$$\boldsymbol{E}(x, y, z) = \iint_{-\infty}^{\infty} \hat{\boldsymbol{E}}(k_x, k_y; 0)e^{i[k_x x + k_y y \pm k_z z]}\,\mathrm{d}k_x\,\mathrm{d}k_y \tag{3.5}$$

To be consistent with Maxwells equations the field must be divergence free such that $\nabla \cdot \boldsymbol{E} = 0$ and $\nabla \cdot \boldsymbol{H} = 0$. This restricts the k vector to directions perpendicular to the spectral amplitudes so that $\boldsymbol{k} \cdot \hat{\boldsymbol{E}} = 0$. Since the refractive index n is real, k_z can be real or imaginary which creates two variants of the propagator. The first of which allows propagation and describes a plane wave, the second of which decays exponentially along the z (propagation) axis and is evanescent in nature; this is shown by equations 3.6 and 3.7. The full

angular spectrum representation, equation 3.5, shows that the optical field consists of a superposition of all propagating plane waves and exponentially decaying evanescent waves.

$$\text{Plane waves:} \qquad e^{i[k_x x + k_y y]} e^{\pm i|k_z|z}, \qquad k_x^2 + k_y^2 \leq k^2 \tag{3.6}$$

$$\text{Evanescent waves:} \qquad e^{i[k_x x + k_y y]} e^{-|k_z||z|}, \qquad k_x^2 + k_y^2 > k^2 \tag{3.7}$$

The magnitude of the spatial frequency, k_x and k_y, correlates to the amount of spatial information that is carried by that component of the field since it details the size of the oscillation in the transverse plane. As such a plane wave travelling at a larger angle with respect to the z axis will carry more spatial information. For plane waves the spatial frequencies are limited to $k_x^2 + k_y^2 = k^2$ (limit when $k_z^2 = 0$) since the total magnitude of k is fixed. However introducing evanescent components, where k_z becomes imaginary, enables the magnitude of the transverse spatial frequencies to be increased whilst still maintaining the condition that $k = \sqrt{k_x^2 + k_y^2 + k_z^2}$. This shows that by entering the evanescent regime the available bandwidth is increased, in principle it can be infinite however the rate of exponential decay of the evanescent field is proportional to the spatial frequency creating a finite bandwidth in practice.

3.3 Spatial resolution

Traditional optical microscopy relies upon an objective lens to collect and magnify light from a sample which is later focused by a second lens to form an image. The resolving power of the microscope is determined fundamentally by the numerical aperture (NA) of the objective. The NA is defined in equation 3.8 and describes the angular range over which light is collected by the objective.

$$NA = n \sin\theta \tag{3.8}$$

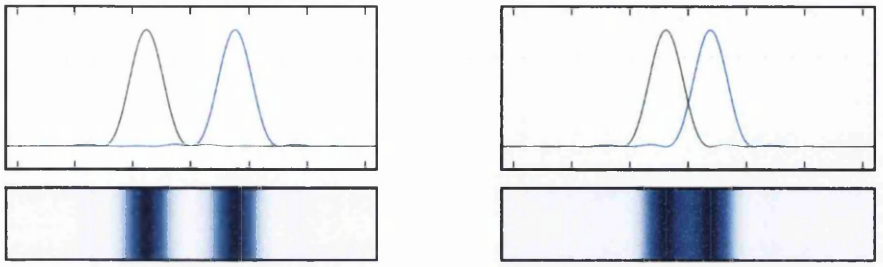

(a) Sepparated (b) Overlapping

Figure 3.2: Plots illustrating the point spread function of two point sources, top shows the intensity profile whilst the bottom represents how this might look in the microscope. a) Two separated point sources allowing the features to be resolved. b) Two point sources separated by the Rayleigh criterion, Δx, which is the limit at which the features can no longer be unambiguously identified.

Where n is the refractive index and θ is the angle between the optical axis and the collected light.

The NA determines the light gathering capacity of the objective and hence the final image resolution. Relating this to the previous discussion, the collection of higher spatial frequencies is increased by using a higher NA. There are however physical limits to the size of the NA due to imperfect optics and practical constraints such as the separation between the objective lens and the sample. A solely lens based microscope thus only collects a fraction of the scattered field and ignores completely all non-propagating components. Information carried by higher spatial frequencies is lost resulting in the collection of a reduced bandwidth of spatial frequencies. The consequence of the reduced bandwidth is that even a point source will have a finite size since there is no longer the complete set of information which is required to produce a full reconstruction; experimentally this manifests itself as diffraction. The finite size of a point source is described by the point-spread function which is a measure of the bandwidth and demonstrates the spatial broadening visible in the microscope.

The ultimate resolution is likewise limited since at small separations

PSF's will overlap as shown in Figure 3.2. The minimum resolvable and unambiguous separation is dependant upon the width of the PSF, Δx, which is the distance from the central maxima to the first minima. Equation 3.9 is called the Rayleigh criterion and was originally formulated at the end of the 19th century.

$$\Delta x = 0.61\frac{M\lambda}{NA} \tag{3.9}$$

This shows the size of the image is dependant on the NA, magnification and wavelength. Abbe and Rayleigh, who were tackling this problem, defined that the resolution limit is reached when the peak of the first objects PSF sits at the first minimum of the second objects PSF. The best possible NA is equal to the refractive index n, which for standard glass optics is $\simeq 1.5$, this fixes the upper limit of resolution at $\Delta x \simeq \lambda/3$.

For green illumination this sets a far-field resolution limit of $\sim 180nm$. To overcome the diffraction limit techniques must be chosen that selectively illuminate sub-wavelength regions of the sample. TERS facilitates this by creating a localised illumination source that is 10's of nm's in diameter thus opening up optical imaging at length scales well below the diffraction limit.

3.4 Overcoming the diffraction limit

The diffraction limit is a fundamental consequence of Heisenberg's uncertainty principle, which for photons is described as:

$$\Delta\hbar k_x \cdot \Delta x \geq \frac{\hbar}{2} \tag{3.10}$$

Where $\hbar$ = Plancks constant and k = Wavevector. The confinement of photons (Δx) is restricted by the spread of magnitude of the wavevector components, using the terminology introduced in Section 3.2 we define this as the bandwidth of spacial frequencies. This spread of wavevectors occurs when the field converges such as at a focus or from the emission of a point source.

Two points are clarified by this formulation of the problem. The resolution, or positional accuracy ($1/\Delta x$), requires the bandwidth of the spatial frequencies to be maximised hence why in conventional microscopy best resolution is achieved with a high NA objective. Secondly, by exploiting the fact that k_x can assume a maximal value equal to the total length of the wavevector, $k = 2\pi/\lambda = \sqrt{k_x^2 + k_y^2 + k_z^2}$, we can increase k_x by forcing one of the orthogonal components to take on a purely imaginary value. As has already been seen the consequence of this mathematical trick is that the wave can no longer propagate along this axis becoming evanescent in nature. Thus by only sampling the propagating far-field components of light the ultimate resolution can never be achieved. Through the introduction of evanescent components we increase the uncertainty in the wavenumber (Δk) and so we are allowed to decrease our uncertainty in the position (Δx) without contravening the uncertainty principle. This enables optical measurements beyond the classical diffraction limit. This is known as near-field microscopy since the non-propagating, exponentially decaying evanescent components must no longer be ignored.

The ultimate limit of resolution would occur when Δx was equal to a gaussian function, which represents the minimum possible uncertainty. To achieve this the full spectrum of spatial frequencies would have to be collected. By only ever being able to measure a finite spectrum of spatial frequencies we will always be working within a reduced limit of resolution and point sources will always have a finite size.

The evanescent field carries extra information however this information is typically lost to the far-field due to its rapid decay. The near-field can interact with other systems allowing access to the information it encapsulates. TERS tips act as an optical antenna in what is a two way process. The tip couples far-field propagating radiation into the near-field. It is additionally able to interact with the near-field converting the evanescent field into far-field, propagating radiation. This allows localised Raman signal scattered from the exponentially decaying near-field at the tip apex to be detected. The high levels of confinement, however, produce large divergence in the scattered signal and so the far-field optical collection remains critical to the performance

of the system.

3.5 Near-field optical microscopy

The drive to confront the challenges presented by near-field optical microscopy stem from the depth and range of information that can be obtained when probing with light. There are a host of complimentary techniques that allow nano-scale imaging. SEM, for example, utilises the small de Broglie wavelength of high energy electrons to create high resolution images. The images that can be obtained with SEM are stunning, however the measurements must be conducted in a vacuum and sample conductivity must be considered to limit charging. This restricts the biological applications; dynamic and in vivo measurements are strictly off limits to this technique. Likewise AFM can produce topographic images with near atomic resolution but offers little further chemical information about the sample. Light, with its many paths of analysis, is still advantageous since there are multiple scattering mechanisms that can be reliably studied using spectroscopy. Polarisation and temporal considerations can further improve sensitivity and selectivity. Furthermore biological mechanisms can be studied using fluorescent tagging.

Near-field microscopy has in its favour the fact that it is building upon the most common-place characterisation technique. On one machine standard far-field microscopy techniques can be conducted to isolate specific regions of interest which can then be probed in depth using the more experimentally complex near-field techniques. Optical measurements remain one of the best approaches for measuring a broad range of sample properties whilst not overly restricting the sample type and preparation.

There are two avenues that facilitate nanoscale optical imaging. The first is to have a translatable localised illumination source as is the case with SNOM and TERS. The second is to isolate single emitters under conditions where the point-spread function never, or barely, overlaps that of a neighbouring emitter. The location of a single emitter can be determined with an almost arbitrarily high precision and by considering their point-spread function a single emitter can be readily identified allowing the position of each emitter

to be retrospectively calculated.

There have been a number of techniques that have been developed to exploit this concept. Each technique requires the creation of conditions where fluorophores flash on and off such that there is a high probability that no local overlap of point spread functions occurs at any period of time. The position of each fluorophore is located using image processing and over time a full, high resolution image is compiled. The main variants of this approach are stochastic optical reconstruction microscopy (STORM) [Rust et al., 2006] which employs two laser pulses at different wavelengths. The first pulse deactivates all fluorescent molecules in the observation window by sending them to their ground state. The second pulse is weak and excites only a small proportion of the fluorophores ensuring few emissions. This process is repeated until a full image is reconstructed. Photo-activated localisation microscopy (PALM) uses partially bleached fluorophores which naturally blink on and off and which are most likely to be found in the off state to achieve the same outcome and produce images with a spatial resolution of $12nm$ [Hoyer et al., 2010].

Since no enhancement is taking place these techniques require high yield mechanisms and so are suited to fluorescence observations. Fluorescence has become a central technique within the life science toolkit and so these optical techniques are certainly useful, complimentary techniques to an already prevalent method of analysis. In our case we are interested in Raman since it facilitates label free characterisation of a sample. Raman, as discussed in Chapter 1, provides detailed chemical, electronic and structural information about a sample however it has a very small scattering cross-section requiring an optical enhancement to boost the signal and make the near-field signal detectable above the background noise.

3.5.1 SNOM

The first scanning probe based optical technique was SNOM which was theoretically postulated by Synge in the late 1920's [Synge, 1928]. The concept proposed shining an intense light source at the back of an opaque

screen containing a sub-wavelength aperture. He postulated that the light field would be confined by the dimensions of the hole and images could be produced by positioning this aperture at close proximity to the sample such that the confined light could locally interact before it had time to diffract and degrade the image. This was an almost exact description of what became scanning near-field optical microscopy (SNOM). SNOM however relies upon the coherent light emitted from a laser which weren't realised until the late 1950's and upon precise position control that requires piezo crystals and high bandwidth feedback electronics to maintain sensitive tip-sample separation. The experimental accomplishment of SNOM did not come about until the 1980's where it was first confirmed by Pohl et al. [1984]. Although, incidentally Synge's proposition was realised using microwave radiation in 1972 by Ash and Nicholls who were able to achieve a spatial resolution of $\lambda/60$. SNOM has demonstrated itself as a valuable technique showing sufficient sensitivity to facilitate single-molecule measurements and the high spatial resolution has advanced understanding of properties at the sub-micrometer scale. Applications range from single-molecule studies, thin-films, interfaces and biological samples.

SNOM probes, which consist of a metal coated tapered optical fibre with a sub-wavelength aperture, work either as a local light source by coupling laser light into the fibre and collecting the scatter using far-field optics or by illuminating in the far-field and collecting through the SNOM probe. In both cases photons are unable to propagate through the aperture and so the probe either becomes a confined, evanescent source or interrogates only the evanescent components of the sample scatter respectively. This gives high spatial localisation, a full image is produced by scanning the sample beneath the tip measuring the intensity at each point. By locally illuminating or collecting scatter SNOM has the capability of resolutions as low as $12nm$ [Betzig and TRAUTMAN, 1992]. The achievable resolution is determined by the aperture size, however its principle limitation is low optical throughput. In routine experiments a resolution closer to $50nm$ can be expected since a larger aperture is required create more sensible levels of signal. Even with the larger apertures, SNOM is a very slow technique that again requires probing

optical processes with a high scattering cross section since it does not exploit enhancement mechanisms. As such it is limited to optical processes such as fluorescence. It does however have a substantial advantage over TERS in that there is no far-field background allowing the small localised signals to be detected from the low noise environment.

3.6 TERS

The development of SNOM paved the way for apertureless SNOM (aSNOM) and TERS. These techniques utilise resonant plasmonic enhancement to couple light to the surface of a sharp metallic probe instead of through its core.

3.6.1 The TERS mechanisms

The TERS technique relies on a number of physical mechanisms that, under the right conditions, work together to establish an enhanced electromagnetic field at the tip apex. Interaction with this enhanced field results in an increased rate of Raman scattering which is recorded at the detector. It is this increase in the Raman signal that allows us to identify the signal emanating from the locally confined field at the tip apex. The principle mechanisms required to produce an enhanced field are:

Longitudinal polarisation:

The optical field at the laser focus must have a strong polarisation component aligned to the axis of the tip. This may be created by a linearly polarised beam under side illumination conditions or by focusing a radially polarised beam with a high NA objective when using a bottom illumination geometry. TERS illumination geometries are detailed in full in Section 4.2.

Surface plasmon resonance:

The tip is held in the centre of the laser focus. Here the surface electrons in the metal probe are driven, by the longitudinally polarised field, into a collective oscillation in the direction of the tip axis. This collective oscillation is called a surface plasmon resonance and couples the EM field to the tip surface. The efficiency of which the surface plasmon resonance is excited depends on the dielectric properties of the metal tip (which is size dependent), the incident wavelength and the polarisation at the laser focus.

Optical antenna:

The tip acts as an optical antenna coupling far-field radiation, via a surface plasmon resonance, to the near-field. Likewise it also converts near-field information to propagating far-field radiation allowing signal derived from the localised interactions to be measured by the detector. This is analogous to radio frequency antennae however there are increased losses since metals are not perfect conductors at optical frequencies. The efficiency of the antenna is strongly determined by the geometry and material properties due to the strict dependance on surface plasmon resonances.

Lightning rod effect:

This occurs due to the conical probe geometry and small surface area at the tip apex. The charge oscillation that occurs due to the excitation of a surface plasmon resonance creates a superposition of charge as the radius reduces down the tip resulting in an accumulation of charge at the apex. This effect produces a very large charge density at the apex which is responsible for the increase in field intensity directly beneath the tip.

3.6.2 Creating an enhanced field

For successful realisation of TERS the incident polarisation is of extreme importance. The polarisation of the incident field at the tip must be aligned longitudinally along the probe axis. The delocalised electrons in the metal tip

can be considered to be a free gas of electrons confined to the tip surface. The polarisation forces this electron gas into a collective surface plasmon oscillation in the direction of the tip axis; the electrons at the surface are driven uniformly up and down the tip. The charge densities are rotationally symmetric about the tip axis producing a phase matching of the surface plasmon oscillation around the tip circumference. This is an important requirement in order to achieve maximum field enhancement.

The conical, tapered tip geometry acts to focus the energy towards the apex by creating a superposition of the field and enforcing constructive interference down the taper due to the decreasing surface area. At the apex an effective singularity occurs since the small surface area at the final extremity of the tip is forced to hold a massive accumulation of charge producing the dramatic field enhancements that facilitate TERS. This mechanism is often referred to as the lightning rod effect since it channels a large electromagnetic field into a small, highly confined spatial region. When the electrons are driven away from the tip apex, by the oscillating field, the positive nuclei are left behind. The electromagnetic field can therefore be represented by an oscillating dipole located at the tip apex [Stranick and Novotny, 2006]. Theoretical calculations demonstrate this to be a valuable and reliable approximation with the condition that the apex radius is $<< \lambda$.

When the tip is located in close proximity to the sample a virtual oscillating dipole is induced in the surface that mirrors that of the tip. This works to reinforce the field between the tip and the sample. This is important since the TERS system cannot be fully understood by considering just the tip in isolation. The sample properties influence the overall enhancement factor, using metallic substrates that have a strong polarisability can increase the magnitude of the enhanced field between the substrate and tip. This technique is commonly employed and is known as gap mode TERS. Gap mode TERS typically requires tip-sample separations of no more than 5 nm's to realise sufficient contribution from the sample [Stadler et al., 2011b].

If the incident light is not suitably polarised, such as when the polarisation is aligned perpendicular to the tip axis, charge densities build up to oppose each other about the tip axis thus cancelling out and producing little or no net

increase in charge density at the apex. No significant field enhancement occurs in this case. Optimising the polarisation conditions are therefore critical to the TERS performance. Likewise the taper geometry is also critical in producing constructive interference to maximise charge accumulation at the apex. The dominant factor that determines the magnitude of the enhancement is the tip radius however it is also important to have a smooth, consistent taper. The taper angle has some, albeit less critical, influence on the overall enhancement. The final, crucial, consideration is the tip material. The metal must be chosen with a high conductivity to minimise damping of the plasmon resonance and it ideally must have a plasmon resonance that is resonant with the incident laser wavelength.

Analytical calculation of the enhanced electromagnetic field distribution around the tip is not possible and so to theoretical simulations require numerical analysis. Due to limited computing power and simplifications in the theoretical models there is still debate as to the exact wavelength ranges that are optimal for particular geometries of TERS tips. The theoretical simulations do however give a good guide as to which wavelengths are likely to be most productive for a particular tip material. Individual variations in tip shape found in real experimental tips influence the plasmon resonance and so physical tips may not match their theoretical resonance.

Figure 3.3 shows the output of simulations comparing the optical response of gold and silver probes for $532nm$ illumination. The simulations were conducted using a boundary element method, which solves for the equivalent surface currents induced by scattering from a homogeneous material. The model shows the clear performance increase of a silver tip over the gold tip under green illumination which is resonant for a silver tip of this geometry. This performance gain is evident both in terms of the intensity increase at the apex and also in terms of the symmetrical field distribution showing positive interference effects have taken place. Gold and Silver are the most common tip materials to be used however Aluminium has also been used for applications in the UV [Furusawa et al., 2009]. The plasmon resonance of Gold lies in the green spectral region however it is shifted into the red by the tip geometry. Silver has a lower wavelength plasmon resonance with its

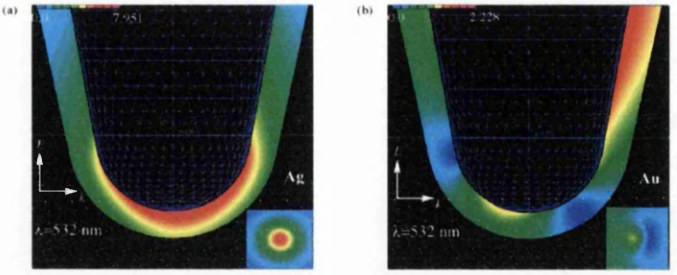

Figure 3.3: The electromagnetic field enhancement calculated for a Ag probe (a) and an Au probe (b). Calculations were conducted using the boundary elements technique that solves for the surface currents on the metal tip. The field intensity was calculated for tips with a radius of curvature of 25 nm positioned 10 nm above a glass substrate. The inserts show the electric field intensity 2 nm below the probe apex over an area of 80 x 80 nm [Lloyd, 2012]

active resonance, taking account of the tip geometry, lying in the green region. Silver enables higher overall enhancement factors than gold since it has a lower imaginary component of its permittivity under visible illumination and exhibits reduced damping of the surface plasmon resonance [Johnson and Christy, 1972]. Unlike gold however, it suffers from rapid degradation in ambient environments due to tarnishing giving it an active TERS lifetime of upto a day; the lifetime can be as short as a few hours depending on usage and experimental conditions.

The advantage of TERS over other competing optical techniques is that although it can be used to investigate high cross-section processes such as fluorescence, photo-luminescence and elastic scattering it is also able to probe low cross-section interactions such as Raman scattering. This opens the door for label free characterisation on the nanoscale. Table 3.1 demonstrates the range of applications to which TERS has been successfully applied

3.6.3 Quantifying TERS performance

There are two quantities used to quantify the TERS performance. The enhancement factor which takes into account the relative size of the far and near-field volumes and the TERS contrast. These are described by equations

Table 3.1: Examples of published work that illustrate the range of experimental configurations and applications of TERS. This set of work shows that TERS is feasible with wavelengths as low as 118 nm; in a vacuum; in liquid; on biological samples; in gap mode and non gap mode configuration; and with low laser power and short acquisition times. The illumination and collection (illum. / coll.) geometries are side, top and bottom represented by s, t and b respectively. GM stands for gap-mode with y or n representing whether the experiment was run in gap mode configuration or not.

Publication	$\lambda[nm]$	illum./coll.	Probe Type	Sample	GM	Objective	Power $[\mu W]$	Acq. $[s]$
Schmid et al. [2008]	532	b/b	Ag Coat. AFM	calcium alginate	n	60× 1.4 NA	200	-
Yeo et al. [2007]	488	b/b	40 nm Ag Coat. AFM	BCB	n	60× 1.4 NA	2-5	10
Pettinger et al. [2009]	633	s/s	40 nm Au Solid STM	SiC	n	50× 0.5 NA	2000	-
Böhme et al. [2009]	532	b/b	20-50 nm Ag Coat. AFM	Lipids on mica	n	60× 1.45 NA	-	-
Neugebauer et al. [2006]	568	b/b	Ag Coat. AFM	S. epidermis cells on glass	n	60× 1.45 NA	1500	-
Hartschuh et al. [2002]	633	b/b	30 nm Au Solid SF-AFM	SWNT on glass	n	1.4 NA	30-100	-
Hayazawa et al. [2002]	532	s/b	40 nm Ag Coat. AFM	R6G	y	20× 0.3 NA	-	-
Stadler et al. [2010]	633	t/t	75 nm Ag Solid STM	BCB and NB on mica	y	100× 0.7 NA	15	0.05
Furusawa et al. [2009]	266	b/b	10 nm Al Coat. AFM	Adenine mol. on quartz	n	0.25 NA	180	60
Steidtner and Pettinger [2007]	633	t/t	20-40 nm Au Solid STM	BCB on Au in UHV	y	Parab. Mirror	2000	1
Schmid et al. [2009]	532	b/b	40 nm Ag Coat. AFM	Thiophenol in Liquid on gold	y	60× 1.4 NA	2-100	10
Huber et al. [2008]	118	t/t	Pt Coat. AFM	Si	n	Parab. Mirror	5000	0.1
Saito et al. [2009]	514	b/b	30 nm Ag Coat. AFM	Graphene on glass	n	60× 1.4 NA	-	20

3.11 and 3.12 respectively.

The TERS enhancement factor can not be measured directly, it requires assumptions to be made based upon the illumination volume in the far- and near-field, as such it is not the most reliable measure of TERS performance. The TERS enhancement factor can be calculated as:

$$\text{Enh. factor} = \left(\frac{I_{appr.}}{I_{retr.}} - 1\right)\frac{V_{FF}}{V_{NF}} \tag{3.11}$$

Where $I_{apps.}$ and $I_{retr.}$ are the scattered raman intensity with the tip approached (in feedback) and the tip retracted respectively for the chosen vibrational mode; and V_{NF} and V_{FF} are the illumination volumes in the near and far-field respectively.

The TERS contrast is the more experimentally useful measure of TERS performance and quantifies the increase in signal at the detector due to interaction with the near-field.

$$\text{Contrast} = \frac{I_{appr.}}{I_{retr.}} - 1 \tag{3.12}$$

The magnitude of the contrast determines how reliably the increased signal can be attributed to a localised contribution from the enhanced near-field at the tip apex.

The enhancement factor is designed to be a measure of the field enhancement at the tip apex and so is not dependent on the optical volume of the sample. The TERS contrast however will be improved by working with well dispersed small structures such as carbon nanotubes where the signal contribution from the far-field illumination is reduced. Lower contrast factors are to be expected for samples such as self assembled monolayers or graphene sheets that will feature a large far-field illumination volume.

3.6.4 Scattering intensity

Raman scattering occurs when a photon inelastically scatters from a molecule loosing energy to vibrational states such that:

$$\omega_s = \omega_i - \omega_v \tag{3.13}$$

Where ω_s, ω_i and ω_w are the scattered, incident and vibrational frequencies respectively. Due to the optical antenna effect of the TERS tip both the incident and scattered fields can be enhanced. There are then two contributions to the overall scattering intensity. The first corresponds to the incident field enhancement $f(\omega_i)$, the second corresponds to the scattered field enhancement $f(\omega_s)$; where the field enhancement, $f(\omega)$, is given by:

$$f(\omega) = \frac{E_{NF}(\omega)}{E_{FF}(\omega)} \tag{3.14}$$

The scattered Raman intensity is $\propto E^2$ and so the total enhancement of the intensity of the scattered Raman light, I, is proportional to the fourth power of the field enhancement [Cançado et al., 2009]:

$$I = f(\omega_i)^2 f(\omega_s)^2 \simeq f(\omega_i)^4 \tag{3.15}$$

There are many factors that determine the overall enhancement factor. This includes the tip and substrate material; the tip size and shape; the tip-sample separation; and the temperature, incident power and the optical conditions at the tip. The collection efficiency, polarisation and tip position in the laser focus will also be critical to maximising the enhancement and achieving optimal performance. Typically enhancement factors reported in the literature range from $10^4 - 10^6$ (e.g. [Pettinger et al., 2005]).

3.6.5 Background rejection

The principal downside of TERS is that the technique is constantly fighting a large background signal. To create the necessary illumination conditions at the tip the laser beam must be focused at the tip-sample interface. In all but a few highly specialised configurations, [Neacsu et al., 2010], it is impossible to record an enhanced near-field signal without also collecting the far-field background. This requires the TERS system to be highly optimised to enable sufficient contrast for reliable TERS measurements. To further accentuate

this issue the far-field background signal can derive from the full volume illuminated by the focused laser spot whilst the near-field signal derives from only the evanescent field beneath the tip.

Background rejection techniques have been explored however they were not experimentally realised within the time scales of this project. It is possible to exploit the highly non-linear nature of the near-field signal which is readily apparent when the tip-sample separation is modulated. The background signal by contrast has a linear dependance and so de-modulation techniques can be used to isolate the two contributions. This has been successfully demonstrated by [Bek et al., 2006, Höppener et al., 2009] and can enable real time background removal with the potential to isolate weakly enhanced signals.

3.7 Summary

In this chapter we have seen how the non-propagating near-field contains information that is not accessible to traditional far-field optical microscopy. The antenna effect of the tip gives us a tool to access information contained in the near-field, the field enhancement that occurs due to the geometry at the tip apex allows this signal to be accessible in the far-field. In subsequent chapters we move on to explore the experimental equipment that is needed to realise TERS. Later in this thesis, in Chapter 8, we demonstrate how the theory can come together to produce enhanced localised signals that reveal information about a surface with spatial localisation at scales below the classical diffraction limit. The theory explored in this chapter will be used to evaluate the factors that determine the magnitude of the experimental TERS enhancements and will inform the discussion around further opportunities for experimental optimisation.

Chapter 4

TERS System

4.1 Introduction to the system

The TERS equipment used throughout this work was brand new and custom commissioned for the project. It combines two stand alone systems; a JPK NanoWizard II SPM and a Renishaw InVia Raman spectrometer. The instrument is built around a Leica DMI 3000 inverted microscope. The combined system was designed around the specific requirements of TERS and features specialist adaptations on both the SPM and optical sides of the system. It was however not sold as a fully developed, tried and tested TERS machine. This project has taken this promising start point and has worked through the initial flaws and oversights of the system to achieve a fully functioning TERS setup.

The fundamental achievements of this project have been:

- To develop sufficient topographic sensitivity when operating in shear-force feedback mode using TERS probes.
- To optimise the optical collection of the Raman system.
- To design scripted measurements and data handling software that can compile and manage the various files output from the SPM and Raman systems enabling large automated measurements.
- To refine the tip fabrication process and the TERS experimental procedure in order to minimise the time taken between tip fabrication and

recording enhanced TERS spectra.

The project builds upon previous work carried out by the group driven primarily by J.Lloyd and O.Alhartomy who have conducted TERS measurements on Veeco Aurora (2 & 3) systems.

The significant change moving to the JPK/Renishaw system from the older Veeco system is that the majority of tuneable components in the new system are motor driven and computer controlled. This is both a benefit but also at times a hinderance since the physically open Veeco system presented far more customisation potential and flexibility with regards to the optics. Motor controlled optics however allow rapid switching between paths, straightforward alignment protocols, and significantly improved ease of use across the range of measurements for which they were designed to operate. The JPK SPM offers the additional, and highly powerful feature that all properties of the SPM can be scripted. Furthermore the SPM is supported by a powerful electronic controller, based upon an FPGA, which has spare and accessible inputs and outputs. The range of potential measurements that are supported by this open approach are highly extensive making it an outstanding research instrument.

Through scripting, complex experimental procedures can be designed allowing long measurements to be conducted with little input from the user. This is advantageous both in the sense of time management and preventing human error which occurs often when long repetitive tasks are embarked upon. The main criticism of the combined TERS system is that this openness is not shared on the Renishaw optical side and the only scriptable access to Raman measurements requires exploiting the capabilities of the Renishaw network client from the JPK server script. This leads to awkward code and restricts the experimental possibilities, something that is not ideal when technique development is the primary goal. It is likely that future development of the system will require bypassing the Renishaw software to produce a complete, integrated software solution.

An overview of the system can be seen in Figure 4.1. This shows the combined configuration that consists of the JPK SPM, Renishaw Raman spec-

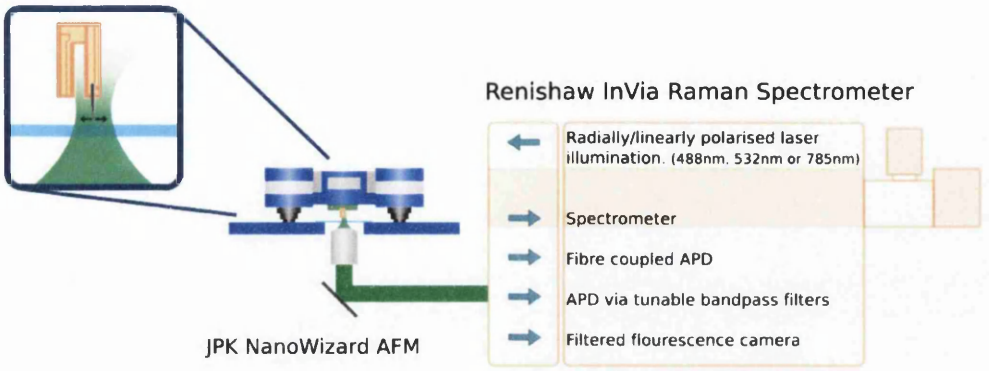

Figure 4.1: Overview of the TERS instrument. A JPK NanoWizard SPM operating in shear-force mode is combined with an adapted Renishaw InVia Raman spectrometer. Available optical paths are summarised.

trometer which is built around the Leica optical microscope. The optical and SPM aspects of the system will be discussed independently in the first parts of this chapter. The procedures involved in conducting a TERS measurement are tackled in Chapter 5.

4.2 TERS illumination geometry

There are 3 main approaches to TERS which includes bottom, side and top illumination as displayed in Figure 4.2. It is generally considered that side illumination, as shown in Figure 4.2a, using linearly polarised light offers the most optimal polarisation conditions at the tip [Hayazawa et al., 2002, Steidtner and Pettinger, 2007]. Side illumination suffers from challenging alignment of the laser focus to the tip and requires long working distance objectives that produce a large focal spot and have a reduce collection efficiency which reduces the TERS contrast Bailo and Deckert [2008]. Additionally the lack of a vertical beam at the focus inhibits complimentary far-field measurements.

The optical scheme used in our TERS configuration is a bottom illumination/collection geometry, as seen in Figure 4.2b. The use of radially polarised light combined with a high numerical aperture objective allows

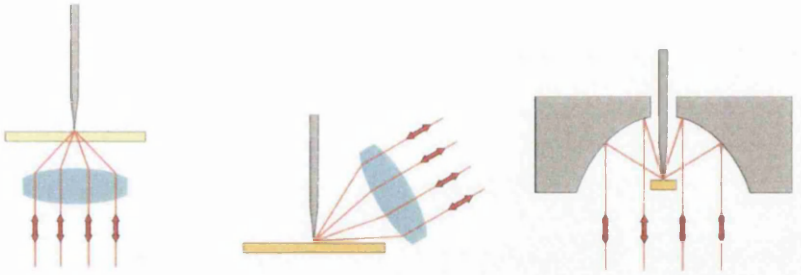

(a) Bottom illumination (b) Side illumination (c) Top illumination

Figure 4.2: The illumination geometries that can be used for TERS measurements. a) Bottom illumination which requires radial polarisation and a high NA objective. b) Side illumination which utilises linear polarisation and requires longer working distance optics. c) Top illumination which requires a parabolic mirror with radial polarisation or a conventional objective in conjunction with an angled tip and linear polarisation. Figure adapted from [Steidtner and Pettinger, 2007].

bottom illumination setups to achieve the required longitudinal polarisation, where the polarisation is aligned parallel to the tip axis, at the focus. The path of the collimated laser light travelling through the outer extent of the objective is bent inwards intersecting the optical axis at a steep angle at the focus. The transverse components of the polarisation cancel due to rotational symmetry about the optical axis leaving the dominant contribution of the polarisation orientated along the tip axis. The high angle of incidence also creates evanescent components at the coverslip surface that contribute to the localised TERS signal.

Bottom illumination has become the most prevalent illumination configuration because alignment of the tip to the optical field is the least challenging. Additionally it is less sensitive to subtle shifts in the position of the tip within the laser focus. Bottom illumination has sped up the process of TERS which is critical for work with silver tips and makes the technique more accessible for routine experiments. The most substantial disadvantage is that it restricts TERS to transparent samples and unlike side illumination the far-field background originating from the full laser spot is collected by the objective.

The final TERS configuration is top illumination as shown in 4.2c) which works on a similar basis to bottom illumination. This approach requires either a tip mounted off vertical at an angle of $\simeq 45°$ alongside a standard, longer working distance objective and linear polarisation or the use of a parabolic mirror above the tip to focus radially polarised light to the tip-sample interface. A high quality focus can be realised using this latter method and it is particularly advantageous in vacuum systems where it is not possible to get an objective sufficiently close to the sample [Stadler et al., 2008]. Parabolic mirrors are highly expensive and challenging to both manufacture and use.

4.3 Optical path configuration

The optical measurement pathways of the TERS spectrometer are presented in diagram 4.3. There are two illumination paths. The first illumination path, I1, is not part of the standard InVia Raman system. It is a custom optical path that allows greater flexibility in the beam conditioning optics that can be used. For TERS this consists primarily of ND filters and a radial polariser, it also features manually adjustable mirror mounts (M1 and M2) which provide greater stability over longer timescales than the the motor driven mirror mounts found in illumination path I2. Both the green and blue laser can be introduced into this path via removable mirrors mounted on the optical bench. The distinct disadvantage of this path is the use of the 50:50 beam splitter (BS 2) which directs the light towards the objective. The laser itself has more power than is needed experimentally and so the dumping of laser power is not an issue however its presence means that only half of the collected Raman signal reaches the spectrometer. This path thus trades efficiency for improved flexibility.

Path I2 which is Renishaw's standard Raman path demonstrates a far more elegant solution to mixing the two beam paths. The paired laser line filter features an angled reflection filter which reflects the illumination beam onto the microscope path. As a result there is no significant loss of intensity. The same is also true of the Raman signal which passes through the laser line

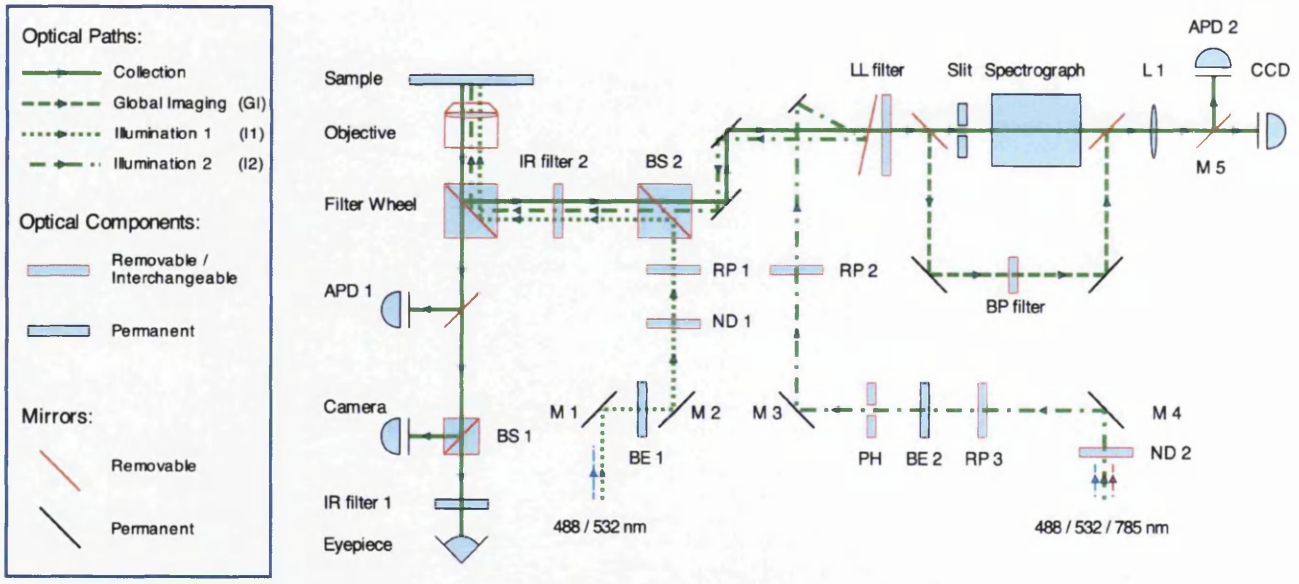

Figure 4.3: Schematic of the optical configuration used for TERS. There are two possible illumination paths, I1 (dot) and I2 (dot dash). Both feature alignment mirrors (M), a beam expander (BE), neutral density filters (ND) and a radial polariser (RP). Path I1 introduces a 50:50 beam splitter (BS) to direct the laser illumination towards the sample whilst path 2 reflects from the paired laser line filter (LL). Path I2 additionally includes a pin hole (PH) for high confocality measurements. The Raman collection path, C (solid), takes light from the objective and uses a leaky mirror positioned in the filter wheel to direct scattered light to the spectrometer. The leaky mirror allows a small percentage of transmission so that the laser spot is visible in the camera, eye-piece and APD detector. The collection path features an infra-red filter to remove the AFM laser, a paired laser line filter (LL), a slit, the spectrograph and a lens (L 1) which focuses the collected light to the CCD detector. The global imaging path, GI (dash), replaces the spectrograph with a set of tuneable bandpass filters (BP) allowing single Raman peaks to be measured with the APD or CCD detectors.

filter whilst the elastically scattered light is rejected. This path is used for all standard confocal Raman measurements that do not require the additional customisability provided by path I1. Additionally the pin hole featured in path I2 helps to produce a cleaner beam profile and to increase the confocality of Raman measurements. Full confocality is achieved by narrowing the slit size before the spectrometer and reducing the area binned of the CCD thus creating a virtual pin hole at the detector. The confocality of the system is rated as better than $2.5\mu m$ when using a 100X objective.

The $532nm$ laser features a motorised half wave plate enabling measurements that require the linear polarisation angle to be varied at the sample. An analyser can also be introduced after the laser line filter for de-polarisation measurements. The 532 and 488 nm lasers can be launched through an optical fibre for SNOM measurements or other illumination schemes. The range of measurements is further increased as a result of various fluorescence filter combinations that can be fitted in the filter wheel and a mercury lamp for use with fluorescence measurements. The system includes the option of being run with a 488, 532 or 785 nm laser. For TERS experiments the 532 nm laser has been predominantly used since this is the most suitable wavelength for silver probes. A few experiments have been conducted utilising the 785 nm laser to test the potential of alternative wavelengths, these results are presented in Chapter 7.

4.3.1 Optical adaptations for TERS

To improve TERS efficiency and limit signal rejection illumination path I2 was adapted to take the radial polariser allowing it to also be used for TERS measurements. With the radial polariser positioned at RP2 instead of RP1 the losses encountered by the beam splitter (BS2) are removed improving signal throughput and allowing reduced collection times. Short acquisition times are critical for mapped measurements where the overall measurement time must be reduced to minimise artefacts introduced by drift in the scanner and in the laser focus.

The beam conditioning was another prominent characteristic of the sys-

tem that required improvement. To achieve the correct illumination and polarisation conditions at the tip a clean focus is required. The mechanism that causes the cancellation of transverse (s-polarised) components and the superposition of longitudinal (p-polarised) components of the polarisation at the focus of a high NA objective works only for the optical components travelling through the outer extents of the objective where the folding angle is maximised. The optical components travelling on, or close-to the optical axis do not cleanly cancel and as a result produce a non optimal focus spot. This spot is hard to focus and does not feature a uniform round profile.

The quality of the focus can be improved and the beam waist reduced by removing the central portion of the laser beam prior to the focus using an annular aperture [Dorn et al., 2003, Quabis et al., 2000]. Alternatively the beam can be focused through a pinhole to reject the non-cancelling transverse components and produce the required doughnut mode prior to the objective.

An annular aperture was trialled in the system with little net improvement of focus quality. It was not permanently included since the gain was not worth the additional alignment costs. Later experiments repositioned the radial polariser to sit before the pinhole and beam expander, in position RP3, producing a cleaner beam profile. With the radial polariser positioned at RP3 there was a clear improvement in focus quality, the laser focus featured a round profile and reduced diameter.

The difference in intensity distribution as a result of the pinhole can be clearly seen by placing a piece of card in the beam path. With the pinhole positioned in the beam a radial diffraction pattern can be observed in the subsequent beam profile and the intensity at the centre is reduced demonstrating that a doughnut mode has been formed, at the focus this produces a clean profile as shown in Figure 4.4c. When the pinhole is removed, the beam is dominated by the cross produced by the segmented radial polariser and the intensity profile features further square diffraction patterns towards the outer extents of the beam which result in a messy focus as seen in Figure 4.4b.

In its current configuration this arrangement is still sub-optimal for two reasons. Firstly the pinhole is off axis and so it is not possible to centre

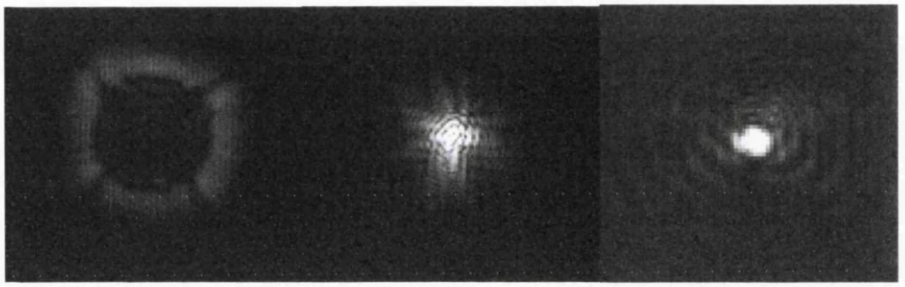

(a) Defocused **(b)** Pin hole out **(c)** Pin hole in

Figure 4.4: Images showing the laser spot as viewed in the microscope camera. a) A defocused spot as used for beam optimisation, the cross shaped shadow created by the segmented radial polariser is clearly visible, the radial polariser can be aligned by centring this cross to the beam. b) The square diffraction patterns that are present in the focused beam when the radial polariser is in the beam path and the pinhole is removed. c) The focused beam profile for an optimised beam where the radial polariser is in position RP3 and the pin hole is in place.

the beam in the expansion optics, the pinhole and have the radial polariser centred in the incoming beam simultaneously. A compromise is reached by having the radial polariser off axis which allows the cross to be centred on the beam after the expansion components. This does not ensure absolute symmetry in all quadrants of the beam which is vital to ensure the correct cancellation conditions at the focus. Secondly the beam does not pass through expansion optics prior to the radial polariser when located at RP3. As such the beam is utilising the least ideal section of the radial polariser. The radial polariser features 4 half wave plates that are orientated to create radial or azimuthal polarisation from a linearly polarised incident beam. These half wave plates are bonded which creates a dark cross in the beam due to the imperfection created by the optic at this bonded region. A non expanded beam accentuates this problem since a greater proportion of the beam is effected by the central bonded region of the optic. Therefore either beam expansion should be considered to reduce the impact of the bonded segments or the radial polariser should be replaced with a non segmented laser etched or liquid crystal radial polariser [Stalder and Schadt, 1996].

It is worth noting that polarisation degradation occurs due to reflection

from the multiple mirrors in the system. This can be counteracted by using pairs of matched mirrors mounted orthogonally or by using suitable correction optics to rectify the polarisation. These considerations are important if it is important to achieve the best possible TERS enhancements and maximise the sensitivity of the technique.

4.3.2 Objective lenses

The bottom illumination TERS geometry is critically dependant on the illumination conditions at the focus which is determined by the beam polarisation, beam conditioning and by the objective lens. Two objective lenses have been used for TERS in this work. A Leica 0.90 NA 60× objective and a 1.25 NA 100× oil immersion objective It is clear from the literature that high NA objectives are paramount to facilitate low laser intensity and short acquisition TERS measurements; the requirement is typically specified as an NA > 1 [Hartschuh et al., 2009].

TERS enhancements have been recorded with both objectives. The preferred objective lens for most samples has become the 60× since it is a better quality optic. The 100× is an oil immersion objective which requires that the sample is carefully cleaned between measurements and introduces physical drift in the system. The thin coverslips are bent by the pressure of the oil causing the focus to drift as the system relaxes.

4.4 The scanning probe microscope

4.4.1 Shear-force SPM

Tip-sample separation is maintained by operating a shear-force configuration using a quartz tuning fork [Karrai and Grober, 1995]. This differs from traditional tapping mode AFM in that the scanning probe oscillates parallel to the sample surface, the shear force geometry can be seen in Figure 4.5. Shear-force has 2 distinct advantages. Firstly it allows truly non-contact surface imaging; secondly, using a tuning fork, allows easy and reliable mounting of

custom made probes. 100kHz quartz tuning forks are used for scanning, they are cheap and reliable oscillators and typically find application in electronic timing circuits for devices such as watches or processors. Quartz is a piezo electric material which enables its oscillation to be driven by periodically applying a voltage. Electrodes are patterned onto the fork enabling a potential difference to be established across the material resulting in a controlled and repeatable mechanical displacement. The converse is also true in that the motion of the tuning fork will alter the charge distribution. This creates an electrical signal through the electrodes that can be amplified and measured to determine the oscillation properties of the fork.

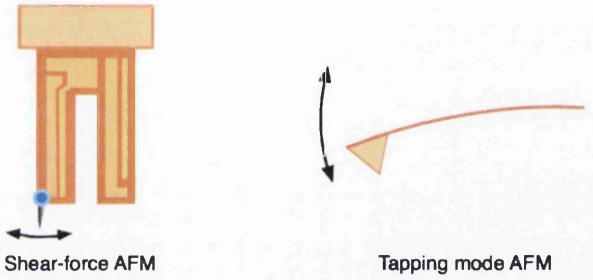

Figure 4.5: Illustration comparing the oscillation properties of a shear-force imaging system and a tapping mode AFM cantilever. Shear-force SPM uses a sharp metal probe mounted to a quartz tuning fork. The tip oscillates parallel to the surface which enables non-contact imaging. Tapping mode AFM oscillates a tip perpendicular to the surface, the tip is mounted to a soft cantilever which allows intermittent or full contact with the surface whilst preserving the tip sharpness.

Quartz tuning forks are stiff by comparison to AFM cantilevers. This stiffness confines the acoustic energy in the prongs creating a system with low losses. The Q factor is a measure of the oscillation quality, it describes the ratio between the energy stored in the oscillator and the energy lost during each cycle. In practice this is measured by conducting a frequency sweep around the forks resonant frequency whilst measuring the amplitude, equation 4.1 details how the Q factor can be calculated from the resonant frequency f_0 and the FWHM Δf.

$$Q = \frac{f_0}{\Delta f} \tag{4.1}$$

Tuning forks are designed to oscillate with one resonant mode, they employ two prongs acting as coupled oscillators to achieve this. The coupling increases the difference between the resonant frequency and that of the first harmonic. Less energy is thus lost to higher harmonics and so all modes other than the fundamental mode of oscillation are suppressed. The system as a whole acts as a second order harmonic oscillator as shown in [Karrai and Grober, 1995, Ruiter et al., 1997]. The phase and amplitude response A have been simulated by approximating the tuning fork system to a second harmonic oscillator driven with a driving force F and where the fundamental and response frequencies, ω_0 and ω respectively, are determined by the size and properties of the tuning fork system:

$$M_e\ddot{x} + F_d + kx = Fe^{i\omega t} \tag{4.2}$$

Where:

$x = Ae^{i\omega t}$,
$M_e = 0.2427\rho(LWT)$,
$k = \frac{EWT^3}{4L^3}$,
$F_d = M_e\gamma\dot{x}$,
$\omega_0 = \sqrt{\frac{k}{M_e}}$

L, W, T are the length, width and thickness of the fork prong respectively, E is the Young's modulus and ρ is the density of the tuning fork. F_d is the damping force determined by the damping constant γ. Equation 4.2 was solved in Mathematica using the above substitutions to give the result:

$$x(t) = Ce^{-\gamma t \pm it\sqrt{\omega_0^2 - \gamma^2}} + \frac{F}{M_e(i\gamma\omega + \omega_0^2)}e^{i\omega t} \tag{4.3}$$

The result has two terms, the first term shows the amplitude of oscillation to be time dependant and that it is subject to an exponential decay indicating

there is a delay before the stable state is met. The second term shows the amplitude to be independent of time and hence shows us how the system behaves in its equilibrium state. The behaviour of the amplitude and phase in response to changes in the physical properties of the system can be modelled by taking the modulus and argument of equation 4.3 respectively.

On approach to the sample the tip interacts with the long range forces at approximately $15nm$ from the sample. The forces acting on the tip cause a damping of the oscillation which results in a change in the resonant frequency of the tuning fork system. The fork is driven at its resonant frequency in free space i.e. when there are no sample interactions on the tip. Interaction with the sample causes a change in the effective spring constance and results in the fork no longer being driven on resonance causing a drop in the oscillation amplitude. To maintain a constant separation between the tip and sample a feedback circuit is employed which modulates the tip-height distance to maintain a constant feedback signal. The feedback signal must be chosen so that the system will respond rapidly to changes in the forces acting upon the tip.

Using equation 4.3 the effect of a shift in resonant frequency was calculated and plotted in Figure 4.6. The response of the phase and amplitude of the tuning fork oscillation is shown whilst the drive frequency is maintained at a constant $300Hz$. The diagram also demonstrates the effect of Q factor. The dashed line represents a higher Q factor tuning fork with a lower intrinsic damping whilst the solid line shows the response of a lower Q factor.

There are two important observations from this analysis. The feedback circuit must detect a signal that changes in response to a shift in resonance. For this purpose both the amplitude and phase signals are appropriate and both have been successfully used as feedback signals for distance control in our experiments. The amplitude however can be seen to respond slowly to a frequency shift due to the lower gradient either side of the drive frequency at $300Hz$. The phase on the other hand has a steep gradient at the drive frequency and so will undergo a large phase shift for a small shift in resonant frequency demonstrating increased sensitivity over amplitude. The Q factor will also impact sensitivity. A higher Q factor produces a sharper peak on the

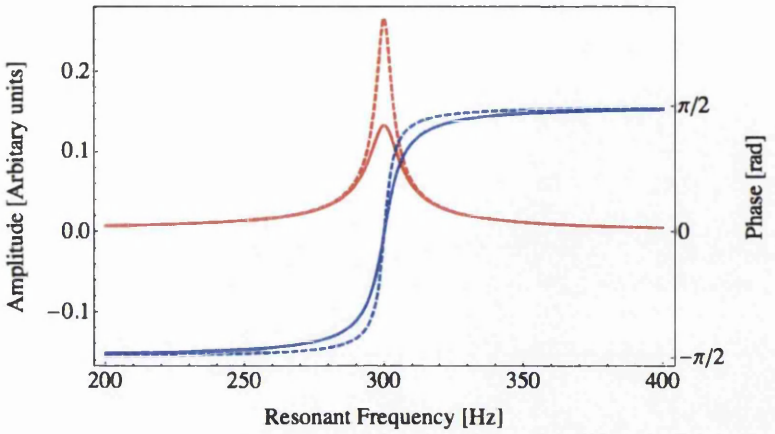

Figure 4.6: Tuning fork resonance simulations demonstrating the effect of a resonance shift on a fork driven at a constant drive frequency of $300Hz$. Blue line: Phase, Red line: Amplitude. Solid and dashed lines represent forks with low and high Q factor respectively.

amplitude curve creating steeper gradients either side of the drive frequency and hence a larger change in response for a set frequency shift. Likewise the phase curve features a steeper curve with increased Q.

The improved response of phase originates from the fact that it is a first order process where as amplitude is a second order process [Ruiter et al., 1997]. Phase changes upon interaction whilst the amplitude changes due to the shift in resonant frequency from the drive frequency. Higher Q although providing sensitivity also has drawbacks. As already mentioned there is a settling time (τ) from when the tip interacts with the sample and an equilibrium oscillation state is reached. This is proportional to the Q factor and described by:

$$\tau = \frac{Q}{\omega_0} \tag{4.4}$$

For high Q factor tuning forks ($Q \sim 1200$) this gives a time constant of $\sim 12ms$. This large settling time limits the scan line rate. Antognozzi et al. [2003] have implemented Q reduction techniques, on forks with $Q \sim 500$, in order to enable reliable imaging at faster line rates. Additionally high Q has been observed to cause intermittent contact behaviour whereby gains are

unable to maintain a constant tip-sample separation. The problems associated with settling time manifest themselves most strongly when using feedback to maintain constant amplitude however it also presents some issues when operating feedback on the phase response.

The forces acting on the tip are generally attributed to a combination of long range Van der Waals forces plus contact, adhesion and frictional forces created by a thin water film on the surface. The water film is present on all samples in ambient conditions. Unlike tapping mode AFM, which oscillates perpendicular to the surface and so exhibits intermittent hard contact, shear-force can maintain a true non-contact imaging regime with the sample. Forces acting on the tip when in feedback typically range from $50 - 500pN$ and the feedback circuit maintains a separation of around $5 - 15nm$ from the surface [Zenobi and Deckert, 2000]. Another advantage of shear-force over AFM is that the probe cannot snap onto the surface as is the case with soft AFM cantilevers. This same property also presents a disadvantage in that there is no forgiveness in the system, which is provided by flex in the AFM cantilever, and so with shear-force AFM even a soft crash will cause damage to the tip.

4.5 SPM optimisation

The JPK SPM was adapted to operate in shear-force mode through a custom tuning fork module. The operation of tuning forks on this system required significant development as the device was untested out of the box and implemented the standard AFM feedback configurations and scan parameters. Optimisation was achieved through extensive testing of multiple tips, exploring scan parameters and working closely with JPK to develop and test new feedback configurations.

The primary problem was in approaching to the surface without causing catastrophic damage to the probe. An example of the tip condition following multiple approaches under the initial feedback configuration can be seen in Figure 4.7. This problem originated due to two reasons. The feedback was operating on the pure amplitude response and not demonstrating suitable surface sensitivity. The second problem was that the JPK system was designed

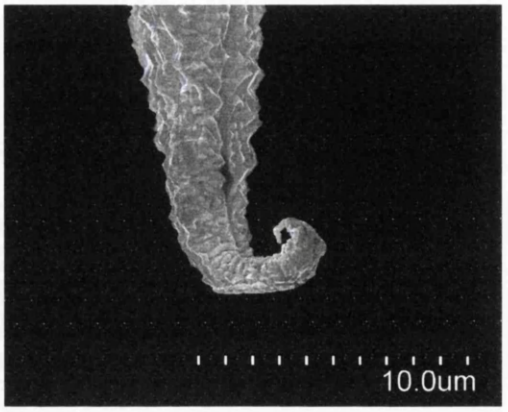

Figure 4.7: SEM image of an etched silver tip approached multiple times using the original amplitude based feedback system shipped with the system. Severe tip distortion can be seen.

to approach rapidly for AFM probes. Landing heavily on the sample does not adversely effect the hard AFM tips mounted on soft cantilevers, this is not the case with shear force configuration. Software modifications enabled a longer timeout to be set in order to reduce the approach speed. The timeout sets the time limit for a piezo sweep and is used to establish when the tip is successfully approached. It was however not possible to tune the amplitude based feedback parameters to achieve sufficient surface sensitivity.

4.5.1 *Hyperdrive* feedback mode

A new mode of feedback was applied that operates on the pure phase response of the tuning fork with the aim of improving surface sensitivity. This introduced a new problem. The phase stability of the tuning forks on the JPK system was incredibly poor. With the standard SNOM style mounting (figure 4.8a) the phase was seen to fluctuate through a range of 8 degrees as shown in Figure 4.9a. This, whilst operating with a setpoint of 1-2 degrees, unsurprisingly caused erratic and uncontrolled approaches and large height variations when in static feedback on the surface. To counter this alternative mounting procedures were tested that could produce higher Q factors. Q factors of up to 1600 could be achieved by minimising the weight glued to the tine, as illustrated in 4.8b. Figure 4.9b demonstrates that some improvement

in phase stability is seen with the higher Q factors however the 3 degree fluctuations observed are still greater than the setpoint and so this system does not facilitate reliable imaging.

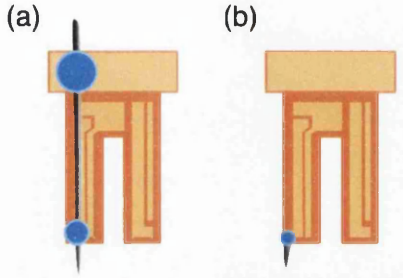

Figure 4.8: (a) SNOM style mounting, the wire is held by a large spot of glue on the can and a smaller spot on the tine. This produces Q factors of 200-600. (b) The high Q mounting method leaves only a very small length of wire secured by a small amount of glue on the tine. This system results in Q factors of 800-2400. The blue circles represent glue placement, the tip wire is shown in grey.

A method was found to improve the phase stability to acceptable levels. Q control was used to lower the Q factor. The Q factor can be tuned by either adding or removing energy with each cycle. This is achieved by adding a sine wave of the same frequency as the oscillator with a tuneable phase-shift and amplitude. In our case the sine wave is added out of phase to increase the loss in the system and reduce the Q. Figure 4.9c shows that this results in a significant improvement in phase stability with phase stability of below 0.6 degrees in 60 s. This is sufficient to image, further optimisations have been developed which includes working at the minimum oscillation amplitude of $20mV$ and tuning Q until a working Q of ~ 150 is reached. These conditions reduce the phase fluctuations to around 0.05 degrees. These developments allow us to utilise the sensitivity of phase feedback whilst having sufficient stability to not damage tips, run controlled approaches and scan accurately. This method sets a requirement on the Q factor such that the Q must exceed 800 in order to have sufficient capacity to reduce the Q factor. The magnitude of the phase fluctuation is approximately proportional to the Q controlled Q factor. The instabilities are thus dampened proportionally to the dampening

of the Q factor. Adding a periodic wave interferes to reinforce the oscillation stability despite lowering Q.

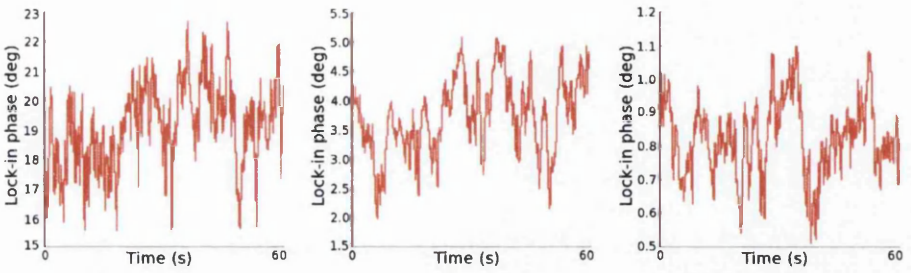

(a) $Q = 324$ (b) $Q = 1429$ (c) $Q_{reduced} = 295$

Figure 4.9: Magnitude of the phase fluctuation over 60s for different tuning fork configurations and recorded with the tip retracted from the surface. (a) The tip is mounted using the SNOM probe method. Phase fluctuates by 8 degrees. (b) The tip is mounted in the high Q configuration. Phase fluctuates by 3 degrees. (c) The same tip as in (b) with Q reduction turned on. Phase fluctuates by 0.6 degrees.

Initially it was thought that interference between the electrical drive of the tuning fork and the electrical response may be to blame for the high noise levels however this was tested by mechanically dithering the tuning fork to induce the oscillation as implemented by the older Veeco system. This proved to offer no substantial gain in the oscillation stability which suggests that the issue lies in the amplification of the small piezo induced currents or noise in the electronics.

The high Q tuning fork system operates beyond the optimised parameters of the SPM. The SPM has been designed with the relatively poor oscillation quality of AFM cantilevers in mind which typically exhibit a Q factor of $100 - 200$. Lowering the Q therefore brings the tuning fork into the optimised bandwidth of the electronics. We assume that Q control thus offers 3 benefits: Phase instabilities are damped through interference with a frequency matched sine wave. Reduced settling time allowing faster line rates. Finally the oscillation properties are closely matched to the optimised settings of the SPM.

4.5.2 *Tuning fork* feedback mode

Development was simultaneously undertaken on an alternative feedback system for operation with low Q tuning fork assemblies allowing the flexibility to operate with probes mounted in the SNOM configuration as seen in Figure 4.8a. Inspired by the feedback configurations of the Veeco Aurora system, which was able to utilise the same shear-force tips without issue, we introduced feedback that utilised the phasor mixing of amplitude and phase. This combines the stability of amplitude with the sensitivity of phase. It is possible to alter the weighting of the two mechanisms giving another layer of control to the scanning process. Imaging was achieved using this technique and unlike operating in pure phase low Q-factor tuning forks with Q of 100+ could be used.

For stability the forks were run in amplitude dominant mode employing a similar configuration to the Aurora system. The drive amplitude was tested and it was found that lower drive amplitudes produced better sensitivity and higher scan quality. This can be seen in the series of scans in Figure 4.10. The scans were conducted using the same tip at a range of oscillation amplitudes to image a DVD, best reproduction of the DVD features was observed at the minimum oscillation amplitude. Irregularities in the pit shape that are still viewable at $100mV$ drive amplitude indicate that the scan is tip limited.

A direct comparison of the two feedback systems is shown in Figure 4.11. The same tip is used in both cases. The image quality is comparable for both scans. The phase image better reproduces the pitted surface however it is brushing away dust particles indicating a harder setpoint is used. Both images show that a sharp tip oscillating at small amplitude can reproduce large scale surface features and do not suffer from significant drift or image degradation across the scan.

To demonstrate that the scan has adequate sensitivity to small structures a topography image of single DNA strands on mica is shown in Figure 4.12. Despite some noise the DNA strands are resolvable with the enlarged scan size showing the scan is tip limited. A cross section through the main strand at the centre left of the scan is shown in (b) which indicates a strand height

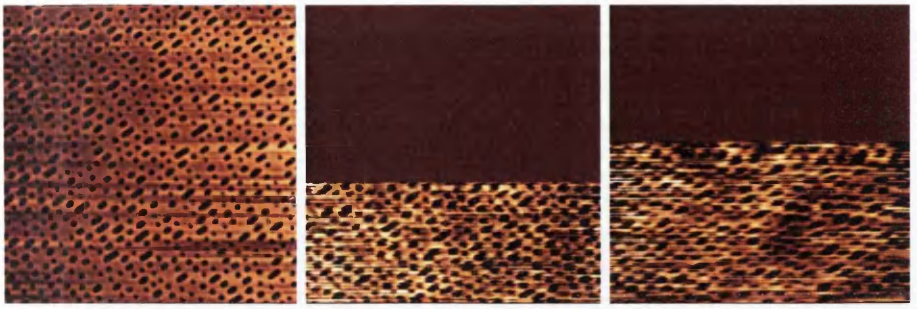

(a) AFM (tapping mode) (b) 1 V SF-AFM (c) 0.5 V SF-AFM

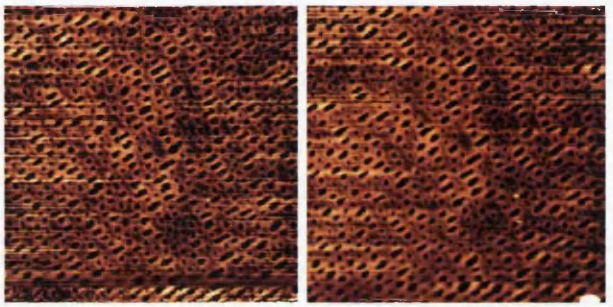

(d) 0.25 V SF-AFM (e) 100 mV SF-AFM

Figure 4.10: (a) Tapping mode AFM image of a DVD surface. Shear-force topography scans comparing the effect of the drive amplitude (b-d) whilst operating with the same tip utilising mixed phase/amplitude feedback. A scan size of $20\mu m \times 20\mu m$ was used for each topographic image.

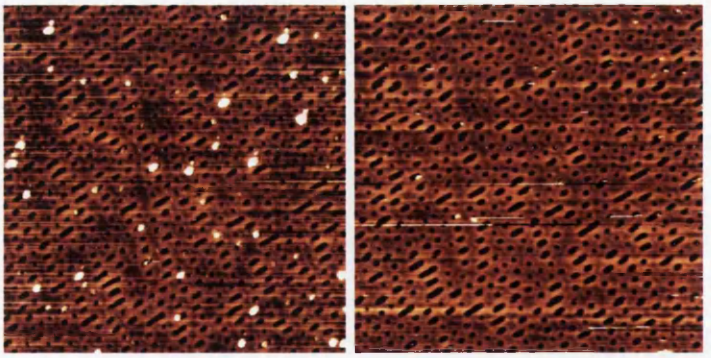

(a) Mixed phase/amplitude feedback (b) Q reduced phase feedback

Figure 4.11: Shear-force SPM image of a DVD surface comparing Q reduced phase feedback and mixed amplitude and phase feedback modes using the same tip operating at low drive amplitude. A scan size of $20\mu m \times 20\mu m$ was used for each topographic image

of $\simeq 200pm$. This shows that we are still not achieving perfect sensitivity to small features since the measured strand height is less than is expected implying that we are applying direct pressure to the DNA strand.

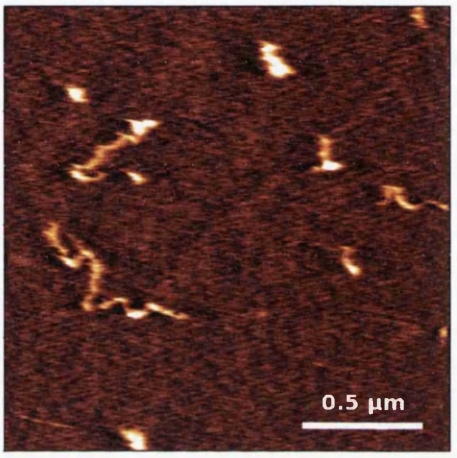

(a)

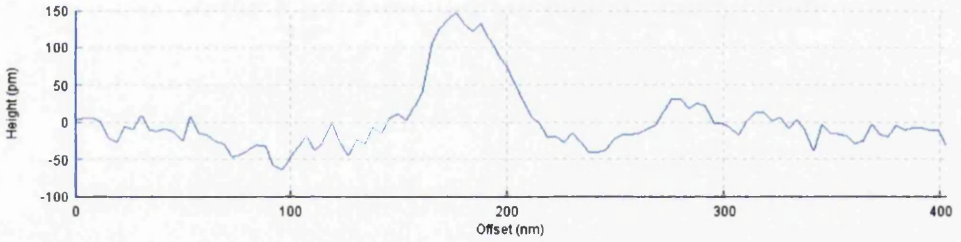

(b)

Figure 4.12: (a) Shear-force SPM topography image of DNA on mica using phase feedback. The scan size of the image is $2\mu m \times 2\mu m$. (b) cross section taken through the well defined strand on the centre left of the topography image.

4.5.3 Gold coated substrates

Gold coated substrates are often used to create a gap-mode configuration and increase the enhanced field at the tip sample interface. These are produced by depositing $\sim 5nm$ of gold using a desktop sputterer on to a glass coverslip. This process coats one side of the glass with gold. These substrates can cause unreliable imaging and tip crashing when operating in *hyperdrive* mode. The

exact cause of this scanning instability is not known but it is thought to either be caused by warping of the coverslip due to the coating process making it less physically stable or from charging effects. This has been overcome, although not consistently, by adjusting or removing the spring clips holding the sample to the stage. If this fails to solve the problem and tips continue to crash then *tuning fork* feedback mode should be used which lowers the sensitivity and is more resistant to tip crashing.

4.6 Sample stability and drift

The physical stability of the sample can affect TERS measurements. The precise nature of the alignment requires a high degree of beam stability over time. When a sample is illuminated in the laser focus heating effects can result in a slight bending of the sample causes the focus to drift. This effect is something that settles with continued illumination of the sample. The settling time is of the order of 10's of minutes.

With care the focus can be tweaked however since the microscope sits on a floating Halcyonics anti-vibration stage any contact with the microscope will effect the alignment of the TERS tip in the laser focus. If performance drops off then a refocus and realign is necessary. To reduce drift the sample is left to settle with the laser illumination on the surface until the focal drift has ceased and the sample is left continuously illuminated unless rapid photo bleaching must be considered.

4.7 TERS tips

4.7.1 Introduction to tip fabrication

The most prominent experimental challenge for reliable TERS experiments is the production of active, enhancing tips. There are a number of different approaches to tip design and fabrication which include coating commercial AFM probes, producing solid probes through electrochemical etching or ion beam milling.

Coated and solid etched probes are by far the most common probes used for TERS, both techniques are viable in their operation and ease of fabrication. All fabrication methods currently still suffer from a lack of strong reproducibility since the exact details of the tip apex are highly challenging if not impossible to control.

The choice of probe is usually dependant on the feedback systems available to the SPM. Thus coated AFM tips suit a traditional AFM setup whilst solid etched probes best suit either shear force feedback as used by SNOM systems or exploit a tunnelling current as used in STM based systems. The feedback mechanism will influence the TERS response; AFM will, in most cases, exhibit intermittent or full contact with the surface whereas shear force or STM will remain out of direct contact. The different approaches alter how the sample is exposed to the enhanced field created at the tip apex.

We have chosen to focus primarily on solid etched probes mounted in the shear-force configuration. This gives us maximum flexibility in the operation of our SPM and complete control over the tip fabrication process. Our TERS system is also capable of operating with coated AFM probes, an example measurement with a coated probe is presented in Chapter 7.

4.7.2 Coated tips

Coated AFM tips were not exhaustively trialled in this work however they were tested as a comparison to etched tips, this data is presented and discussed in Section 7.3.6. A 20 nm silver coating was applied to SiNi AFM tips by PVD and stored under vacuum until use. The tips feature a roughened surface with surface features $\sim 50nm$ in diameter. An example of an unused coated tip can be seen in Figure 4.13a. The coating process adversely effects the resonance properties of the tips and a strong resonance can not be guaranteed after the coating which degrades the tapping mode imaging ability.

Each chip features 4 cantilevers, the resonance was tested on each cantilever in turn to find one with a sufficiently high Q factor. The second complication is that heating effects, when the tip is in the path of the Raman laser, cause the resonance to shift and the tip to lift from the surface when operating

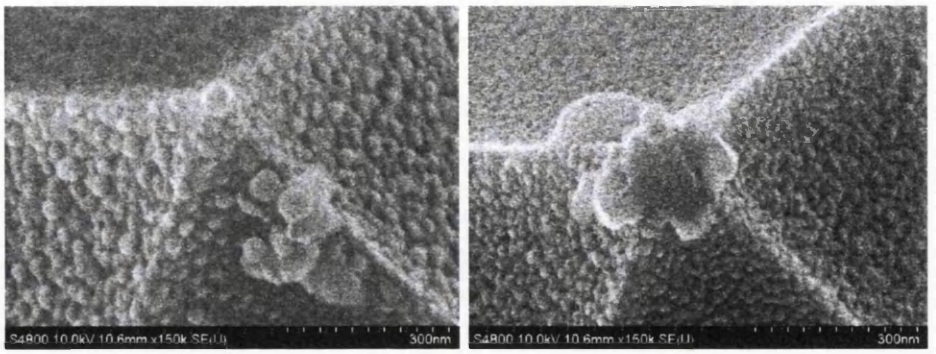

(a) Unused tip **(b)** Heavily used tip

Figure 4.13: SEM images of AFM tips coated with 20 nm of Ag

in tapping mode. To counter this low laser powers are required and a hard setpoint however this is prone to rapid tip wear which will reduce TERS performance. To allow larger laser powers contact mode feedback must be used.

Conducting TERS measurements with limited tip wear was challenging due to the degradation of the imaging stability in the presence of the laser. Figure 4.13b shows the effect of poor imaging feedback on the tip which has resulted in the flattening of the apex. It is thought that the heating at the laser focus can also lead to softening of the silver which could explain the smooth finish compared to the roughened surface deposited by the PVD.

With experience these imaging issues can be overcome as demonstrated by the number of TERS papers successfully using coated AFM tips in the literature. We were able to observe enhancement effects using the coated silver probes, results are shown in Chapter 7. It is likely that with further optimisation of the topographic imaging to improve tip wear greater enhancements can be achieved.

Coated probes suffer from poor resilience since adhesion of the coating to the Si or SiNi tip is often poor. It is possible to utilise multiple coatings to both optimise the adhesion of the final TERS active coating and to reduce the underlying refractive index of the TERS probe which can tune the plasmon resonance to the excitation wavelength [Cui et al., 2000, Yeo et al., 2009]. This

requires multiple steps in the fabrication process and the required heating can lead to further degradation of the imaging capabilities of the tip. The tip apex geometry is however far more consistent than with etched probes since it is strongly defined by the underlying geometry of the Si AFM tip.

4.7.3 Etched tips

The method of etching implemented in this work is closely based on the procedure developed by our group and published by Lloyd, J S et al. [2011]. A number of subtle modifications have since been introduced that produce an increase in reliability of the etch and improve the operational speed of the etch process. The etchant is composed of 2M nitric acid and ethanol combined in a ratio of 1:2.

A standard etching configuration is used that features a gold ring as the cathode and the tip wire as the anode. A DC current cut-off circuit is employed to apply a voltage across the two electrodes, the circuit automatically switches off the supply when the current drops below a threshold marking the end of the etch. The current cut-off prevents over etching and subsequent bluntening of the tip.

The primary adaptation to the method referenced above is that the solution is left for a period of > 3 hours prior to etching. This gives the solution time to reach a more stabilised state and is marked by the cessation of bubble formation. Preferably the solution is left to settle overnight ensuring the major reactions occurring in the etchant are complete.

The combination of the meniscus, formed by the tip wire entering the etchant, and the electric field created between the gold ring and the tip wire define the geometry of the tip and create its tapered, conical profile. The taper is formed by the evolution of the meniscus which moves down the tip wire as the etch progresses. It falls because the tip surface area decreases reducing the surface tension holding up the meniscus and the local weight of the solution increases due to the introduction of heavy products that have left the tip during the etch.

The chemical reactions that occur between nitric acid and silver are

complex and dependant on the solution concentration and applied voltage. Lloyd, J S et al. [2011] show the variation in tip surface roughness that occurs when operating in different voltage ranges. The reactions are further complicated by the presence of ethanoic acid which will form in small quantities from the oxidation of ethanol.

The magnitude of the applied voltage must be carefully adjusted to ensure suitable tip geometry since it drives the rate of the chemical reaction and can alter the reaction path. Incorrect voltages lead to round, blunt tips if too high or incomplete etches if too low. The surface texture is altered if the wrong reaction path is driven which creates rough tips that are unsuitable for TERS.

The required voltage is dependant on the composition of the etching solution, the optimum etch voltage, which is typically between 1.93 and 2.02 V, decreases as the solution settles before reaching a stable state, the solution takes more than three hours to stabilise. Once at the stable state and with the voltage correctly tuned to the solution the etch becomes more reliable and a good tip can often be achieved in one or two etches.

Throughout the development of the original tip etching method a lot of care and attention was paid to try and precisely control all parameters of the etch. This included controlling the immersion depth of the tip by using a syringe to replace a volume of etchant. Minimising vibrations by switching off the fan in the fume cupboard for the duration of the etch and ensuring volumes of ethanol and nitric were accurately measured. These interventions demonstrated improvements in the reliability of tip etching. We have since observed that once the stable etchant state is reached the etch appears far more tolerant to these factors and sharp tips can be fairly repeatably produced without having to worry about careful control of immersion depth, vibrations and etchant concentration.

We now wait until the stable state is reached, solutions are mixed the night before to ensure sufficient settling time. The tip is immersed in the solution $1 - 2mm$ by eye. The fume cupboard is left turned on throughout and the volumes of nitric to ethanol are less well controlled since the ethanol evaporates off and requires regular topping up.

The solution is topped up to maintain the working level of solution in the beaker, this is only carried out when the solution level drops substantially. The required etch voltage is not significantly effected by this variation in concentration, a short settling time of around 30 minutes is allowed after the ethanol is topped up. Adding ethanol does not trigger further bubble release indicating that fresh ethanol does not reactivate the original rapid reactions in the solution.

Etch reliability is still not perfect and subtle variations in the solution can dramatically change the etch properties. Our experience etching has lead us to the conclusion that variations in the solution have the biggest effect on the resultant tip geometry. If the solution is not stable, which can be the case even after being left to rest for several hours, then a series of tips can look completely different despite the etch parameters remaining constant. This lack of etch stability does not seem to be something that we can address through tight control of the etch parameters since the natural variation of the solution is the dominant factor effecting reproducibility. Taking advantage of statistics is often the best way of ensuring a good tip when the solution is in an unreliable state, with enough successive etches there will be a number that come out sharp. In this sense tip etching can be considered reliable as it is always possible to produce a tip that is suitably sharp when viewed in the microscope however the level of repeatability does vary with each batch of etchant. Some days sharp tips can be produced first attempt and this success can continue with every subsequent etch throughout the day whilst on other occasions it requires multiple etches.

This more relaxed etch protocol makes the etch process far more user friendly which has an implication to TERS. The TERS activity of silver tips is known to degrade over time and so speed is a vital factor when conducting a TERS experiment. It is also known that not all tips are TERS active. Under the original tightly controlled etch regime, with only a short settling time 3 or 4 tips would be etched in one go. TERS experiments would then use the tips in sequence meaning that tips were lying in ambient conditions a number of hours before use. With the new adaptations and focus on speed it is now convenient to etch tips as and when needed. This means that tips are always

used fresh from the etch and a tip can be in the system and on the surface within 20 minutes from being fabricated. This ensures we are using the tips at their most active. These same motivations have lead to optimisations in the mounting process, as discussed in Section 5, that decrease the time it takes to get the tip from fabrication to the sample surface. Faster processes not only ensure the best possible TERS activity but also facilitates greater tip throughput and so a number of tips can be trialled in one day increasing the likelihood that a TERS active tip can be found.

4.7.4 Etched silver tip geometry

Figure 4.14 demonstrates the small scale variation seen amongst sharp tips produced using the same batch of etching solution. Each of these tips would be considered suitable for TERS based upon the microscope image. The surface roughness varies considerably between the three tips. Figure 4.14a shows that a very smooth surface can be obtained where as 4.14b and 4.14c show tips that have many raised surface features. The smooth tip terminates in a feature $\sim 100nm$ in diameter whilst the rougher tips exhibit features at the apex which are $< 50nm$ in diameter.

The apex geometry of these tips as seen in the SEM shows that our etch process is not yet perfect. Tips are often dominated by the grain structure of the silver. This may be exasperated by the aggressive nature of the nitric etch. Nitric acid is known to wet etch silver and so can continue to etch even when not driven by the applied field. This may produce pitting and localised etching that occurs in addition to the electronically driven etch process. Variation in final tip shape does not eliminate the chances of TERS, enhancements are regularly observed, however this will be a factor that reduces the reproducability of the magnitude of the field enhancement from tip to tip.

Solid etched tips presented in the literature typically feature smoother and better defined apexes. TERS enhancements are not restricted to smooth tips; coated AFM probes, for example, feature a rough surface finish that is effectively made up of many nano particles attached to the surface of the AFM tip. This is often presented as an advantage of AFM tips since it is

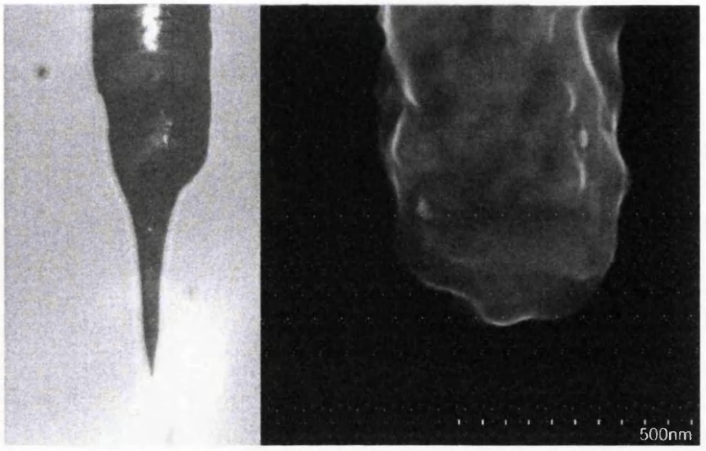

(a)

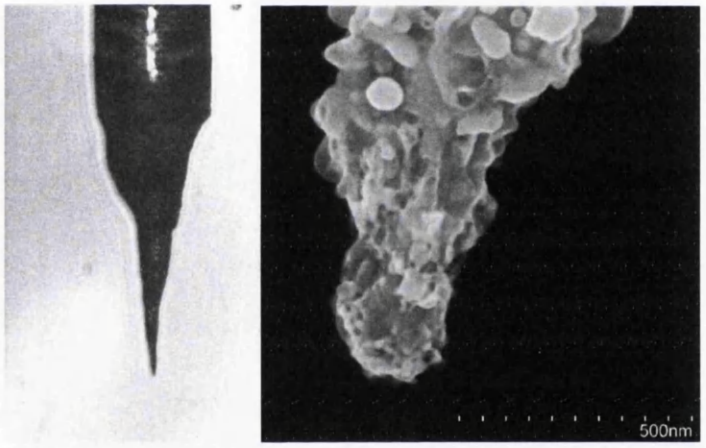

(b)

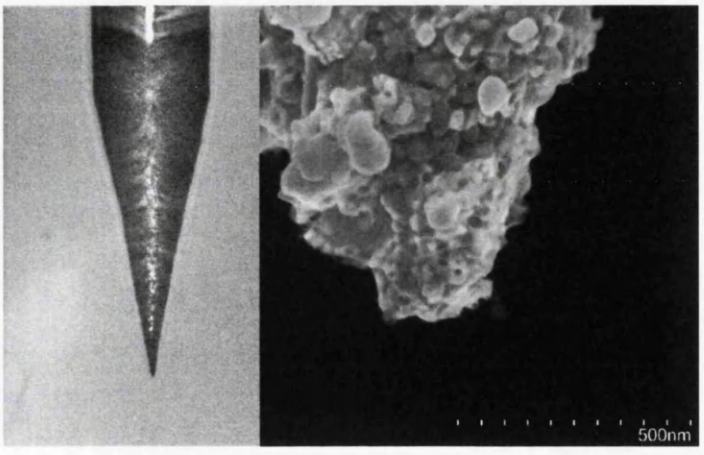

(c)

Figure 4.14: Example of 3 Ag etched tips produced from the same etchant. The left hand image in each case shows the tip as viewed in the microscope and right hand image displays SEM image of the tip apex.

likely that there will be more than one nano particle like features at the tip apex and so more than one chance at securing the required surface conditions for a TERS enhancement. We are achieving a similar outcome with the grain dominated etch. There are multiple nanoscale features at the apex and so multiple chances of achieving an enhanced spectra. This may reveal why different signals can originate from different regions of the laser spot during alignment as shown in Section 7.2.7.

The downside is that these structured tips may not fully take advantage of the lightning rod effect since the apex does not sit below a smooth conical taper. The smooth profile of the tip taper is broken by the rough inhomogenities that act as discontinuities in the surface and which create a local disturbance in the flow of surface currents. These features produce a release point for the coupled field and so can act as an enhanced hotspot. This disrupts the overall symmetry of the system. The broken symmetry may prevent a full superposition of the electromagnetic field at the apex.

The field produced by tips with these complex geometries is not well understood. A theoretical simulation was produced in collaboration with Andrew McCowan to investigate the field properties at the apex. The field profile is displayed in Figure 4.15a for a conical Ag tip illuminated with a plane wave incident from the side and polarisation aligned to the tip axis. The colour profile demonstrates the increased field intensity that is localised to the tip apex. The tip in Figure 4.15b is an etched tip that we produced and selected to help define the simplified geometry employed by the model .

The simulation analysed for the surface currents excited by the incident EM field using a boundary elements technique. It assumed a conical tip geometry. Extensions of this analysis to more complex tip geometries were not possible due to the complexity of the problem which rapidly becomes too computationally intensive. This same issue is present in other approaches to calculating the field intensity such as with the finite difference time domain technique that is commonly used. Since the problem can not be solved directly but requires finite element or boundary analysis significant approximations must be made to produce a simplified problem that can be computed in a manageable amount of time. There is little understanding of the field

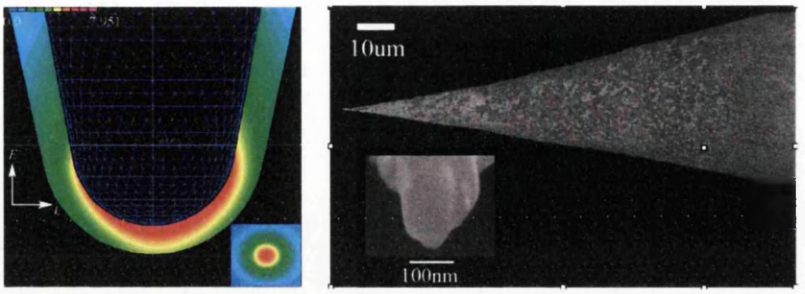

Figure 4.15: Boundary element simulation for an Ag tip with 25 nm apex radius illuminated by a linearly polarised 532 nm plane wave incident from the side. Left hand image shows the field intensity distribution in the vicinity of the tip, the inset shows the field intensity 2 nm below the tip apex. Right hand image shows an SEM image of the tip that was used to define the tip geometry used in the theoretical model [Lloyd, 2012].

properties for a tip with the non symmetric and inhomogenous geometries we are seeing in Figure 4.14a and 4.14b. A better way to consider the field profile may be to view the tip as a SERS particle adhered to a metal probe in which case the contribution from the taper can be largely discounted.

This explanation may be one reason for the relatively modest TERS contrast factors that we are observing with our tips. The other reason may be that limited tip reproducibility makes an exceptional enhancement factor a rare occurrence. This is something that is hard to compare directly with the literature as the variability in tips is not often published and published work is biased towards the most enhancing tips. To obtain smoother tips it may be worthwhile moving to a less aggressive etch such as one based upon perchloric acid [Zhang et al., 2007], this etch technique is proven in the literature to produce smooth silver tips. The SEM images show that the etch is dominated by grain boundaries. This presents a further path to optimisation, thermal annealing could be used to alter the grain properties of the silver and so may offer a method to create smoother and/or sharper tips.

In summary by increasing the number of hotspots through complex geometries we increase the odds of achieving an enhancement. The overall magnitude of the enhancement however may be negatively effected by reduced lightning rod effect since the broken symmetry does not promote field

enhancement contributions from the taper. More than one active hotspot will also cause complications in the data analysis, multiple signal sources lead to a decrease in the TERS resolution and a convolution of Raman signals.

4.8 Summary

Development of both the optical and SPM sides of the system has been a critical output of this work. Without the improvements described in this chapter reliable TERS measurements would not be possible. The scanning sensitivity in particular is of fundamental importance since the tip must not contact the surface and must be held within 15 nm of the sample surface in order to expose the sample to the enhanced field generated by the tip. The exponential decay of this field makes the magnitude of the enhanced Raman signal highly dependant on the tip sample separation and so separation stability is important to ensure consistent and reliable TERS measurements.

Tip technology is still the limiting factor when it comes to the wider adoption of TERS. $\sim$ 50% of tips produced using this etching method and selected for experiment exhibit TERS activity however exceptional enhancement factors are rare and this is likely to derive from the small-scale variability at the tip apex. Improvements in the tip fabrication process, which is further explored in Chapter 5, have simplified the etch and helped to reduce the setup time of a TERS experiment (from etch to approach) to around 20 minutes. Furthermore improvements allow tips to be etched on demand minimising the time the tip is left in ambient conditions where its performance will degrade.

Chapter 5

TERS Procedures

5.1 Introduction

This chapter outlines the methods employed when conducting TERS measurements. The routines are detailed in full however further explanations of the motivations and reasoning behind the procedures are not included in this discussion and can be found in other sections of this thesis.

The chapter is split into two sections; the first outlines the standard procedure required to setup the system, fabricate a tip and then align the tip to the laser beam ready for TERS measurements. The second section details the possible procedures that can be employed to conduct a range of TERS measurements once an active tip has been approached to the surface of a sample.

The methods described are the final procedures which have become settled upon over the development of the system. A particular focus of this work has been to optimise the experimental procedure for speed and remove unnecessary steps that introduce delays to the process. It also assumes that the illumination path I2 is used and that the radial polariser is in position RP3 (see Figure 4.3). This configuration has surfaced as the best possible way of running TERS measurements using the current experimental setup. There are still a few notable limitations of the system, recommendations for improvements are detailed in Chapter 9. Due to the evolution of the system

the configuration and methods used during measurements presented in later chapters may differ in some cases from the ones discussed here. Optical components and paths are referred to using the labels defined in Figure 4.3.

5.2 Beam conditioning and optical alignment

The quality of the laser focus is a fundamental requirement of the TERS procedure. Before commencing the TERS experiment beam conditioning is conducted to produce a small round focus that exhibits an even and symmetric intensity distribution.

To begin the alignment the sample must be in place and the SPM head located in position on the microscope so that the weight is correctly distributed on the anti-vibration stage. The half wave plate, that sets the polarisation axis of light leaving the 532 nm laser, is rotated using the Renishaw *System Configuration* software to its, pre-set, indexed position. This aligns the polarisation axis to the radial polariser to create radially polarised light. The beam profile is examined by moving the objective through the focus. The beam steer motors are used to improve the beam quality and profile; these are controlled within the Renishaw *WIRE* software. The right hand mirror (M4) is used to ensure the beam is symmetric in intensity through the pinhole. The symmetry can be viewed in the camera by defocusing the spot with the pin hole in place, as shown in Figure 4.4a, or by interrogating the beam after the expansion optics using a white card. The right hand mirror must be adjusted iteratively with the radial polariser position since adjustments are dependant on steering the beam through the pinhole which alters the location of incidence on the radial polariser. The radial polariser must be positioned such that the visible cross is centred in the beam when viewed after the expansion optics. This can often be easier to see by removing the pinhole, if the radial polariser is too far off axis distortion will be visible in the focused last spot.

The left hand mirror (M3) is used to adjust the angle at which the beam is incident on the sample. The beam should be vertical which can be achieved by steering the beam and checking for radially symmetric expansion and

contraction of the laser scatter when moving through the focus. A cross-hair on the camera is used to mark the laser position; this is both to aid measurements, since the sample and laser cannot be viewed simultaneously, and to maintain system alignment. If the final position of the laser spot is displaced from this cross hair then the cross hair should be moved to depict the new beam position and a realignment of the slits and shutters is recommended. This is an automated process within *WIRE* but requires the introduction of a silicon sample.

The final beam shape after these two processes should be round and feature an even intensity profile with only light diffuse scatter visible around the spot, a good focus is demonstrated in Figure 4.4c. The diffuse scatter should be largely symmetric. Users should also be aware that a reasonably small deviation of the spot position using the left hand mirror can cause the beam to be clipped by the sample stage and adversely influence the symmetry of the spot.

The sample should be moved to the region of interest using the camera cross-hair to align the sample to the laser position. Once the sample position is set the adjustment thumbscrews must be reversed half a turn to decouple the sample holder from the sample stage. If the sample features complex structures and is not homogenous then characterisation will have be conducted prior to TERS measurements using tapping or contact mode AFM to identify structures of specific experimental interest.

5.3 Tip production and mounting

5.3.1 Tip etching

A solution of 2M nitric acid is mixed with ethanol at a ratio of 1:2. This is left to settle in the etching beaker for a period of more than 3 hours. The gold ring is checked for signs of silver deposition, if there is a strong difference in colour between the ring and its natural colour then the gold ring requires polishing using metal polish and then thoroughly rinsing with solvents.

The tip etch apparatus is set up as in diagram 5.1. The tip wire is threaded

through the hole in the wire holder with ~15mm emerging from the bottom. The top of the tip wire is secured using locking nuts onto a screw which is threaded through the tip holder. This ensures a good electrical connection; a crocodile clip is clipped to this screw connecting it to the positive terminal of the cut-off circuit.

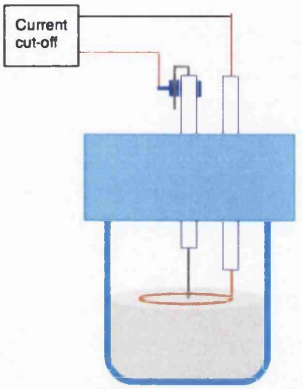

Figure 5.1: Schematic of the tip etching apparatus. Tip wire (grey) is held in the holder (purple) and clamped by lock nuts onto a screw that is threaded through the tip holder (dark blue). The gold ring (orange) is positioned symmetrically around tip wire and is half submerged in the tip etching solution. The gold ring and silver wire are connected to the negative and positive terminal of the current cut-off circuit respectively.

The tip holder is inserted through the hole in the lid and secured using a locking screw. The height of the gold ring is adjusted so that it is half submerged in the solution and positioned symmetrically around the tip wire. The height of the tip holder is then tweaked to leave the tip wire submersed to a depth of 1-2 mm. This is achieved by lowering the tip holder until a meniscus is seen to form in the solution and then lowering it 1-2mm further. This action becomes repeatable with practice, the exact immersion depth will be dependant upon the user; this is compensated for by the etch voltage. The etch voltage is set to between 1.93 and 2.02 V and must be optimised within this range for each batch of etchant.

Etching is repeated until a promising tip is identified in the optical microscope which is determined by the apparent smoothness and shape of

the tip taper, an example can be seen in Figure 5.2. A sharp tip will be diffraction limited at the apex, further examples of tips are shown in Chapter 7. If multiple etches do not produce a sharp tip then the etch voltage is adjusted. Tips are dipped in ethanol, when removed from the apparatus for inspection, and air dried.

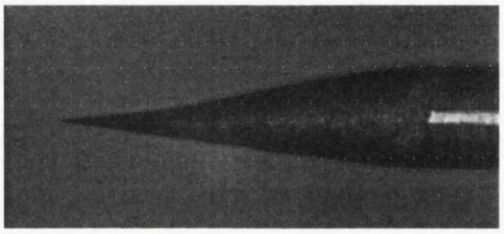

Figure 5.2: An etched tip suitable for TERS measurements. This image shows a tip as viewed in the optical microscope immediately after the etch. The profile, texture and visibility of the apex inform the decision whether to use the tip or continue etching.

Tip mounting

The tip is transferred to the mounting stage where the tip wire is held by magnets to the arm of an x-y-z translation stage. The etched end of the tip wire is left to protrude by 40-50 mm as illustrated in Figure 5.3a. A pair of tweezers, that have been fixed to a stand by the bottom blade rendering this blade immobile, are positioned beneath the tip wire. The tip is manoeuvred until the tip wire sits on the bottom blade of the tweezers with only the etched taper overhanging. This is conducted whilst viewing the etched end of the tip in a long working distance microscope. Fine adjustments of the wire position are achieved using the micrometer screws on the x-y-z translation stage.

The tip wire is positioned such that only the tapered section of the tip wire is left protruding beyond the blade of the tweezers as shown in 5.3a. The top blade of the tweezers is carefully lowered by hand whilst viewing from above in the microscope. The tip wire is left pinched just above the taper. Force is applied to ensure the wire becomes flattened in the tweezers and care is taken not to release the tip.

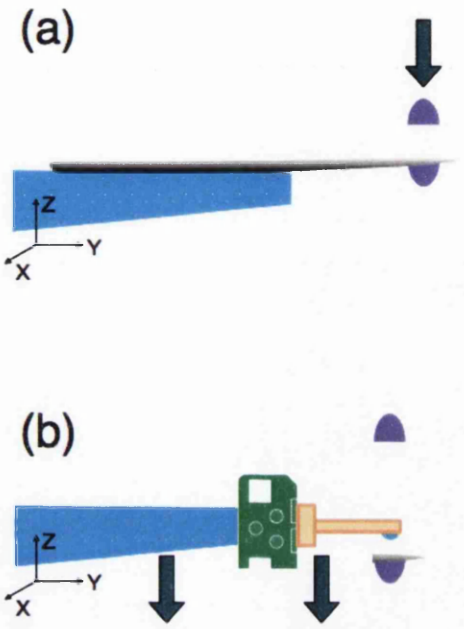

Figure 5.3: Side view of tip mounting rig. (a) The tip wire (grey) is mounted to the x-y-z translation arm (blue) which facilitates fine positional control of the tip. The tip is positioned on the bottom blade of the fixed tweezers (purple). Pressure is applied to the top arm to clamp the tip above the taper. Excess wire is removed, the remaining tip wire stays fixed to the bottom arm of the tweezers when pressure is released. (b) The tuning fork assembly (green/orange) is mounted to the x-y-z translation arm (blue) and positioned so that the outside tine, that has been pre-glued with a small drop of UV cure glue (blue), lines up with the tip shaft. The tuning fork assembly is lowered on to the tip, the glue grabs the tip and ensures transfer from the tweezers to the tuning fork.

A pair of cutting tweezers are used to cut off the excess length of wire that protrudes from the back of the tweezers. This is best conducted by raising the cutting tweezers from below and using the back of the fixed tweezers as a guide to cut along. The fixed tweezers can now be opened and the etched tip will be stuck securely to one of the tweezer blades. With practice a very short length of wire can be left with no damage to the etched tip taper.

A tuning fork assembly is positioned using blue-tack on the x-y-z stage

and a small spot of UV cure glue is applied to the front tine of the fork using a cleaved optical fibre. The glue must be on the appropriate face of the fork which depends upon which blade of the tweezers to which the tip has stuck. Using the x-y-z stage in combination with the microscope the tuning fork is positioned so that the glue can be brought into contact with the tip shaft as illustrated in Figure 5.3b. Importantly the tapered section is left protruding and does not at any point come into contact with the glue.

The glue facilitates the transfer of the tip to the tuning fork. Subtle adjustment of the tip position on the fork is often required once transferred, this is achieved by carefully pushing the tip wire with the end of a cleaved optical fibre. An image of the tip mounted to the tuning fork is shown in Figure 5.4a. It is important to consider how the tip will be presented to the microscope and the laser focus, Figure 5.4b shows how the tip is viewed in the TERS microscope. For ease of operation the tip wire must be positioned towards the front of the tuning fork so that it is not blocked by the shadow of the tuning fork when mounted in the SPM and viewed on the TERS microscope. The tip is usually left slightly angled ($\sim 7°$ off vertical) so that the front edge of the tip taper is near parallel to the optical axis. To secure the tip the glue is hardened through UV exposure for ~ 3 minutes.

SPM approach using *Hyperdrive*

The mounted tip is transferred to the SPM, the head is positioned to leave the tip close to the optical axis, the sample has been previously aligned to the laser spot and left on a region of interest. The fork resonance is then set in the JPK software. The standard shear-force configuration utilises *hyperdrive* feedback mode, which operates on phase. The key parameters for this operational mode are gain = 1, drive amplitude = 0.02 V and the Q control amplification is tuned to produce a resonance peak of 100mV in amplitude, the resonance will be centred around 100kHz. The drive frequency is then set to the maximum of the resonance peak. The head is lowered by eye until the tip is close to reaching the sample. The AFM is set to do a step approach which lowers both the piezo's and the motors alternately to

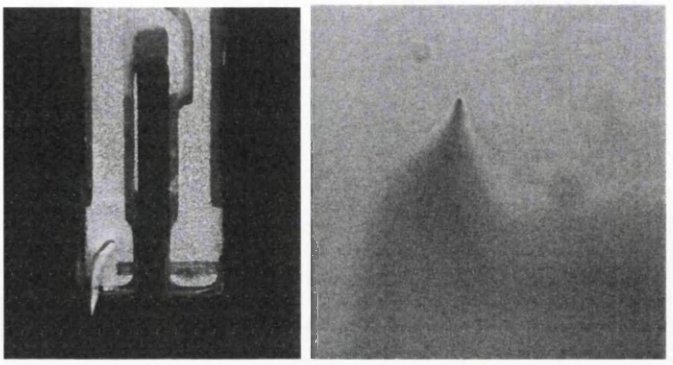

(a) Mounted tip **(b)** Tip as viewed during TERS

Figure 5.4: a) Microscope image of a solid etched silver tip mounted to a quartz tuning fork. b) Camera image of the tip in the TERS system with the objective focused on the tip apex. The slight angle that is introduced when mounting allows the tip to protrude beyond the shadow created by the tuning fork which can be seen in the bottom right of the image.

successfully approach the sample. The gains are adjusted such that one full $15\mu m$ sweep of the piezo's takes around 20 s.

Once the surface is found the piezo's are retracted and any required positional change of the tip, relative to the optical axis, is conducted using the coarse positioning screws on the head; this should only require a small tweak to compensate for the different mounting position on each fork. The scan outline mode is used to trace the scan region which ensures that the subsequent scan will encompass the laser spot. The z range is lowered to $3\mu m$ however this may be dependant upon the specific needs of the sample. The approach gains are raised and the timeout is reduced to compensate for the lower travelling distance of the z piezo. Reduced z range allows better sensitivity since it matches the expected height variation to the dynamic range of the electronics.

Alignment of the tip to the laser spot.

To locate the laser spot with no risk of tip damage the tip is first scanned off the surface through the laser spot. The SPM is operated in false feedback mode, whereby the setpoint is set to a value that lifts the tip from the

surface, this enables large and rapid scans through the laser spot. The optical configuration must be set such that the filter wheel is positioned for Raman measurements; the mirror (M5) is in place sending light to APD 2; the *Global Imaging* path is selected with no band pass filter in place (an indexed position is selected in system configuration); and the focus is set on the tip apex. A laser power of between 5 and $50\mu W$ ($0.05\% - 0.5\%$ laser power) is used, this will vary depending on the quality of the tip. A low laser power is used for initial measurements to prevent damage to the APD from strong backscatter. The reflection intensity is then collected on APD 2 whilst the tip is scanned off the surface through the laser spot. This allows the laser spot to be located. The focus is then returned to the sample surface and the scan is repeated with the tip in feedback. Typically the starting parameters for topographic scans on the surface are: line rate of 0.5 Hz, setpoint of 0.7, I gain of 1000-1500 and scan size $< 10\mu m$. Scan resolution for an APD image must be 128x128 pixels, the APD and topographic image are collected simultaneously. The APD image, an example of which is shown in Figure 7.9, is used to identify where to position the tip for TERS measurements which is discussed in detail in the following section.

5.4 TERS procedures

The procedures discussed in this section combine the standard functionality of the combined system with additional capability created by custom written Jython scripts on the JPK instrument. Jython is a variant of Python that compiles to run on the Java virtual machine, it has the ability to import existing Java classes allowing the full functionality of the JPK AFM to be easily scriptable. The system was delivered with a TCP/IP script that allows communication between the JPK and Renishaw systems. The JPK system establishes the connection and acts as the server whilst the Renishaw system is the client responding to tasks sent from the AFM. The server side script is customisable however we do not have the same level of access to the client script. As such custom implementations to the JPK server script were developed to allow specific measurement routines to be conducted. Batch

processing software was written in Python to compile the data collected by the two systems which both ensures the integrity of the data and compiles a database of all measurement parameters and data files in one place, this is discussed in detail in Chapter 6.

5.4.1 APD alignment

The most critical part of the TERS procedure is to ensure optimal positioning of the TERS tip in the laser focus. The primary method of alignment follows a similar technique to that used by Rasmussen and Deckert [2006]. The TERS probe is scanned through the focus whilst the reflection intensity is measured on APD 2 via the unfiltered *global imaging* path, as discussed in Section 5.3.1. An image is produced that maps the intensity of the scatter as the tip moves across each pixel in the scan as seen in Figure 7.9a. Typically a coarse map is first done off the surface in false-feedback. Once the location of the laser spot is well defined the tip is approached and the optical map is recorded with the tip on the surface. It is important to minimise the number of surface scans to reduce the chances of tip contamination and wear.

The APD intensity measurements allow the raster scanning tip to produce an image at the scan resolution. The APD imaging works best when a lower scan resolution is used as it creates a larger effective integration time per pixel. The intensity profile is a convolution of the beam profile and the tip shape. On a well defined tip this will produce a round spot with a noticeable bright spot at its centre as seen in Figure 7.9. Figure 5.6 shows a less well defined spot that results from the tip meeting the surface at an angle, this does not rule out enhancements and the backscatter, combined with previous experience, still allows the location of a TERS hotspot to be predicted. The tip location is selected first at the position of maximum intensity of the backscatter. Once a tip location is set the AFM is switched to stage scanning mode so that the tip position remains constant relative to the laser spot.

Often the tip position is further optimised through point spectra. With many tips there are multiple hotspots or a broad region of high intensity at the tip apex. This can originate as a result of a blunt or double tip and

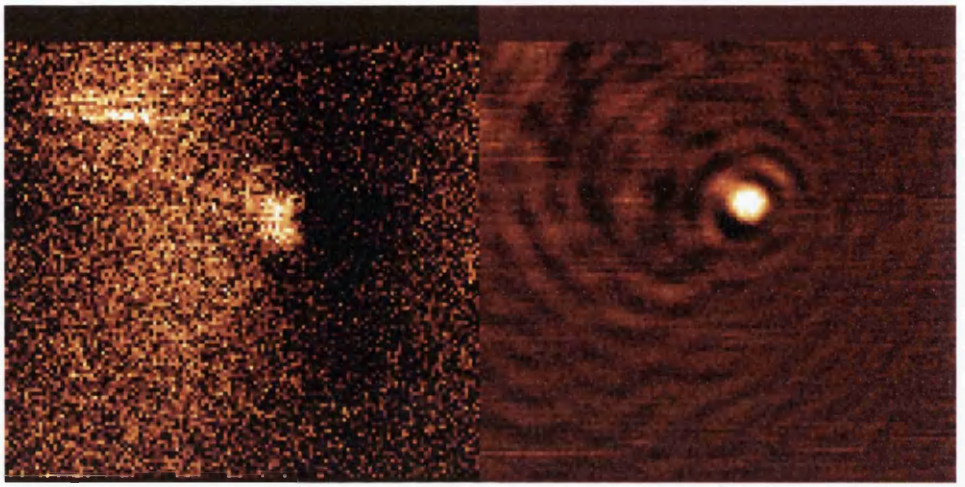

(a) APD 2 (b) APD 1

Figure 5.5: The backscattered intensity from a sharp vertical tip as it is scanned through the laser focus. This image is used to align the tip in the laser spot. The two images a) and b) compare the intensity distribution as measured on APD 2 and APD 1 respectively. These measurements were conducted with a laser power of $\sim 5\mu W$, the scan size is $10\mu m \times 10\mu m$.

sometimes irregularities higher up the tip shaft produce strong backscatter. In these cases multiple tip positions are trialled, TERS spectra are taken at each location to find the strongest TERS response. Once happy, the tip location is fixed and SPM operation is switched to the sample scanner allowing mapped measurements of the sample.

The system presents one significant operational challenge from this point. The microscope sits atop a Halcyonics anti-vibration stage leaving the microscope floating relative to the spectrometer. As such any interaction with the microscope will cause the beam position at the sample to shift and the TERS optical alignment integrity to be lost. In most cases the alignment process must be repeated following any alterations to the focus or after viewing the sample under white-light illumination. With care focus can be adjusted however it cannot be assumed that the spot alignment is maintained and a reference spectrum should be taken.

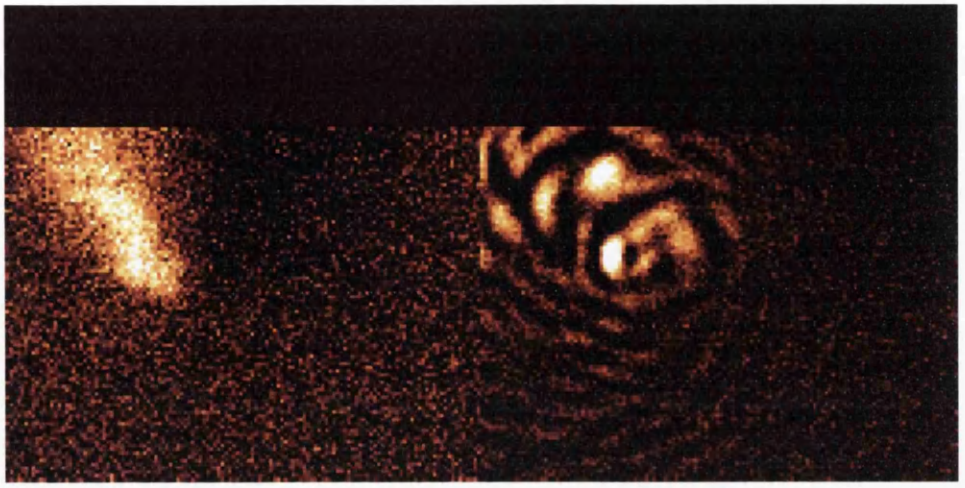

(a) APD 2 (b) APD 1

Figure 5.6: The backscattered intensity from an angled tip as it is scanned through the laser focus. The two images a) and b) compare the intensity distribution as measured on APD 2 and APD 1 respectively. These measurements were conducted with a laser power of $\sim 5\mu W$, the scan size is $10\mu m \times 10\mu m$.

Dual APD alignment

In theory APD 1 and APD 2 are measuring different forms of scatter. APD 1 is unfiltered and so should report on both the elastically and in-elastically scattered light of which the elastically scattered light will dominate. The path to APD 2 features a laser line filter which should remove elastically scattered light leaving the image dominated by the in-elastic scattering. In practice there is enough laser breakthrough on this path that the elastically scattered light still forms a significant contribution to the resulting image.

The images produced by the two APD's can be seen in Figure 5.6, they differ significantly for reasons that we cannot fully explain. The images are formed by measuring the intensity of the scatter at each tip location, the intensity is recorded from a relatively large detection surface and so should not be readily influenced by differences in the mirrors and lenses between the two paths. APD 2 typically produces a cleaner image of the tip profile whilst APD 1 shows more interference effects. From APD 2 the position of

the hotspot can be guessed by judging where the tip apex should be based upon the projection of the taper profile, an intense region may also be seen indicating a hotspot. APD 1 often demonstrates greater sensitivity to the TERS hotspot through a well defined bright region on the image as can be seen in Figure 5.6b. If there is not enough TERS activity to produce this visibly hot location the image is of little help as the overall tip profile is hard to determine.

Having both APD's can be of use to rapidly establish the hotspot location. There is however one severe limitation of operating with APD 1, the mirror below the filter wheel must be in the beam line which prevents the spot from being viewed in the camera. This means that it is not possible to observe whether the laser focus has drifted when running TERS measurements reducing the reliability of the subsequent data. APD 1 is thus most useful on a preliminary scan of the laser spot to identify a potential hotspot location, particularly if APD 2 proves to be ambiguous. A repeat scan must then be conducted with the mirror removed so that TERS measurements can be conducted whilst monitoring the laser focus.

Full spectra TERS alignment

An alternative method of alignment, which works best on highly homogenous samples, is to take a grid of point spectra across the location of the laser spot as seen in Figure 5.7. A spiral grid is defined that is aligned to the backscattered laser spot. The TERS instrument takes point measurements from the centre of the grid outwards thus probing the most promising locations first. A full TERS spectrum is taken at each point on the grid allowing the Raman response to be the indicator of TERS activity. Since short acquisitions are required for this to be a sensible alignment process Raman signal is only observed when the tip location in the laser spot produces a near-field enhancement. Locations of enhanced activity are marked in green in Figure 5.7.

This process is slower than utilising purely the APD signal. It is useful if laser spot characterisation is of interest or as a secondary technique if aligning based upon the APD image of the backscattered laser spot was not

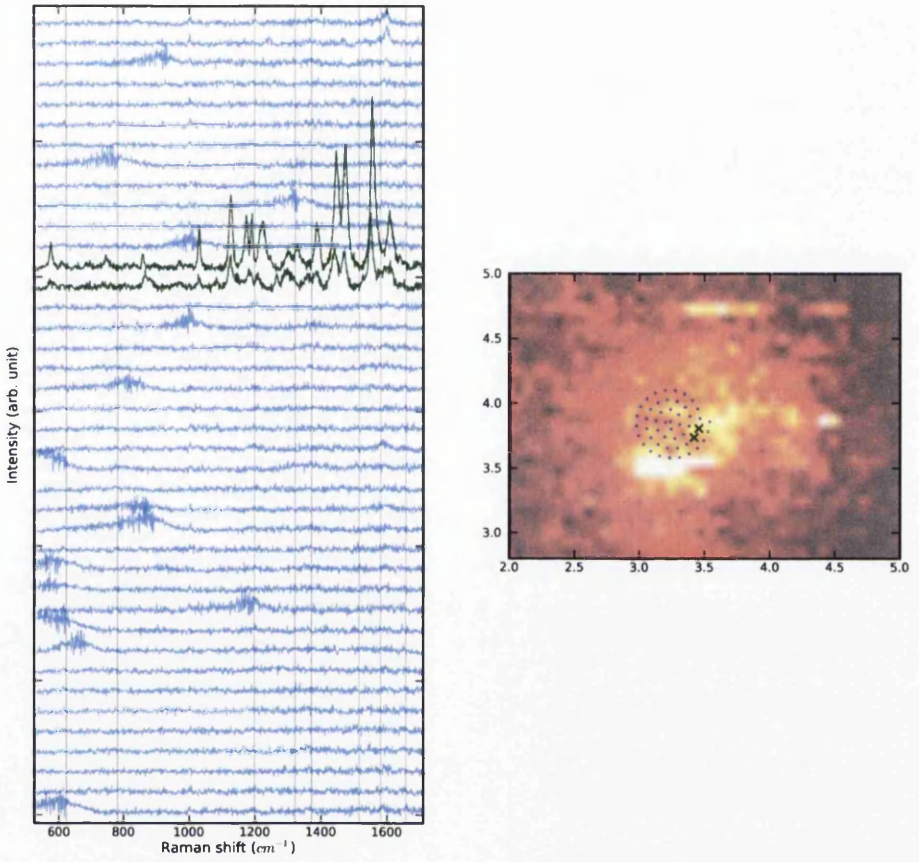

(a) Raman response **(b)** Alignment grid

Figure 5.7: Example of using a grid of TERS spectra for tip alignment. A grid of points, in spiral configuration, is defined using the convoluted APD image of the laser spot. A Raman spectrum is taken at each position with the tip in feedback with the sample. The Raman response (a) starts from the centre of the spiral (bottom spectrum) working outwards. No Raman activity is visible up until the spectra drawn in green where numerous Raman peaks appear. These locations are marked by green crosses in (b) and can be seen to lie near the centre of the backscattered spot. Spectra were recorded over a 15s acquisition with a laser power of $10\mu W$

sufficient to identify an enhancing feature on the tip. This technique requires far more time in feedback with the sample and so care must be taken to avoid contamination or damage to the apex.

Pseudo laser scanning

The full spectrum TERS alignment process can also be achieved on inhomogenous samples by an extended script that creates a pseudo laser-spot scanning regime. Laser scanning, which takes a series of TERS measurements whilst the beam is steered to different locations around the tip apex, has proven to be an effective and rapid method to achieve optimal TERS alignment and is used very successfully by Stadler et al. [2010]. Laser scanning allows the optical conditions at the tip to be tuned whilst ensuring the physical structure beneath the TERS tip remains unchanged.

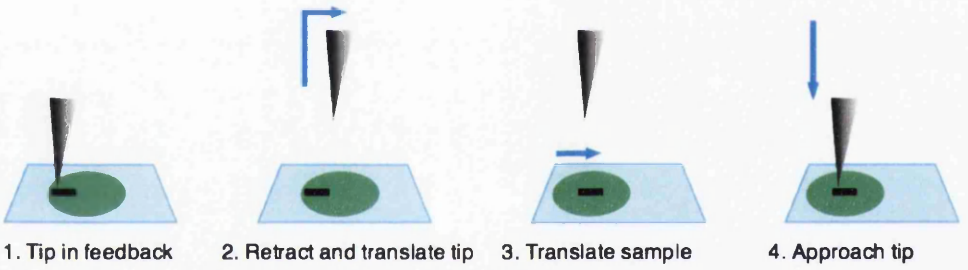

Figure 5.8: Schematic showing the process of pseudo laser scanning which is achieved by moving the tip and sample synchronously. A TERS measurement is taken (1) the tip is retracted and translated (2), the same translation is applied to the sample (3), the tip is approached ready for the next TERS measurement (4). This process leaves the tip located on the same sample feature but with the tip and sample positioned in a different region of the laser spot.

We can achieve the same outcome by synchronously moving the tip and the sample so that the tip position relative to a sample feature remains unchanged whilst the position of the tip in the laser spot is altered. This process is illustrated in Figure 5.8. A grid of TERS measurements can then be used to find the most active location for the tip. This is particularly effective on structures such as nano wires which are small and spatially well

defined. The method first requires a topography scan of the surface in order to identify and align the tip to a suitable surface feature.

5.5 TERS mapping

TERS maps are produced by taking a grid of TERS point spectra across a feature of interest. Maps are conducted using a modified version of the TCP/IP script that was supplied with the system. In its original form this script could coordinate a series of point measurements between Renishaw and JPK systems. The modified version has eliminated bugs leading to reliable operation, this is an absolute necessity considering the time invested in manufacturing and aligning the tip and has introduced a number of additional features that improve the functionality for TERS measurements.

The principle addition is the ability to record a spectrum with both the tip in and out of feedback with the sample. A delay has been introduced to allow the tip to fully approach before the spectral measurement is started. This delay is only implemented when the tip approaches and not when the tip retracts to minimise the measurement time. The delay is set to equal the approach timeout, the timeout is the time delay allocated by the system to allow the tip to approach, the system switches from approaching to approached state when the timeout is reached. The approach time can be reduced by limiting the z range of the piezo's maintaining a slow, safe approach.

A setting allows users to chose the tip out frequency. Tip out measurements can be recorded at no points, every point or at some intermittent value. The disparity in available spatial resolution between near and far-field measurements, due to the difference in illumination size, means that there is little sense in recording a tip out, far-field, measurement at every sample location when the distances covered by the tip are small. The resulting far-field point density can therefore be lower than that required for the near-field speeding up the measurement time.

Further features introduced to the script allow for the pseudo laser scanning as described in Section 5.4.1 and help ease the process of translating between multiple coordinate systems. The coordinate system changes depending on

whether the tip or the sample scanner is in use. Repositioning the tip requires the coordinate system used by the sample stage to be translated. A script was written to automatically calculate the required offset to ensure measurement integrity and allow for the adjustment of the tip position in the laser spot so that the tip spot alignment process becomes independent from the tip sample alignment process. This capability speeds up the measurement process on inhomogeneous samples since the sample does not require re-scanning each time the tip location is altered.

5.5.1 TERS maps on inhomogeneous samples

The process of TERS mapping on in-homogenous samples is more complicated than TERS measurements on homogenous samples since the tip must be aligned to both the sample and the laser spot. We are cautious about over exposure of the tip to the surface which could lead to both tip wear and possible contamination from direct interaction with the sample. This procedure has been designed to limit the time where the tip is in feedback and in close proximity to the sample.

On inhomegenous samples the sample is first scanned using an AFM in either tapping or contact mode depending upon the specific requirements of the topographic image. This provides us with a high definition reference image of the region of interest and ensures the sample is well characterised prior to TERS investigation. We choose to operate our shear-force scans at the minimum scan resolution and with the lightest operable setpoint. The shear-force image is used primarily for locating the pre-determined structure of interest.

The TERS method can be split into three separate operations. The region of the sample to be studied is positioned on the laser axis using the white light image and the coarse positioning screws on the stage. Fine-tuning can be achieved using the piezo stage however it is important that the piezo controlled stage remains largely centred to ensure maximum position flexibility at latter stages of the experiment. Once the sample is centred on the beam and the focus is set the tip is aligned to the beam as discussed in Section 5.4.1.

On certain samples it may be required to displace the sample by a set amount to avoid surface features that may lead to excessive beam distortion, once the tip is aligned to the beam the sample can be returned. With the tip position fixed the AFM is switched to sample scanning mode and a topography image can be obtained of the sample. This is used in combination with the reference AFM image to determine where to take point measurements or a TERS grid. The original location at which the tip is positioned is set to be the origin in the *sample offset* script, any changes in the tip position which may be required to optimise the optical response are then converted into an offset which is applied to the topography coordinates to compensate for the shift in tip position. This allows changes in the tip position relative to the laser spot to be easily implemented and accurately accounted for without requiring any unnecessary scanning.

There is a requirement to rescan the laser spot if the optical conditions at the tip are changed. This is the case whenever there has been any interaction with the microscope such as switching the filter wheel or altering the focus. Over long measurements the focus can suffer from drift and so this is often a parameter that needs re-optimising periodically and can be monitored using the camera. Due to the floating nature of the microscope adjusting the focus implies the need for a full beam alignment however it is possible, on occasion, to carefully tweak the focus to regain TERS performance.

The size, location and grid size are defined for the grid of point measurements using the sample scan topography image. The automated measurement procedure is set in the *Raman Server* script and the script is run which waits for a response from the Renishaw Raman system. A Raman measurement must be set up with the correct measurement parameters. The measurement is started by running the *Remote Raman Measurement* in the Renishaw software which establishes and checks the connection before commencing the series of measurements as defined by the JPK script.

5.6 Single channel APD measurements

The *Global Imaging* path can be used to measure the optical response of a single Raman peak. The tuneable band-pass filters are adjusted to centre on the Raman peak of interest and the intensity of this peak is measured using APD 2 or by taking a snapshot of the CCD.

The APD detector is most commonly employed as the sensitivity of this detector enables rapid collection times and low laser powers. This detection method allows single channel optical measurements in both the near and far-field. Measurements can be combined with un-filtered intensity measurements from APD 1 which is fibre coupled to the microscope port. This second channel allows the intensity of the Raman peak to be normalised against changes in the background intensity. The APD 1 detection path however suffers from lower sensitivity since the signal reaching the detector is attenuated by the mirror in the filter wheel which only transmits a small percentage of the backscattered light. As such utilising a second channel for normalisation is not experimentally feasible for all measurements.

5.6.1 Far-field Raman imaging

Utilising the *Global Imaging* path in conjunction with the JPK scanning sample stage images can be constructed to demonstrate the intensity distribution of a specific Raman peak.

An example Raman map can be seen in Figure 5.9 which shows the G band intensity across a graphitic flake. This method allows images to be collected more rapidly than point spectroscopy, for the same resolution. It is however not as rapid or convenient as utilising a specialised Raman imaging system and only provides information on one spectral peak. As a complimentary technique to characterise the sample in preparation for further measurements it can be of great benefit.

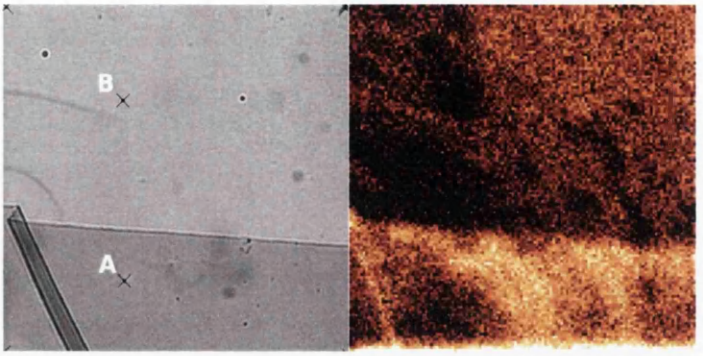

Figure 5.9: Far-field Raman map of graphitic material. Left hand image shows a white light image of the sample with a thick flake extending up from the bottom. Right hand image shows the G band intensity measured using the band-pass filtered *Global Imaging* path on to the APD 2 detector. The Raman map was formed by translating the sample stage and taking intensity measurements at each pixel.

5.6.2 Optical approach curve

Approach curves can be conducted by implementing the force spectroscopy routines in the JPK system. Custom ramps can be programmed in either an open or closed feedback regime. Whilst the tip-sample distance is modulated all of the measurement channels can be recorded allowing the z-height and the APD intensity to be read off simultaneously.

Using the *Global Imaging* path the intensity of a specific Raman peak can be recorded as a function of tip-sample separation. For an active TERS tip the optical response should increase at a highly non-linear rate when within 15 nm's from the sample surface. Due to this non-linear nature the profile of the intensity change with respect to the tip-sample separation can be used to isolate the near and far-field components of the signal [Pettinger et al., 2009].

5.7 Summary

These procedures represent a significant improvement in the usability of the system, particularly by comparison to conducting TERS measurements on the groups previous Veeco system. Increases in the speed of the procedure help

to ensure that the tip is in top operational condition for TERS measurements. Additionally it allows TERS to be a far more useable technique that becomes more routine enabling more emphasis to be placed on investigating sample properties rather than system setup. The ability to script procedures increases the experimental scope and allows far more complex experiments to be designed and conducted. In the next chapter we explore the software that has been developed to collate and review the large datasets that can now be collected during mapped TERS measurements.

Chapter 6

Data Processing and Automation

6.1 Introduction

Conducting experimental measurements across multiple machines, which each run on different operating systems with their own proprietary, non integrated software presents many technical challenges. This is not only the case in collecting the data but also in its analysis. Once the basic challenges are overcome and a localised TERS enhancement can be reliably achieved the real power of the technique derives from doing coordinated mapped measurements to interrogate the chemical composition of a sample with high spatial resolution. These measurements create large sets of data which must be carefully processed to coordinate the optical information provided by the enhanced Raman spectra with the spatial information provided by the AFM.

We have already explored some of the software implementations that have been created for collecting the data, this chapter moves on to discuss the post processing of the data. The post analysis software, written in Python, produces a final experimental output that is easy to review and applies data-processing steps to maximise the clarity and quality of the output. Additionally all measurement parameters and both the raw and processed datasets are stored in a database ensuring that all experimental variables and

results are backed up in one place and well managed.

6.2 Software tools

The tools that have been created have been written in Python [Python Programming Language, 2013] which was a logical language to use since the AFM is scripted in Jython [Jython Programming Language, 2013]. Python and Jython are variants of the same language and so share the same syntax and fundamental rules however Jython compiles to byte code designed to run on the Java platform whilst Python compiles to byte code that runs on its own C based virtual machine. This alters the modules, and hence additional functionality, that can be imported since external modules must share the same base language as the virtual machine or be written in pure Python. The Python language focuses on clear, simple and easy to read syntax that can be written either as a scripting language or as a full object orientated programming language. For this reason alone it is a sensible choice for designing both scripted procedures and more complex analysis tools that require a full class structure to enable complex operations with simple and well structured code.

Python offers us a number of advantages. By sticking to this one language any user looking to modify the operation of the processing software will learn skills relevant to scripting the AFM thus increasing their capability at designing sophisticated scripted measurements. Secondly, the fact that Python runs on a well supported virtual machine means that it runs flawlessly on all operating systems. The only cross platform complications occur if trying to design a full GUI and so only a basic user interface has been employed for this software to ensure full cross platform capability [EasyGui, 2013]. The final advantage of Python is that it is free and open source, has a very large active community of developers and comprehensive help files [Python 2.7 Documentation, 2013]. Since it can use modules written in C there are a fantastic diversity of modules that can be imported which give it the capabilities of equivalent software such as Mathematica and MATLAB. On top of this Python is extensible to work directly with micro processors;

conduct live image analysis on a web cam feed; or integrate directly with web frameworks amongst many others. For the purposes of this project the principle external modules involved communicating with databases, enabling user input, manipulating data and plotting graphs. Test projects were also conducted on using python to analyse live webcam footage through OpenCV [OpenCV, 2013], which could find use for tracking mobile biological cells. Other work was conducted to create and test a web interface that could run the python analysis on a server, via Django [Django Framework, 2013], allowing us to operate with a central database of data for all users. This scheme would allow data to be viewed, rapidly interrogated and analysed on any machine with the bulk of the processing work being conducted on a server. It is the extensibility of Python that is valuable and this opens up a vast array of experimental possibilities. The range of modules is a direct result of the fact that the language is open and not designed for one specific application as is the case for more specialised alternatives such as Mathematica or LabVIEW.

The data itself is stored in a MySQL database [MySQL, 2013]. MySQL was chosen as it is one of the most prevalent database languages and most notably it is the database on which most of the web is based. It is, like python, open source and interfaces well with the Python language. Using a database is not the only option we had available. A simple file structure approach would also have worked whereby all the data files for a particular measurement could be stored in one folder. This would however be a far less powerful way of achieving the same outcome and could potentially be awkward to use. The database allows all data from both the Raman and AFM measurements to be stored in one place along with all measurement parameters for both systems and information about the tip and sample used for the measurement. The nature of MySQL allows the database to be rapidly interrogated so, for example, if you were interested in finding out what tips produced an enhancement above a certain contrast value on a specific sample then these parameters can be given to the database as a query and the set of measurements that satisfy the query are returned. Cross interrogation opens up the possibility of more interesting lines of enquiry that otherwise would

be time consuming to achieve.

By entering each measurement into the database we can also be sure that all the relevant parameters are easily accessible in the future ensuring the integrity of the dataset. The process of entering data into the database is as we will see automated making it a simple, user friendly process. The database becomes evermore useful over time as the quantity of experimental information increases. Thus it can becomes a key record of progress and documents changes in the system particularly if standardised measurements on a control samples are regularly undertaken.

6.3 Software

The following section describes in detail the processing steps which are employed, graphical representations of the software procedures are displayed to allow clear visualisation of the processes involved.

6.3.1 Data input

Figure 6.1 provides an overview of how data is extracted from the raw data files and configured for input in to the database where it is permanently stored and in a format that facilitates a number of post processing steps. The processes described here are specifically aimed at mapped measurements as these are more complex and present both greater challenge and interest when it comes to batch processing. The routines however also work for single point measurements.

When a mapped measurement is undertaken the primary concern is linking Raman spectra with their physical positions on the SPM image. The JPK SPM image is saved in ascii format with scan parameters and coordinate information, such as the rotation and offset of the image, saved in the file preamble. This contains everything we need to map the Raman data back on to the topography image, however it does not save the spectral measurement coordinate list. This coordinate list is passed to the Renishaw system by the RamanServer script which controls the mapped measurement. The

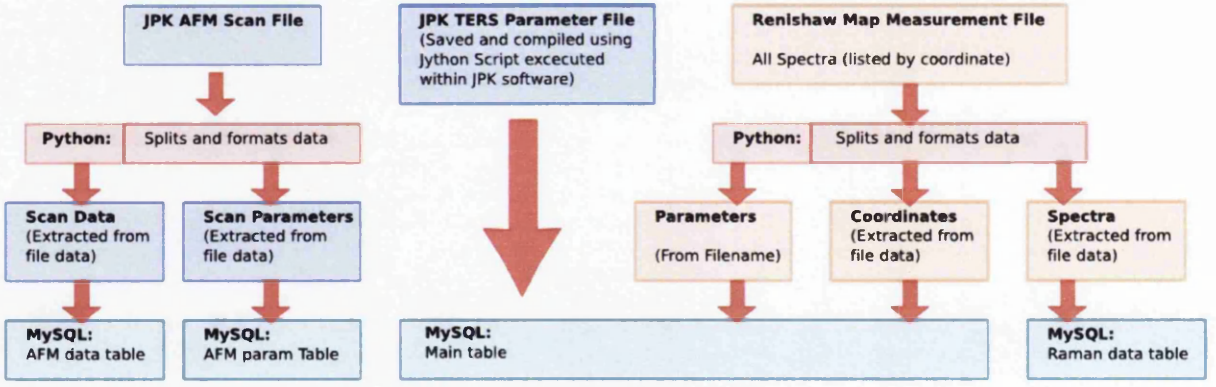

Figure 6.1: Schematic showing how measurement data is extracted from the Renishaw and JPK systems, formatted and entered into a relational MySQL database.

measurement coordinates are saved within the Raman map measurement file.

The Raman spectra are saved in a proprietary format that requires conversion using the Renishaw batch converter to ascii format. The resultant ascii file contains four columns which are the x and y SPM coordinates followed by the wavenumber and the Raman intensity. This list of data contains all the spectra in the mapped measurement which can be separated by their coordinate. To extract the coordinate list unique combinations of the x and y coordinates must be found. The spectra are then separated according to the measurement coordinate.

The Renishaw file system does not allow access to the Raman measurement parameters. A system has been designed to store the parameters in the filename in a way that is consistent, easy to input by the user and easy to automatically extract using Python. All measurement parameters are stored in the filename, as demonstrated in Figure 6.2, in the format of a list separated by underscores and where the value is separated from its variable name by an equals sign. The structure can be converted to a Python dictionary, which is the primary look up table structure utilised by Python.

```
date=120502_tipID=NSS59_sampleID=SWNT1_centre=ext_obj=100X_con=0
_PH=1_RP=1_filter=1%_acqu=60_posID=A-map_rep=2_tipIn=0
```

Figure 6.2: Example of the filename structure used for Raman measurements.

The final set of parameters are stored by a script on the JPK system which correlates the tip position, sample position, scan ID, setpoint and measurement time with the position ID. This ensures the parameters used by the SPM are recorded at the time of Raman measurement since these parameters are often different from those used during the SPM topography scan. The scan ID defines which topography scan has been used to guide the choice of sample position and the position ID is used to relate this data with the Raman data.

The python software gathers all the above parameters and data and formats them for input into the database. The database features a relational

structure whereby multiple tables are utilised and which are linked by a common identifier. The identifier is unique for each measurement and is formed from the measurement ID (e.g. C4map), the spectrum centre (1500), the position ID (p0) and the tip approach status (t1 or t0), the identifier for this measurement would then be: *C4map_1500_p0_t1*. This format is human readable and allows the table ID to be guessed without querying the main table if needed.

There are four linked tables, and their relational nature is illustrated in Figure 6.3. The main table stores the measurement parameters and numerical outputs from the processing steps. This table is the first port of call and can be queried to identify which spectra or AFM datasets are of interest. The AFM data is stored in two tables linked by the ScanID, the topography data and SPM parameters are stored separately. The final table contains the raw Raman data, linked by the TableID, and is also used to store the processed Raman spectra.

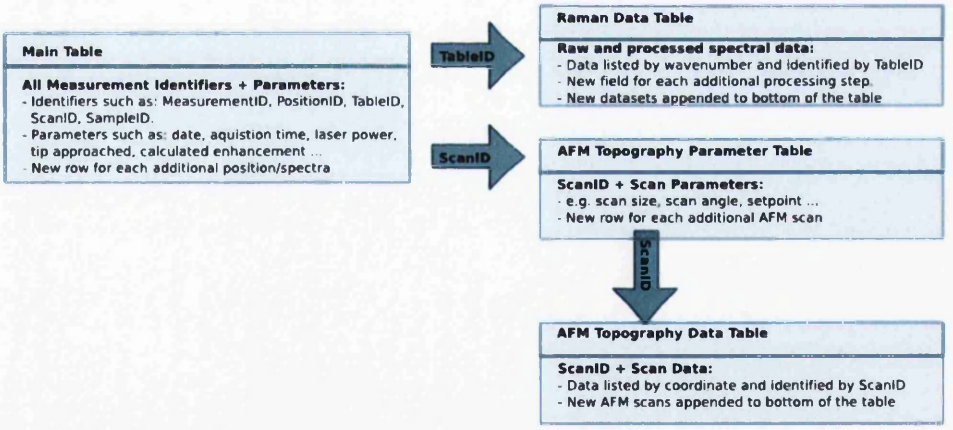

Figure 6.3: Schematic showing the relational structure of the MySQL database. The Main Table is the primary table that contains the measurement parameters and dataset information. This is linked by the TableID and the ScanID to the Raman and SPM data respectively.

6.4 Post processing

Figure 6.4 demonstrates the procedure used to handle and process data once in the database. The Python code asks the user which data needs processing and structures the response to form a query. MySQL responds to the query by providing the corresponding $TableID's$. The python script passes this to the next stage in the Python code which formulates another query to extract each spectra from the data table. MySQL returns the data which is then processed using the desired processing steps. The processed data is then written back to the database as a new field maintaining the original data and ensuring all processing steps remain accountable.

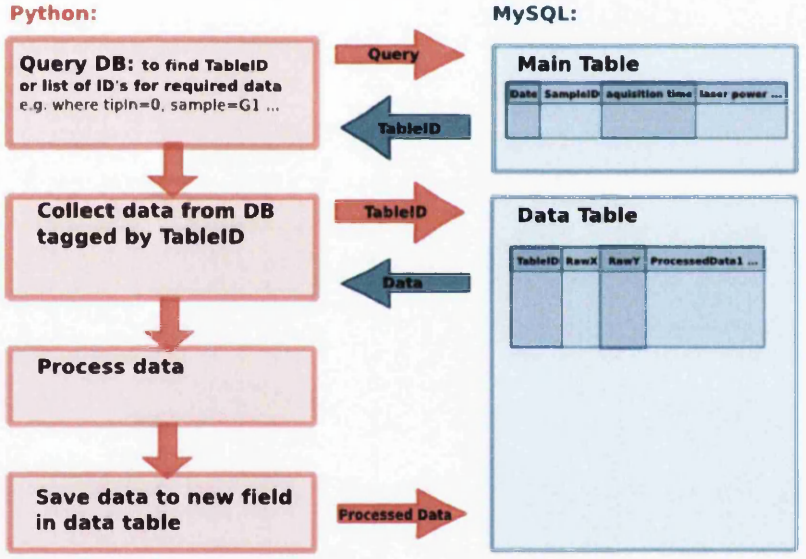

Figure 6.4: Schematic illustrating the Python routine used to extract data from the MySQL database, process it and then return the output back to the database.

6.5 Processing routines

A summary sheet, shown in Figure 6.5, is created for each processed spectrum in the database. This sheet plots each of the processing steps detailed below and allows the user to check that the parameters for the processing are

appropriate. This alleviates the dangers of blind processing which without sufficient care could result in artefacts and distorted data. The routines described in this section are implemented on all the data-sets, the summary sheet facilitates rapid review of the data.

6.5.1 Rolling circle filter

The rolling circle filter is an adaptive filtering process which acts as a high pass filter [Brandt et al., 2006]. It is useful for TERS analysis since it can separate the Raman signal from the underlying fluorescent background allowing the analysis of each of these optical contributions independently. With the tip present there is often a change in the broad background structure that underlies the Raman signal. This background originates from fluorescence and diffuse scatter. By removing the background the height of the spectrum at a particular wavenumber becomes a good approximation of the Raman peak height. This allows Raman peak intensities to be more easily mapped and contrast values to be automatically calculated. The adaptive nature of the technique means that the the background does not require fitting by a function and so no knowledge is required of the background profile prior to the implementation of the filter. With care over the choice of parameters and ensuring that these parameters are consistent across all spectra in a dataset the rolling circle filter can be applied to an entire series of measurements.

The mechanism utilised by the rolling circle filter is, as suggested by the name, analogous to a mechanical like process. A circle with a defined radius is pushed up from below until it touches the data the touching point is then recorded. This process is repeated for each position along the x axis and thus the circle is 'rolled' along the data. The filter works because the circle when correctly defined cannot push into the small width of the Raman peaks but is able to fully trace the underlying background as demonstrated in Figure 6.6.

Multiple adaptations of this concept were tested, tracing the height that the circle can reach for each wavenumber becomes flawed when the background shape becomes steep since the filter output pushes away from the data on these steeper faces. We thus settled upon a process which lists all of the

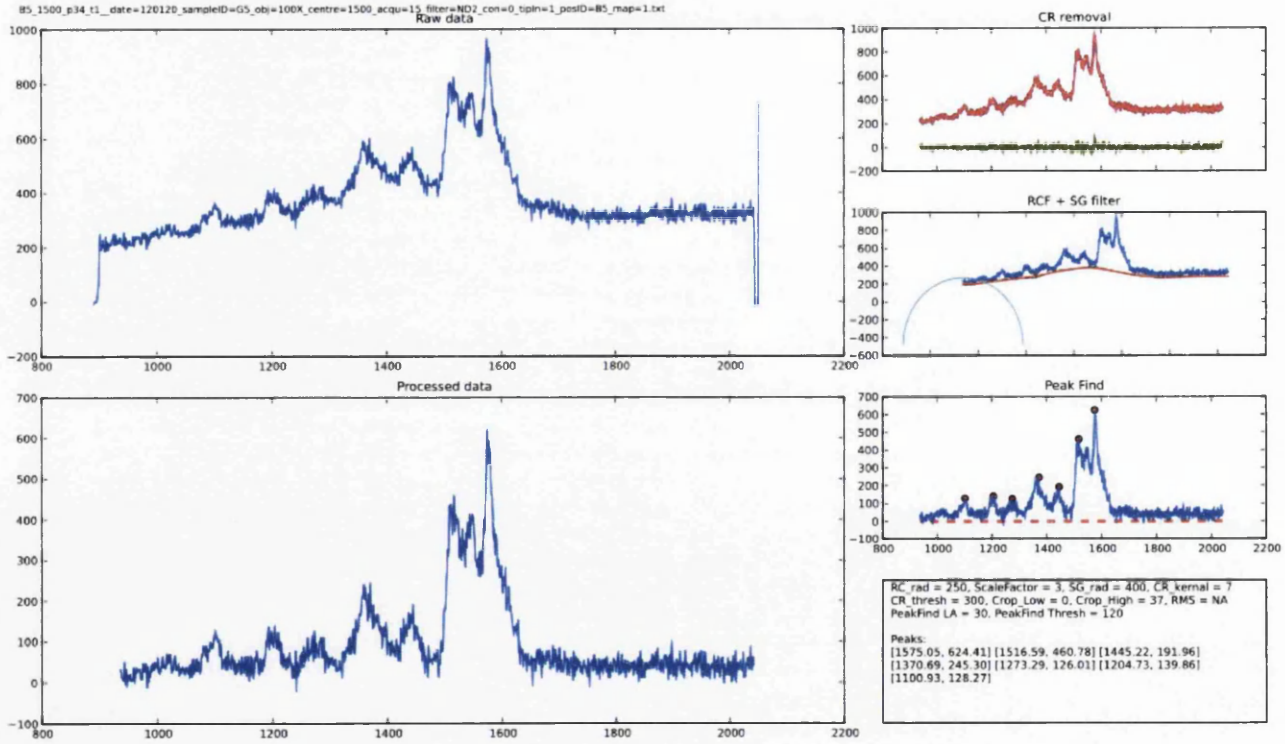

Figure 6.5: Summary sheet that is output for every individual spectrum in the dataset enabling the quick review of all processing steps undertaken. The left hand column of the image displays the raw data (top) and the final processed data (bottom). Each processing step is plotted on the right hand column. From top to bottom the plots display the output from cosmic ray removal, background subtraction, peak detection and filtering parameters.

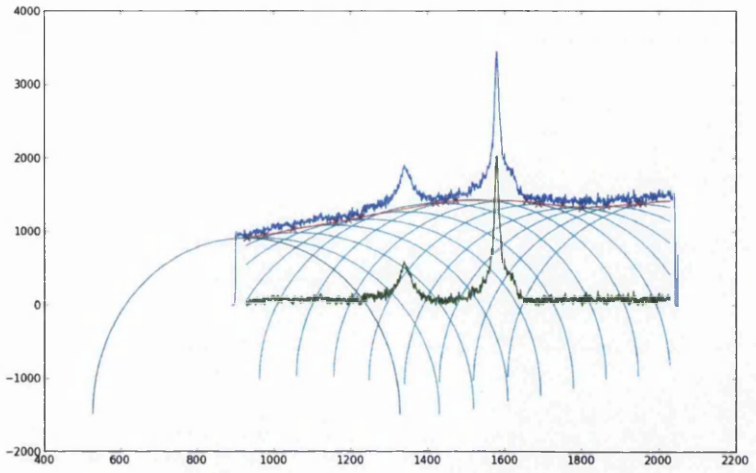

Figure 6.6: Demonstration of the rolling circle filter in operation. The raw data is shown in blue. For each member of the data array the circle (light blue) is raised to meet the data, points where the circle touches the data are marked by purple crosses. The red line represents the background signal which is produced by interpolating across the touch points and applying smoothing. The background corrected output is plotted in green.

unique touching points, linearly interpolates these points before a Savitzky-Golay filter is employed to create a smooth representation of the background. This reliably reproduces the broad line shape of the background. The main problem with the rolling circle filter for our application is that its height is offset by the size of the noise on the data. The RMS noise is often seen to increase in TERS measurements with the tip in feedback. This can introduce an error into the automated calculation of contrast values due to differing constant offsets in the background between tip in and tip out. This issue is easy to correct for, however it is worth noting since it is a particular problem when there is a low signal to noise. For TERS measurements low signal to noise ratios are often encountered during mapped measurements where speed is a priority. Despite this the isolation and removal of the background signal allows better evaluation of the enhancement levels than if the background was left in since the background changes can often be far more intense than

the difference in the Raman signals themselves.

The primary tuneable parameters of the rolling circle filter is the circle radius which effectively sets the filter cut-off and so thresholds which peaks are considered as Raman or background signal. The circle radius should be roughly twice the width of the broadest Raman peak. The second parameter is the Savitzky-Gollay radius. The SG filter performs is a low pass filter that is often used to smooth Raman data as it is one of the best filter techniques for preserving the peak shape. It applies a local polynomial fit, using a 3rd order polynomial. The radius in the case alters the window size over which it is conducting the fit. The window is centred upon the current data point and the SG radius effects how rapidly the filter can respond to changes in the interpolated line shape. The output is fairly tolerant to this value and typically it should be chosen to be twice the circle radius. When running this filter the circle and SG radius are tuned on a representative spectra before being applied to all spectra in the dataset. With the same parameters the filter response is consistent thus making it a useful tool for mapped measurements. An additional parameter is the scale factor which is used to scale the circle height to suit the aspect ratio of the data. Without this the circle will present itself as a flat horizontal line to high intensity datasets.

6.5.2 Cosmic ray removal

The data is cleaned to remove cosmic rays. This utilises a filter which isolates large magnitude, high frequency peaks. A small kernel, 7 pixels wide, is passed along the data. The magnitude of the intensity at the centre of the kernel is compared to the median intensity of the kernel. If the difference between these values passes a threshold it indicates a cosmic ray. The cosmic ray is replaced with the median value.

This filter is unable to fully remove very large cosmic rays which can feature a base width larger than the kernel. It does however always remove sufficient intensity that the resulting peak does not dominate the spectra and force a large y range. The filter can be further optimised by utilising multiple passes and tuning the thresholds in each case. Since the goal of this

process is to produce a representative visual output and not to produce the final spectra for publication we are satisfied with the product of one pass of the cosmic ray filter.

This stage of the filtering also removes the head and tail of the spectrum to remove the drop in intensity produced by the mismatch between the CCD length and the image of the Raman signal projected by the spectrograph.

6.5.3 Peak detection

A peak detection module was imported [PeakDetect, 2011] that identifies peaks based on the intensity and local gradient. Peaks are identified and tagged in the database for future lookup. The peak positions are also marked on spectrum summary sheet to enable changes to the thresholds to be made and enable appropriate sensitivity of the peak detection.

6.6 TERS measurement summary sheet

The most important output from the script is a summary sheet, as seen in Figure 6.7, that is produced for each measurement position in a series and evaluates both the tip approached and tip retracted data. This correlates the enhanced TERS response with the physical location on the sample and calculates contrast factors for any identified peaks in the tip approached spectrum.

The summary sheet allows comparison of the spectral response between measurement locations enabling the resulting signal to be identified in the context of the changing sample structure. The raw data is displayed in the left hand column and the middle column displays the processed data. The top row of these columns shows both the tip approached and tip retracted line shapes while the bottom row shows the pure TERS response that is produced by subtracting the tip retracted signal from the tip approached signal and shows us the signal that is derived from the localised enhanced field at the tip apex.

This standardised output allows trends in the data to easily and reliably be

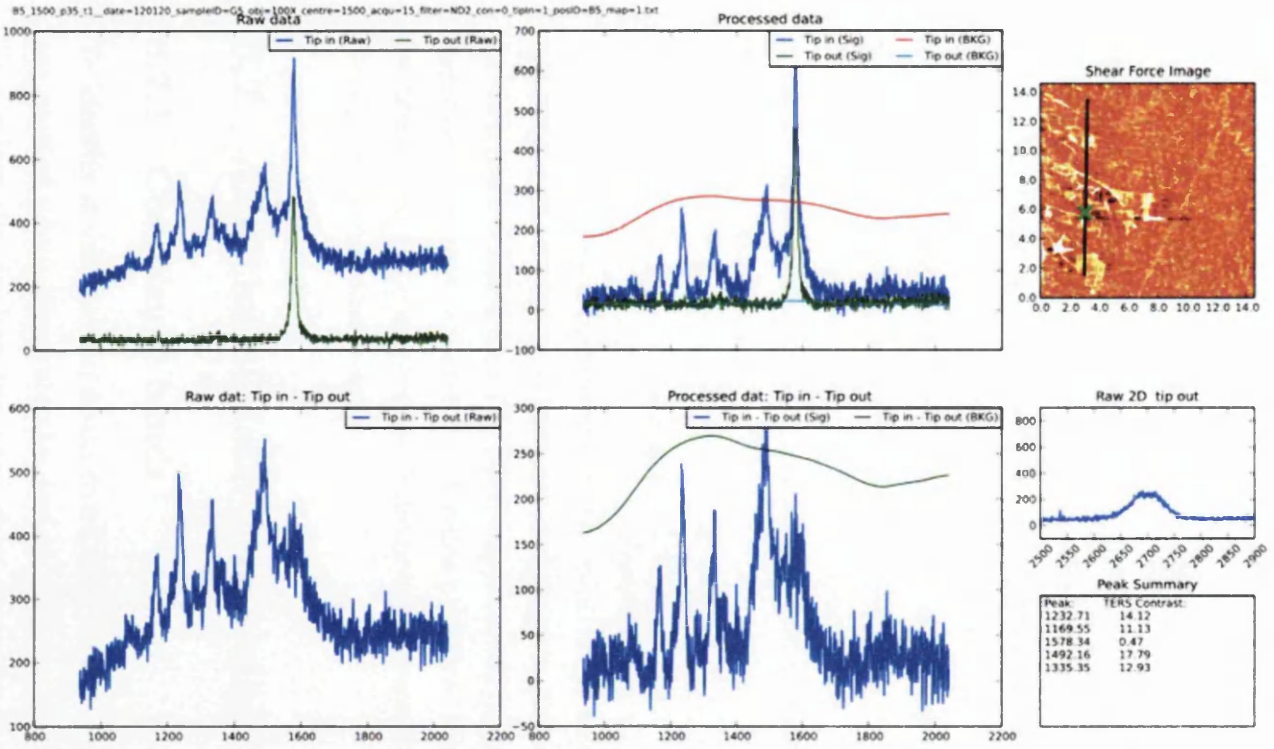

Figure 6.7: Example of a TERS measurement summary sheet, the data displayed shows the TERS response on a graphene flake. The top row displays the near and far-field data. The left hand column shows the unprocessed data, the processed data is displayed in the middle column. The bottom row displays the TERS response that is calculated by subtracting the tip retracted signal from the tip approached signal revealing the signal that can be attributed to the presence of the tip. The right hand column plots the physical location of the measurement on the SPM topography image which also shows the rest of the measurement line. The box below allows additional spectra to be plotted which in this case is the 2D peak of graphene for that sample location. The final box calculates the TERS contrast for the previously identified peak positions.

identified. Any problems in processing routines can also be observed through direct comparison to the raw data. The contrast calculations allow a rough contrast value to be ascertained.

6.6.1 TERS contrast

TERS contrast has become the accepted value to use when comparing enhancement levels between tips and samples. The contrast represents the difference in signal intensity with and without the tip present, as shown in equation 6.1, it thus quantifies the signal increase. Background subtracted data is used for contrast calculation. Enhancement factors can also be calculated which also take into account the difference in optical scattering volume between the near and far-field measurements. This produces large values however is based upon the assumed sizes of the near and far-field volumes which leads to large errors in the calculation.

$$Contrast = \frac{I_{approached}}{I_{retracted}} - 1 \tag{6.1}$$

In the processed measurements the contrast is calculated by taking the intensity of the background subtracted tip approached and tip retracted data for each peak position found in the tip approached dataset. This gives a good approximation that is useful for reference purposes. Some error is introduced by differences in the magnitude of the noise between the tip approached and the tip retracted measurements.

6.7 Additional data processing

6.7.1 Confidence bands

To identify stable Raman peaks from time varying peaks confidence bands are plotted which illustrate the deviation in the peak intensity with time. To conduct this analysis repeated short acquisitions are required with the tip in feedback on the surface. The standard deviation across all datasets is

calculated for each wavenumber. The 95% confidence band is plotted which is equal to 1.96× the standard error.

6.7.2 SPM topography

To limit tip wear and to not delay the TERS procedure topography images with TERS tips are limited to low scan resolutions, small areas and light set points. This does not produce the best imaging quality however provides sufficient information about the sample to identify measurement locations when used in combination with detailed contact mode AFM topography images that were recorded in prior characterisation of the sample.

Often we choose to combine the shear-force and AFM images to utilise the positional information provided by the shear-force image to which measurement coordinates can be plotted. The higher resolution AFM image is then superimposed on top and adjusted to match the topographic features visible in the shear-force image. An example of this is shown in Figure 6.8 The top left corner shows the underlying shear force image that was used to locate the physical TERS locations.

Figure 6.8: Example of a shear-force topography image (revealed top left corner) overlaid with a high resolution contact mode AFM image and markers indicating a series of TERS measurement positions. The measurement positions are defined based on the shear-force image. Features are matched between the shear-force and AFM images to ensure accurate alignment is achieved.

6.8 Summary

The software methods that have been developed through this work are a significant output of the project. In modern computer controlled systems much additional power can be gained from software by enabling large automated measurements and sequenced procedures. To cope with the volumes of data automated processing and data handling are also highly important. Without these techniques the mapped measurements demonstrated in chapters 7 and 8 would not have not been feasible. The methods and software, presented in this chapter and previously, have made a large contribution to the results in this thesis and have allowed the separate SPM and Raman systems to work together effectively and efficiently.

Chapter 7

TERS on Thin Films.

7.1 Introduction

Thin films present a strong testbed for TERS development. Their homogenous nature allows the alignment of the sample to the tip to be neglected which removes a complex step from the TERS procedure and allows experiments to focus on the optical configuration and tip properties.

This chapter presents data from two different molecular films. The first film is of Rhodamine 6G (R6G) which is a dye molecule and exhibits a Raman response that is resonant with 532 nm illumination. Four sets of measurements are investigated on this sample which are:

- SERS measurements using gold nano particles
- A far-field comparison of a 50 nm thick R6G film on glass and an ultra-thin (~monolayer) R6G film on gold
- TERS of a $50nm$ film of R6G on glass
- Gap-mode TERS of an ultra-thin (~monolayer) R6G film on gold

The second half of this chapter investigates a self assembled monolayer of thiophenole molecules adhered to a gold substrate. All TERS measurements conducted in this section are operating in gap-mode configuration. The main focus of our work has been to obtain enhancements using a solid, etched Ag tip with 532 nm radially polarised illumination. Other experimental variations have been explored on the thiophenole sample which include:

- $\lambda = 532nm$, solid Ag tip
- $\lambda = 785nm$, solid Ag tip
- $\lambda = 532nm$, Ag coated Si tip

The results presented in this chapter are used to explore themes relevant to the development of our TERS system and aid us in understanding the success and limitations of the instrument. The themes explored are: Surface-enhanced Raman scattering (SERS); background fluorescence; temporal fluctuations of the Raman modes; gap mode TERS; solid and coated tips; and illumination wavelength.

7.2 Rhodamine 6G

7.2.1 Introduction

Rhodamine 6G is a dye molecule that is resonant under 532 nm illumination which results in a strong Raman response. The resonant condition means that the Raman cross section is maximised for this wavelength leading to efficient scattering [Meyer et al., 2010]. R6G and other dye molecules have been used in many TERS studies since they are responsive and easy to work with. For this reason they are prime candidates to test different experimental configurations. Stöckle et al. [2000] conducted the first ever successful TERS measurements on BCB dye molecules thus dye molecules have been considered one of the most favourable test beds right from the very origins of the technique.

Table 7.1: Selected examples of TERS measurements conducted on dye molecules

Publication	Dye	Config.	Tip	$\lambda[nm]$	Power $[mW]$	$Acqu.[s]$
[Hayazawa et al., 2002]	R6G on glass	side	Ag coated	532	0.034	10
[Yeo et al., 2007]	BCB on glass	bottom	Ag coated	488	2-5	5
[Downes et al., 2009]	R6G on glass	bottom	Au coated	532	0.069	60
[Schultz et al., 2008]	R6 on Au	top	Au NP on AFM tip	514	3	-
[Peica et al., 2009]	Rose Bengal	UHV side	Au & Ag Coated	488	¡100	-

Rhodamine 6G is a well characterised molecule. Table 7.1 details the experimental configurations and measurement conditions used by different groups working with dye molecules. The molecular structure of Rhodamine 6G is shown in Figure 7.1. The aromatic carbon bonds that are present

in the structure are the primary reason for the strong Raman signature in Rhodamine. The spectral peak allocations are displayed in Table 7.2 which shows that the dominant contributions originate from vibrations between carbon atoms. These peaks are marked on each of the Rhodamine spectra to aid comparisons between datasets.

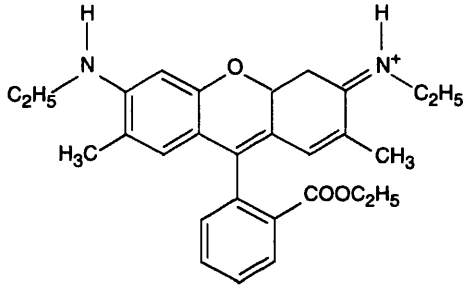

Figure 7.1: Molecular structure of Rhodamine 6G [Hayazawa et al., 2001]

Carbon bonds have a large Raman cross section and so produce intense Raman peaks [Weber and Merlin, 2000]. This facilitates short collections at low laser powers. This is important for TERS measurements since heating effects at the tip can degrade the enhancement and cause damage to the sample which sets a low threshold on the laser power that can be used. Short collections, as has already been discussed, are vital when progressing to mapped TERS measurements.

Table 7.2: Rhodamine 6G peak assignment [Hayazawa et al., 2001]

Raman shift $[cm^{-1}]$	614	776	1365	1510	1579	1652
Assignment	C-C-C ring	C-H bend	arom C-C str	arom C-C str	arom C-C str	arom C-C str

Data presented in this section features SERS spectra obtained from nano particle clusters alongside results from three TERS tips. One of the TERS measurements has been conducted on Rhodamine deposited on glass (tip *R*.1), the other two tips were used in gap mode configuration with a sample composed of an ultra-thin Rhodamine film adhered to a gold coated glass coverslip (tip *R_Au*.1 and *R_Au*.2). The data has been selected to demonstrate enhanced spectra and additionally to demonstrate transient signals thought to derive from local carbon contamination.

7.2.2 Sample preparation

A Rhodamine solution was created by dissolving one level spatula of Rhodamine in $5\mu L$ of ethanol. It was not possible to measure the exact concentration due to a lack of sensitivity of the available balance. The concentration was also further diluted on deposition and so the final concentration of Rhodamine dropped on the sample is unknown.

Preparation of R6G on glass

To prepare Rhodamine on glass a micro pipette tip was used to draw a droplet of the R6G solution using capillary forces. This was touched against the coverslip to deposit a small droplet on the surface. The droplet was spread around using the end of the pipette tip. A drop of ethanol was then added which created a concentration gradient dispersing the R6G towards the outside of the coverslip. This was left to dry producing a deposition that increased in thickness away from the centre of the coverslip. The centre of the coverslip showed a light pink coloration whilst thicker regions at the outer extents of the coverslip showed a vibrant pink coloration. In the microscope regions of varying thickness could be seen due to colour variation. There were many large homogenous regions of the sample that appeared of consistent thickness. TERS measurements could be performed with sufficient tolerance in the sample position to allow the sample to be moved between measurements ensuring the data was collected on fresh un-bleached regions of the sample.

The lowest thickness region of the sample was selected for TERS measurements with tip $R.1$. This area expressed a light coloration and the rhodamine film was measured to be $50nm$ in thickness. The film thickness was determined by scratching through to the glass surface with an AFM probe.

Preparation of R6G and gold nano particles for SERS

The SERS sample was produced using the same procedure as above however the drop of ethanol was replaced by a drop of 30 nm gold nano particles in suspension in ethanol. This allowed the gold nano particles to disperse amongst

the Rhodamine and settle on the glass surface once dry. Measurements were performed on and off large agglomerations of the gold nano particles.

Preparation of R6G on a gold coated coverslip

A glass coverslip was coated with a $5nm$ thick layer of gold using a desktop sputterer. A droplet of Rhodamine was added following the same method as above and spread across the surface. This was left to dry before being rinsed thoroughly with ethanol. This process removes excess R6G molecules that are not directly adhered to the gold substrate creating an ultra-thin molecular film on the surface that is close to one monolayer in thickness [Pettinger et al., 2005]. The final surface has little coloration. The gold film darkens the coverslip which results in an attenuation of the laser illumination at the tip, the attenuation is $\sim 50\%$ and depends on the thickness of deposition.

7.2.3 Far-field Raman of R6G on glass and on gold

The far-field Raman response of Rhodamine 6G demonstrates a dependance on the underlying substrate and sample preparation. The far-field spectra for Rhodamine on glass and Rhodamine on gold are displayed in figures 7.2a and 7.2b respectively. The principle Raman modes for Rhodamine are marked by the vertical grey lines on the plot, this is continued for all subsequent Rhodamine spectra for ease of comparison. The peak positions are: $614, 776, 1186, 1310, 1365, 1510, 1579$ and $1652cm^{-1}$. The spectra for Rhodamine on both substrates share the same set of peak positions. The fluorescent background, scattering intensity and peak definition however differ considerably. The sample on glass (figure 7.2a) demonstrates an order of magnitude more counts on each rhodamine peak than the sample on gold (figure 7.2b), this is however coupled with increased peak breadth and subsequently reduced peak definition. The fluorescent background signal forms a substantial contribution on the glass sample whereas there is little background signal observed on gold.

The samples differ both in their substrate and in their preparation. As such care has to be taken when considering a direct comparison. The increased

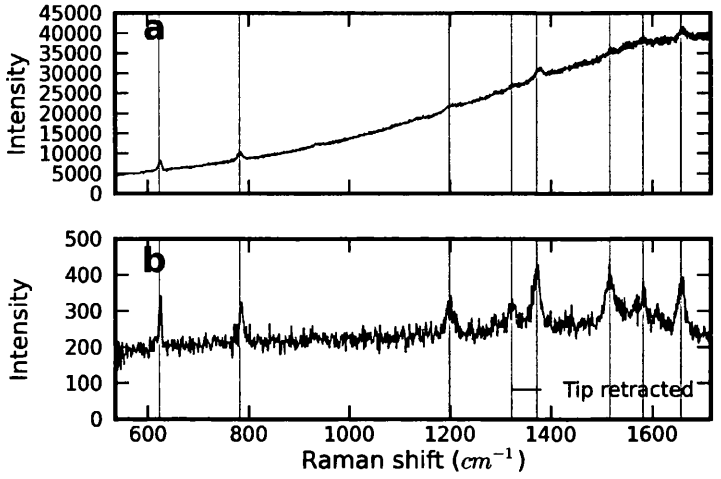

Figure 7.2: Far-field Raman spectrum of a $\sim 50nm$ thick R6G film on glass (top) and an ultra-thin R6G film on a gold coated coverslip (bottom). The spectra were collected using $532nm$ illumination with a 5s acquisition and 0.05% ($7\mu W$) laser power. No background subtraction was performed on this data.

Rhodamine thickness observed on the glass sample will contribute to both the signal and background intensity since there are more molecules in the laser focus scattering light. This may also explain the reduced peak definition since the increased film size presents a less well defined system than the monolayers adhered to the gold surface.

The difference in fluorescent background is not solely dependant on the Rhodamine thickness but will also be affected by the substrate. This can be seen not just in the magnitude but also the profile of the background which features a strong gradient peaking around $1700cm^{-1}$ on glass, on gold it is far flatter and peaks earlier around $1500cm^{-1}$. The gold film provides a non radiative decay channel that quenches the fluorescence background signal through energy transfer from the molecule to the metal [Hayazawa et al., 2002]. This decrease in unwanted optical scattering causes a significant improvement in the ratio of Raman signal to background.

The Rhodamine on glass sample suffers from rapid degradation due to photo-bleaching, the Raman peaks drop to half their initial intensity after 25s of laser exposure at 0.05% laser power, this is compounded by the poor peak

definition to place a severe restriction on measurement times. The colour of the sample, when working on thicker material, can also be seen to change from yellow to purple following laser exposure. The Rhodamine on gold sample demonstrates far greater tolerance to laser power and requires 100 s of laser exposure to decrease the Raman response by 50%. The peaks for this sample still maintain good definition despite this drop in scattering intensity enabling longer series of measurements to be conducted, however it is still important to bear in mind that attenuation over longer time frames must be taken into account. It is important for both samples that the sample is moved to a fresh location between measurements thus minimising the impact of photobleaching and ensuring comparable results.

The increased resilience to laser power found on the gold sample originates from a number of sources. The gold substrate helps to dissipate heat from the laser focus away from the dye molecules reducing damage to the molecules. There is a secondary contribution from the gold film which causes a darkening of the surface, this results in a $\sim 50\%$ attenuation of the laser at the sample surface. The improved resilience of the gold sample allows larger laser powers to be used improving the signal to noise enabling short collection times.

The gold surface is likely to also provide small levels of SERS enhancement. The spluttered surface is not atomically smooth and so local irregularities in the surface can create enhancing hotspots which boost the Raman scattering intensity from the dye molecule. This is something that is hard to directly measure but SERS effects will result in increased signal intensity from ultra-thin films and may improve peak definition over short acquisitions. The peaks observed on the thick Rhodamine film on glass are both more intense and broad, this is a result of the increased number of molecules undergoing scattering in the laser focus.

7.2.4 R6G SERS measurements using Au nano particles

Surface enhanced Raman spectroscopy (SERS) exploits the enhanced field created by metal nano particles. This is a plasmonic effect analogous to TERS.

SERS measurements feature multiple hotspots originating from many nano particles that are illuminated by the laser focus therefore the overall SERS system differs substantially from TERS because the scattered signal derives from many enhancing particles. The strongest Raman scattering occurs from molecules that lie directly between pairs of enhancing nano particles where field enhancement is the greatest. This means that the strongest signal originates at nano particle clusters.

Large nano particle clusters are visible in the optical microscope as can be seen in Figure 7.3a. A grid of far-field measurements was taken across the clusters. Figure 7.3b shows a thresholded colour map of the same region of the sample. The intensity of the $614cm^{-1}$ peak is mapped, coloured squares mark an intensity reading above the intensity threshold and indicate enhanced spectra. The colour scale, from red to black, depicts the magnitude of the enhancement from high to low intensity respectively. The locations showing enhancement correlate strongly with the locations of nano particle clusters which are seen in the white light image. Moreover the scale of the enhancement largely correlates with the apparent size of the nano particle cluster.

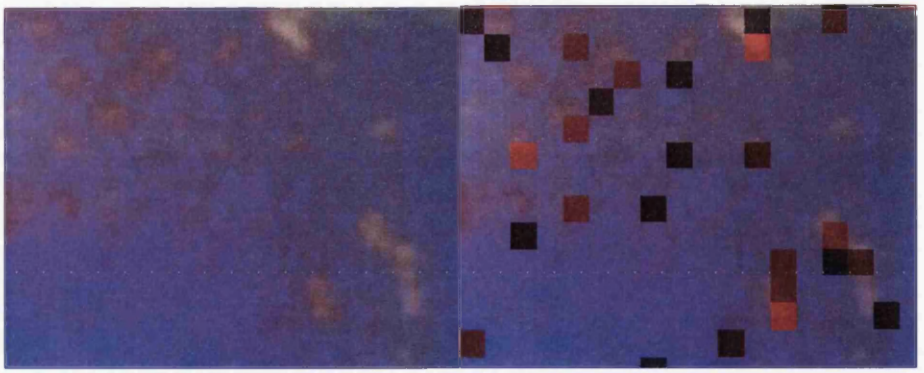

(a) Optical micrograph **(b)** Far-field Raman intensity

Figure 7.3: (a) $17 \times 14\mu m$ microscope image of clustered 30 nm gold nano particles on Rhodamine 6G. (b) The far-field Raman colour map of the same region depicting areas of high intensity of the $614cm^{-1}$ Raman peak. Increased Raman intensity corresponds to locations where nano particle clusters are visible in the optical microscope.

The Raman signal undergoes substantial enhancement at the nano particle

clusters, Figure 7.4 shows the difference in spectral signature between when the objective is centred upon a highly enhancing cluster and when it is not located above a cluster. This data shows a mean SERS contrast of 7.3 ± 1.2 the error value takes into account the variation across each of the spectral peaks for the enhanced and non enhanced data.

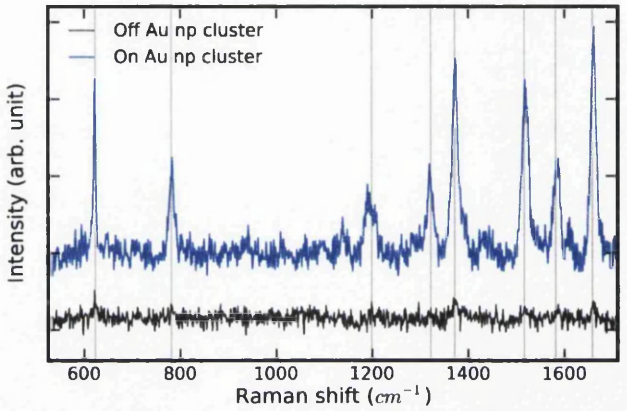

Figure 7.4: SERS spectra of Rhodamine. Blue and grey spectra represent the spectral signature with the objective centred on and off a nano particle cluster respectively. Spectra were recorded with an acquisition time of 2 s at 0.05% ($26\mu W$) using 532 nm illumination and have been background corrected. The dominant Raman peaks are marked which lie at: $614, 776, 1186, 1310, 1365, 1510, 1579$ and $1652 cm^{-1}$

This level of contrast is significantly greater than the contrast that has been observed for TERS measurements. Nano-particles create plasmonic, enhanced fields using very similar mechanisms to a TERS probe. The primary difference is the confined geometry of the nano-particle which influences the nature of the enhanced field and will determine the plasmon resonance. SERS however has a statistical advantage. Large clusters of nano particles 100's of nm's in size sit in the laser focus which allows many R6G molecules to be positioned at the optimum position for enhancement between closely separated nano-particles. These conditions ensure that there are many enhanced scatterers. As such there are many hotspots in the laser focus and this is able to produce high contrast values that we have not been able to replicate with TERS. Since we do not know exactly how many hotspots are being collected over we cannot

calculate a SERS enhancement factor for this measurement.

To achieve maximum enhancements for gap-mode TERS the correct tip, whereby the geometry of the apex supports a strong plasmon resonance, must be held in very close proximity to the gold substrate and a Raman active molecule must sit between the tip-substrate interface. The likelihood of this is reduced compared to SERS where the shear number of particles will ensure that there are many optimum gap mode hotspots that sandwich the Rhodamine molecules between active nano particles. SERS is helpful when it comes to giving increased sensitivity to weak Raman signals however it provides little additional information in the way of localisation. With careful tagging, nano particles can be used to produce localised signals thus acting as targeted reporters however this requires permanently altering the sample system that is being studied.

7.2.5 TERS measurements of R6G on glass

Stable TERS enhancements were achieved on the Rhodamine on glass sample. Figure 7.5 shows a typical TERS enhancement for tip $R.1$. Signal to noise ratios are poor due to the limitations of the sample, as already discussed, the sample suffers rapid degradation from photo bleaching. A laser power of $7\mu W$ and acquisition time of 2s were used to ensure that observed changes in the Raman signal were a product of the tip interaction and hence demonstrate a true near-field enhancement.

Experiments were carefully conducted to guarantee that a new sample location was used with each pair of tip in and tip out measurements and exposure of the laser to the sample was minimised. The TERS spectra plotted in Figure 7.5 have undergone background subtraction and have been offset for clarity. The enhanced Raman peaks show an average TERS contrast of 1.2 ± 0.3. The peaks are broad and poorly defined when compared to the SERS data and the R6G on gold sample. A lack of peak definition was similarly observed in the far-field only measurements on this sample presented in Figure 7.2. The enhanced signal does not appear to improve the peak definition which would be a sensible hypothesis based upon the signal

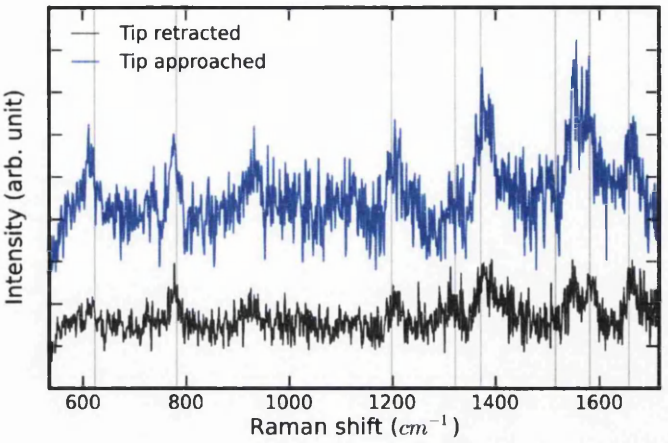

Figure 7.5: TERS spectra of Rhodamine 6G on a glass substrate using tip $R.1$. Low signal to noise since collection times are restricted by the rapid photo bleaching of the dye. Spectra were recorded with an acquisition time of 2 s at 0.05% ($7\mu W$) using 532 nm illumination and have been background corrected. The dominant Raman peaks are marked which lie at: $614, 776, 1186, 1310, 1365, 1510, 1579$ and $1652 cm^{-1}$.

localisation provided by the tip. This may be a result of the poor signal to noise which also hinders accurate representation of the enhanced line shape. Enhancement can be seen across all of the rhodamine peaks which lie within this spectral range.

TERS measurements of R6G on gold

A typical TERS enhancement can be seen in Figure 7.6 for tip $R\_Au.1$ on the gold coated Rhodamine sample. The spectra do not show exceptional contrast. The average contrast for the enhanced peaks is measured to be 0.6 ± 0.1. The enhancement is stable and observed across all spectral peaks. The peak definition is strong by comparison to R6G on glass.

The weak contrast observed here fails to support the conventional wisdom presented in the literature. The gap mode configuration that occurs when the enhancing tip is held above a gold sample should produce increased enhancement factors. This is due to the effective oscillating dipole being mirrored in the substrate reinforcing the field across the probed molecules.

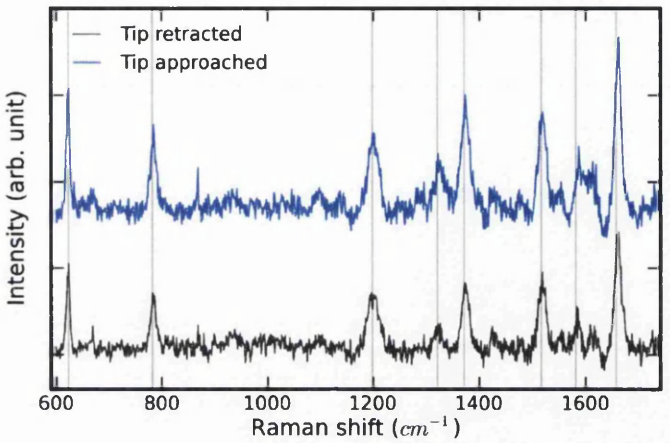

Figure 7.6: Gap mode TERS spectra of Rhodamine 6G on a gold coated glass substrate using tip $R\_Au.1$. Spectra were recorded with an acquisition time of 2 s at 0.5% ($\sim 30\mu W$) using 532 nm illumination and have been background corrected. The dominant Raman peaks are marked which lie at: $614, 776, 1186, 1310, 1365, 1510, 1579$ and $1652cm^{-1}$.

It is therefore disappointing that smaller contrasts are observed on this sample. This is compounded by the fact that this sample consists of a thinner film of Rhodamine molecules this produces a smaller far-field background contribution and should again lead to an increased TERS contrast.

We suggest that the reasons for this outcome can be pinned on two probable causes. Tip apex variation may have resulted in measurements with a highly enhancing tip on the R6G on glass sample whilst a tip with an equivalent magnitude of enhancement was not experienced on the R6G on gold sample. Secondly the gap-mode TERS system works only when the tip is within sufficient proximity to the gold surface. The evanescent field produced by the tip decays exponentially and so the proximity will determine whether sufficient energy is available for the surface electrons in the gold film to establish a complimentary dipole oscillation. In the literature a proximity of 5nm is quoted as a requirement to achieve efficient excitation of the mirrored dipole, near-field signal decays rapidly at larger separations [Pettinger et al., 2009], enhanced signals (non gap-mode) will begin to emerge at $\sim 20nm$ separation from the sample [Neacsu et al., 2007]. Shear-force

feedback will hold the tip below 15 nm separation from the surface however the exact separation for the set points we use is not known, because of this the advantage presented by the gap-mode configuration may not be being realised. Techniques that utilise AFM or STM based feedback systems can confidently position tips close enough to the surface to obtain the full gap mode advantage.

7.2.6 Temporal variation

Data is plotted in Figure 7.7 for a second enhancing tip, tip *R_Au.2*, showing enhancements of Rhodamine on gold. The first three peaks (623, 782 and 1198 cm^{-1}) have a mean contrast of 0.7 which shows the magnitude of the enhancement of the Rhodamine signal is similar to that of the previous dataset presented in Figure 7.6. The upper end of the spectrum however shows a far greater enhancement with a TERS contrast of 4.9, 6.8 and 1.6 for the 1371, 1581 and 1657 cm^{-1} peaks respectively. The contrast factors are presented for each of the Raman peaks in Table 7.3.

Table 7.3: Calculated contrast factors of the enhanced peaks from the TERS spectra plotted in Figure 7.7 using tip *R._Au.2*.

Peak [cm^{-1}]	623	782	1198	1321	1371	1516	1581	1657
TERS contrast	0.7	0.9	0.6	2.4	4.9	1.0	6.8	1.6

Signals of this nature are frequently observed and indicate that the tip is active producing one or more enhancing hotspots. It is however important that TERS spectra are stable and produce a signal that is representative of the sample. The enhanced line shape observed in this spectrum is representative of a temporally unstable enhancement. This can be seen in Figure 7.8a, the series shows a sequence of spectra taken directly after the measurement presented in 7.7 and utilising the same tip (tip *R_Au.2*). Measurements are taken with the tip in feedback on the sample. The spectra have been stacked to show the progression of the Raman response over time, background subtraction has been undertaken for clarity. The peaks at the higher end of the spectrum are transient, they can be seen to turn on and off over time and do not maintain a consistent peak position.

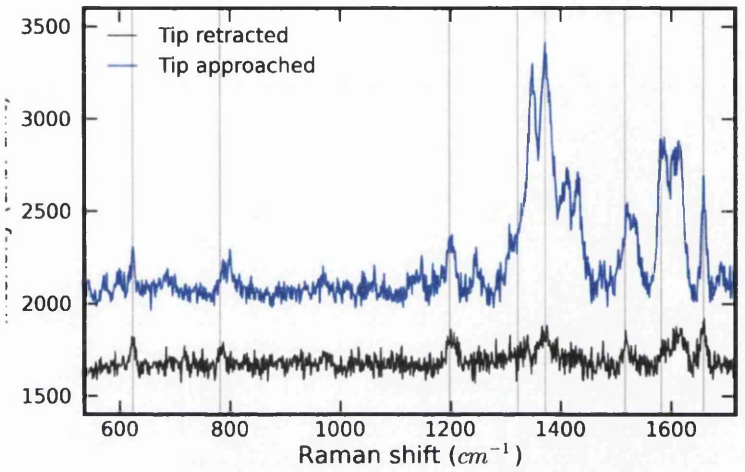

Figure 7.7: An active TERS tip (tip *R_Au.2*) showing enhancement of R6G on Au. This data shows the typical line shape for unstable, transient peaks which are highly enhanced and are located at the upper end of this spectral range. Spectra were recorded with an acquisition time of 10s and with 0.5% ($\sim 30\mu W$) laser power using 532 nm illumination. Background subtraction and offset have been applied for clarity.

The spectrum in Figure 7.8b shows the overall time averaged spectrum derived from the spectra presented in the time series (7.8a). The spectrum has not undergone background subtraction. The blue shaded area marks the 95% confidence band thus illustrating spectral regions that show high uncertainty. Below 1200 cm^{-1} the confidence band is narrow and so peaks at this end of the spectrum demonstrate little variation and can be considered real. At the upper end of the spectrum the confidence bands are wide indicating large uncertainty introduced by the transient peaks that are present in this spectral range.

7.2.7 Discussion of TERS temporal fluctuations

Temporal fluctuations in TERS spectra are not uncommon and have been presented and discussed in the literature. Table 7.4 lists prominent papers that discuss the origins of spectral instabilities in enhanced data. This discussion is primarily centred around single molecule TERS measurements where time

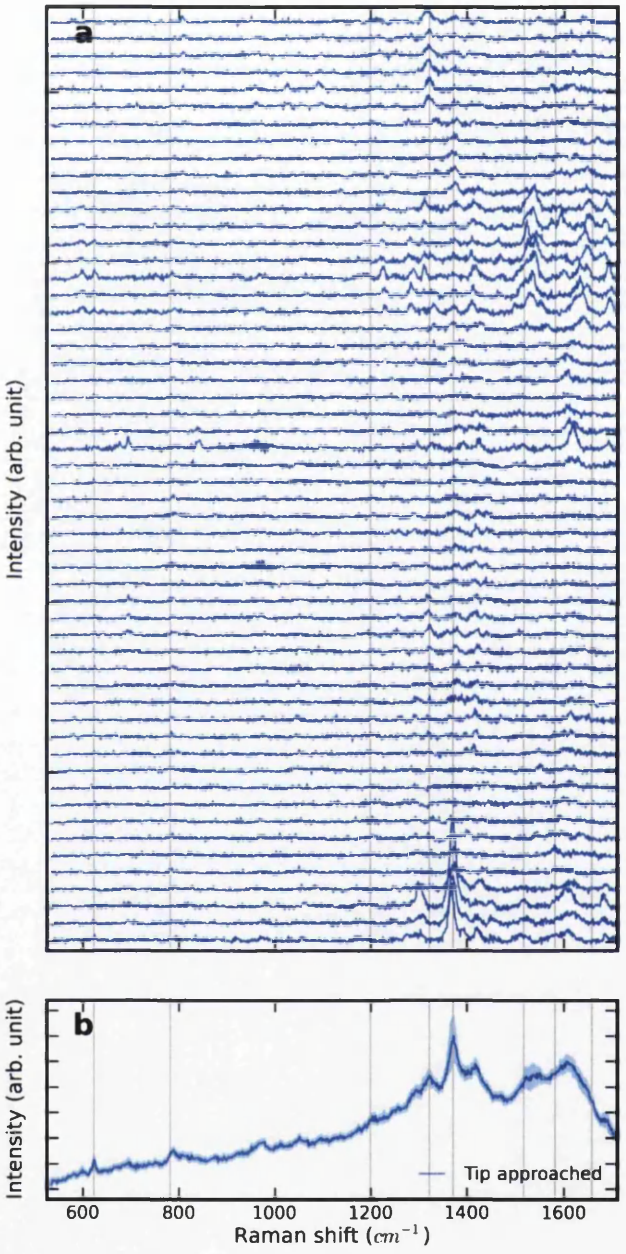

Figure 7.8: (a) Sequence of TERS spectra showing the time variation of the enhanced Raman signals of R6G on Au. Spectra are stacked with time progressing with increasing Y value. Each spectrum was acquired for 10s at 0.5% ($\sim 30\mu W$) laser power using the same tip and sample position as in fig 7.7, background correction has been performed. (b) The average TERS signal derived from the the datasets plotted in 7.8a. No background correction has been conducted, the shaded region depicts the 95% confidence band indicating the magnitude of the variance in the data.

varying spectra can show evidence for single molecule measurements, as such the bulk of the literature that discusses temporal variation is working on dye molecules.

Table 7.4: Publications that discuss temporal variations in enhanced spectra and which explain the possible mechanisms in action.

Publication	Sample	$\lambda[nm]$	Tip	Explanation given
[Domke et al., 2007]	MGITC ml	633	solid Au	Carbonaceous contaminants.
[Yeo et al., 2009]	sub-ml dyes	NA	NA	i. Molecular motion. ii. Phys. instabilities & Chem. changes of tip. iii. Carbonaceous contaminants.
[Ichimura et al., 2007]	Adenine	532	coat. Ag	Chemical and mechanical enhancements.
[Stadler et al., 2010]	BCB	633	solid Ag	Molecular diffusion.
[Pettinger et al., 2005]	MGITC sub ml	633	solid Au	Increased disorder in the SAM due to bleaching & photofragmentation.
[Hayazawa et al., 2005]	R6G	488	coated Ag	Charge transfer.

*ml = monolayer

The consensus drawn from the literature is that there are two types of temporal fluctuation. For samples with low molecular coverage temporal fluctuations in the peak intensities can occur due to the changing ensemble of molecules populating the enhanced near-field. This can change due to molecular diffusion or tip drift. Peak ratios may also be altered as a result of changing orientations of the molecules beneath the tip. The second cause is from carbonaceous contaminants that diffuse into the enhancement zone, this can be identified by new peaks being observed that are not consistent with the known Raman peaks of the molecules being probed.

In general it is no longer considered valid to explain the emergence of many new peaks as a result of altered selection rules that may occur due to the high field gradient beneath the tip. There have been no theoretical or experimental studies to show that this can unambiguously be the case. The TERS spectra should resemble the ensemble structure but may exhibit different and varying peak ratios [Domke et al., 2007]. Even in the case of photobleaching, experiments on MG and BCB have shown that the resulting decomposition products are spectroscopically silent and do not introduce new spectral signals [Yeo et al., 2009], bleaching can however be a source of carbon molecules leading to carbonaceous contamination signals. There are some cases where peaks not visible in the bulk far-field or SERS spectra do occur. Hayazawa et al. [2005] carried out a detailed study of R6G and proposed that charge transfer from the tip can promote enhanced activity of otherwise

silent vibrational modes when the correct conformational conditions are met beneath the tip.

Carbonaceous contaminants produce time varying spectra because they are able to rapidly create and break C-C and C-O bonds [Domke et al., 2007]. Carbon based molecules can originate from the sample; from contamination introduced to the tip in the fabrication process; and from the ambient conditions in the laboratory. The silver tip is readily oxidised, as already discussed, and will act as a catalyst for reactions which are more likely to occur at the tip apex due to the raised temperatures found in the enhanced field. Furthermore the Raman cross section of carbonaceous molecules is large and so few carbon based molecular structures need to diffuse into the enhanced field to be prominently detected.

To determine the exact origin of temporally fluctuating peaks the spectra can be time averaged. The resulting line shape indicates whether the peaks are derived from the sample, in which case the peak distribution will largely resemble that of the bulk sample, or from an external source such as carbon contaminants. Carbon contaminants can easily be identified since the time averaged spectra will resemble that of amorphous carbon with very broad peaks centred at 1350 and 1580 cm^{-1} [Blum et al., 2012].

Following this discussion it is clear that the data presented for tip *R_Au.2* in figures 7.7 and 7.8 show a convolution of stable, enhanced rhodamine peaks and large transient peaks that are present due to carbonaceous contaminants. The profile of the time averaged spectrum in Figure 7.8b resembles amorphous carbon with the broad peaks around 1350 and 1580 cm^{-1}, additionally the largest peak variation occurs in the vicinity of these carbon peaks as demonstrated by the increased width of the confidence bands. The scale of the confidence bands directly indicate the level of uncertainty in each peak and can thus be used to inform whether or not the peak can be considered a consistent, real peak that is representative of the tip-sample interaction.

This carbon signal is not present for all tips that have been studied and can, when present, be tuned out. Enhanced carbon signatures indicate that the tip is active and that further optimisation of the tip position in the beam is worth pursuing. It has been possible to alter the alignment of the tip

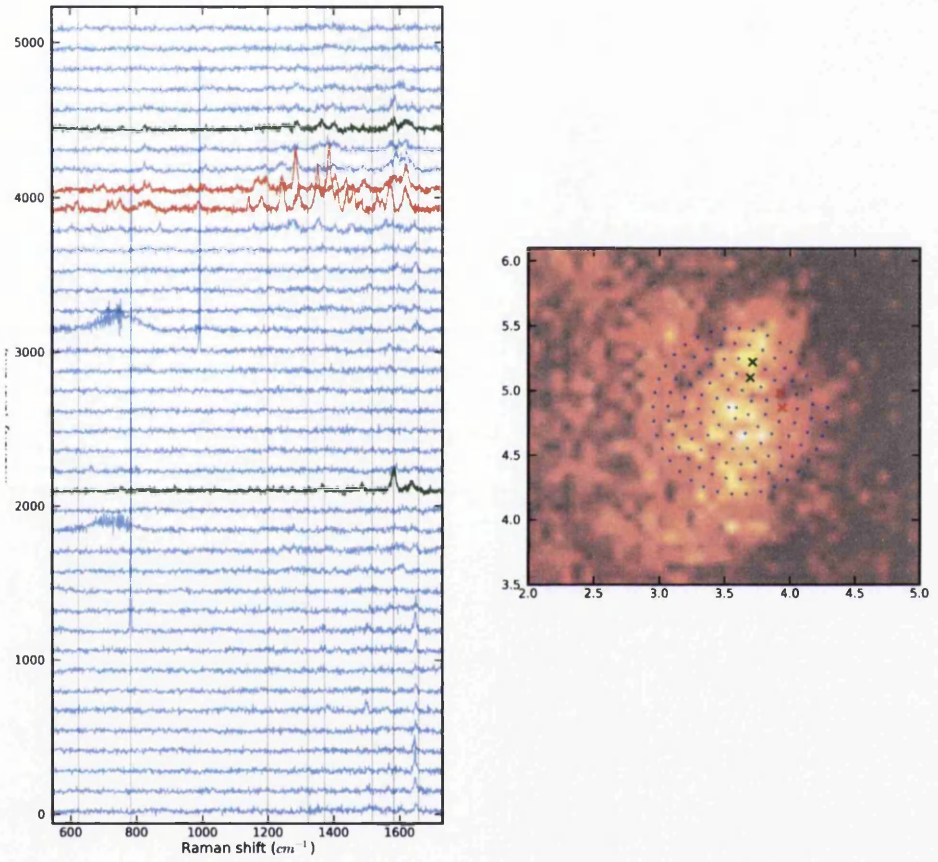

(a) Raman response **(b)** Alignment grid

Figure 7.9: a) TERS spectra for R6G on glass, measurements were taken across a grid of tip positions around the laser spot in order to identify TERS hotspot locations. Green and red data points indicate measurements of interest that are discussed in the text. Spectra were acquired for 15 s at 0.1% laser power ($\sim 10\mu W$). b) The TERS measurement grid superimposed on an image of the laser spot which was produced by scanning the tip and recording the scattering intensity with the APD.

and the measurement settings to obtain stable spectra that are no longer dominated by these contamination signals. The alignment grid shown in Figure 7.9 is a good example of this. The figure shows the TERS response as the tip is moved in feedback around the laser spot. TERS activity is emerging in two regions of the spot marked by the red and green data points. The green data points represent potentially promising enhanced spectra whereas the red points represent the enhanced spectra of carbon contaminants. The physical locations of these signals are spatially separated and so the red signals may be emerging from a secondary hotspot at the side of the tip. In this case altering the tip position is enough to remove the contamination signature. The contamination signal appeared, with respect to the sequential order of measurements, between the two promising data points (green) showing that the best reliable enhancement that this tip was able to produce on the rhodamine was independent of the enhanced carbon signatures.

7.3 TERS of a thiophenole SAM

In order to further the understanding of TERS and evaluate its successes and pitfalls a global round robin experiment is being conducted whereby measurements are being undertaken by multiple experimental groups on a standardised sample. This project has been designed and instigated by the TERS group from the chemistry department at ETH, Zurich. As participants in this programme it presents a prime opportunity to gain substantial knowledge about the performance of our system and place its sensitivity in relation to that of the more established TERS community.

The trial has been designed to be a blind test compromising of two stages. At the time of writing we have completed the first stage and so are yet to learn the full outcome of the project and have not seen the data produced by other groups. The first stage has been conducted on a self-assembled monolayer (SAM) of thiophenole that was pre-prepared by the Zurich group. We have witnessed them conducting TERS on an identical sample using their own upright TERS setup which features a solid silver probe mounted in STM configuration with 633 nm illumination. As a result we have good knowledge

of what to expect from the sample and what measurement parameters are required. The second stage will consist of an unknown sample which will significantly increase the challenge as there will be no known spectral peaks on which to focus any optimisation processes. This secondary stage and a full discussion of the global data will not be featured in this writing since it is yet to be completed.

The sample that is discussed in this section is a self assembled monolayer of thiophenole molecules on a gold coated glass coverslip. The sample was received in a wet state, sitting in a sealed container of the thiophenole solution. The only preparation required on our part was to rinse the sample in ethanol and dry under a nitrogen flow. This was conducted immediately before use to ensure the optimum state of the sample. Multiple experiments were carried out over the course of two days, although some sample degradation is expected within this time the sample remained active throughout the duration of the work.

Thiophenole is potentially an ideal standardisation sample as it forms a well defined system that is stable and resistant to laser illumination. The thiol molecules undergo self-assembly by binding directly to the gold substrate thus ensuring that only a single layer of molecules adheres to the surface. Excess molecules are removed in the rinse process. In this case this forms a uniform surface that is perfectly suited to TERS development. Understanding the distribution of thiols can however have important applications since thiols are often used to alter the surface chemistry of a metal surface allowing the stable and homogenous binding of biomolecules to create a functionalised material. Biosensors, for example, can be created by exploiting a monolayer of ligands. A ligand monolayer can be formed on top of the thiol molecules since the ligands will bind to the tail groups introduced by the thiol molecules [Homola et al., 1999].

With the 532 nm laser measurements were conducted utilising the illumination path I2 and the radial polariser positioned at RP3, see Figure 4.1 for details. 10% laser power was used for every measurement. This equates to $1.4mW$ at the sample, the sample produced an additional attenuation of $\sim 50\%$ leaving $0.7mW$ at the tip. The 785 nm measurements were conducted

using the same path (I2) however no radial polariser was used and so linearly polarised light was focused at the objective. 50% laser power was used for these measurements which produced $1.5mW$ at the sample. The magnitude of the attenuation through the sample was not measured for this wavelength.

7.3.1 Thiophenole TERS results

No signal is visible in the far-field with $532nm$ illumination since the thiophenole is not a resonant Raman scatterer and the single molecular layer results in a very small scattering volume. Any signal that becomes visible when the tip is approached is a direct result of near-field enhancement. The primary benefit, in this case, of using TERS is not the high resolution properties but the signal enhancement that produces sufficient signal for detection. Data is shown for three solid etched tips and one coated AFM tip. Additionally tip T.2 was illuminated with both $532nm$ and $785nm$ radiation. The peak positions marked by the grey vertical lines on the TERS plots are based upon the spectral positions reported by Schmid et al. [2009], the peak assignments for $532nm$ illumination are presented in Table 7.5.

Table 7.5: Thiophenole TERS peak assignment identified by Schmid et al. [2009] for 532 nm illumination:

Raman shift $[cm^{-1}]$	1000	1023	1073	1576
Assignment	op C-C-C str	op C-H str	ip C-C-C str & C-S str	C-C str

7.3.2 Tip T.1

The data for tip T.1 is presented in Figure 7.10 and shows the enhanced response of thiophenole in gap mode configuration. Repeat measurements are shown with parts 7.10a and 7.10b displaying 30 and 60 s acquisition times respectively. Tip out spectra, where taken, are shown in grey. Repeat measurements allow the identification of stable enhanced peaks. There is a large amount of transient activity around 1350 and 1600 cm^{-1}, which is similar to what has already been seen in the Rhodamine spectra, these peaks are best attributed to carbon derived signatures. These signatures are large by

comparison to the small peaks attributed to the thiophenole. The thiophenole peaks that are of interest are marked by grey vertical lines, a trio of peaks centred above 1000 cm^{-1} should be observed when the tip is in feedback.

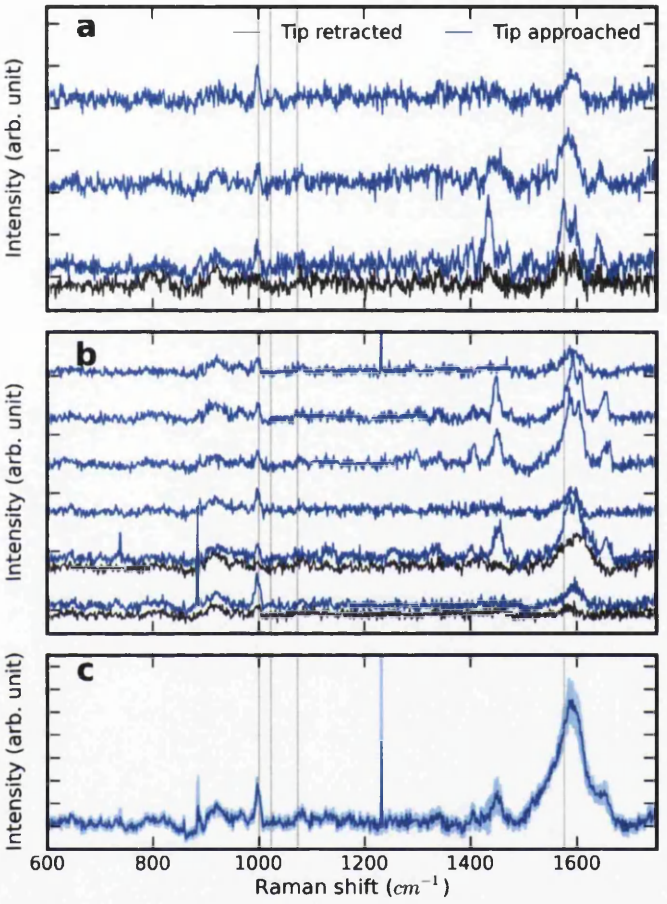

Figure 7.10: Tip T.1. Repeated TERS measurements on thiophenole at the same sample location. a) and b) show 30s and 60s acquisitions respectively at10% laser power ($\sim 0.7mW$). Background subtraction and offset have been applied for clarity. c) The average line shape of the data presented in 7.10a and 7.10b. The 95% confidence band is represented by the light blue shaded region.

Figure 7.10c shows the averaged spectrum for all the TERS data presented in parts 7.10a and 7.10b. The light blue shaded region shows the 95% confidence band which allows us to identify stable and time varying peaks.

The peak at $1000cm^{-1}$ appears prominently and has a normalised peak intensity of $13 \pm 1Cs^{-1}$. The peaks at 1023 and $1073cm^{-1}$ are not so readily observed. The averaged line shape shows a small peak at $1073cm^{-1}$, an inspection of the repeat measurements shows consistent presence of a peak at this position however its intensity is very close to the level of the noise. The confidence band around this trio of peaks is small and so the peaks that are emerging can be confidently assigned as real and representative of the tip-sample interaction. TERS contrast factors can not be calculated since there is no signal to use as a reference in the far-field background. There is no discernible peak at 1023 cm^{-1} however this is the weaker peak out of the thiophenole peaks in this spectral region, since the 1073 cm^{-1} peak is weak it is not unexpected that the 1023 cm^{-1} cannot be resolved. This is a result of insufficient near-field enhancement.

Thiophenole also exhibits a Raman peak at 1576 cm^{-1}. We do not observe this peak however we cannot say that it is not present since this peak lies in the spectral region dominated by fluctuating carbon signals. The 95% confidence band is large and so the uncertainty in the line profile is greater than the peak height expected for the 1576 cm^{-1} peak. As such it may be present but is masked by the transient carbon signals.

7.3.3 Tip T.2

532 nm illumination

Figures 7.11a and 7.11b show the TERS response from two sample locations, a collection time of 30s was used in both cases. An averaged spectrum of the data from parts 7.11a and 7.11b is shown in figure 7.11c. This tip demonstrates similar trends to tip $T.1$. There are temporally stable peaks around 1000 cm^{-1} and transient contamination peaks found most prevalently at higher wavenumbers. In this case Figure 7.11c shows a very clear amorphous carbon signature that is creating two broad peaks at 1350 and 1590 cm^{-1}. This is combined with greater time varying activity than seen with tip T.1.

The trio of thiol peaks are evident including hints of a peak at 1023 cm^{-1} which is weakly present in both the repeated spectra and in the averaged

spectrum. The peak at 1000 cm^{-1} is however weaker than with tip $T.1$, the normalised average intensity measures $10 \pm 1Cs^{-1}$. The confidence band is once again small in this spectral region which indicates these peaks are real.

785 nm illumination

Figure 7.11d shows enhanced spectra when the same tip is illuminated with linearly polarised 785 nm radiation. It appears that the Raman cross section of the thiophenole is improved at this wavelength since there is signal apparent in the far-field spectra. With the tip in feedback there is a strong contrast on the $1000cm^{-1}$ peak however only weak contrast on the remaining thiophenole peaks. The mean contrast for the 1000 cm^{-1} peak for both sets of TERS spectra is 1.2 ± 0.3. Uncertainties are calculated based on the magnitude of the noise. The mean contrast of the 1073 cm^{-1} peak is lower at 0.3 ± 0.4. The enhancement of this 1073 cm^{-1} peak cannot be absolutely confirmed due to the size of the errors which result from the large noise and poor sample size. The lack of repeat measurements prevents any statistical methods that could demonstrate that the peak is real.

The observation that the contrast is not consistent across each of the thiol peaks is strange and leads to speculation that the enhanced signature may be originating from other sources. Some confidence can however be gained from the fact that the signal was repeatable across two separate measurements. This points to it either being the result of an enhanced thiophenole signal or that it is evidence of tip contamination. This tip had seen a reasonable amount of use already and imaging performance was poor due to heating effects from the 785 nm illumination so direct contamination of the tip cannot be entirely ruled out.

A slight shoulder is visible on the $1576cm^{-1}$ peak however additional datasets are required to ensure this is a real peak and not an artefact of other carbon signatures present in this spectral region. The presence of 3 out of the 4 peaks suggests that there is a strong case for pursuing further measurements with the 785 nm laser. It is exciting to think that this may open up increased sensitivity on certain samples which is demonstrated here by the increased

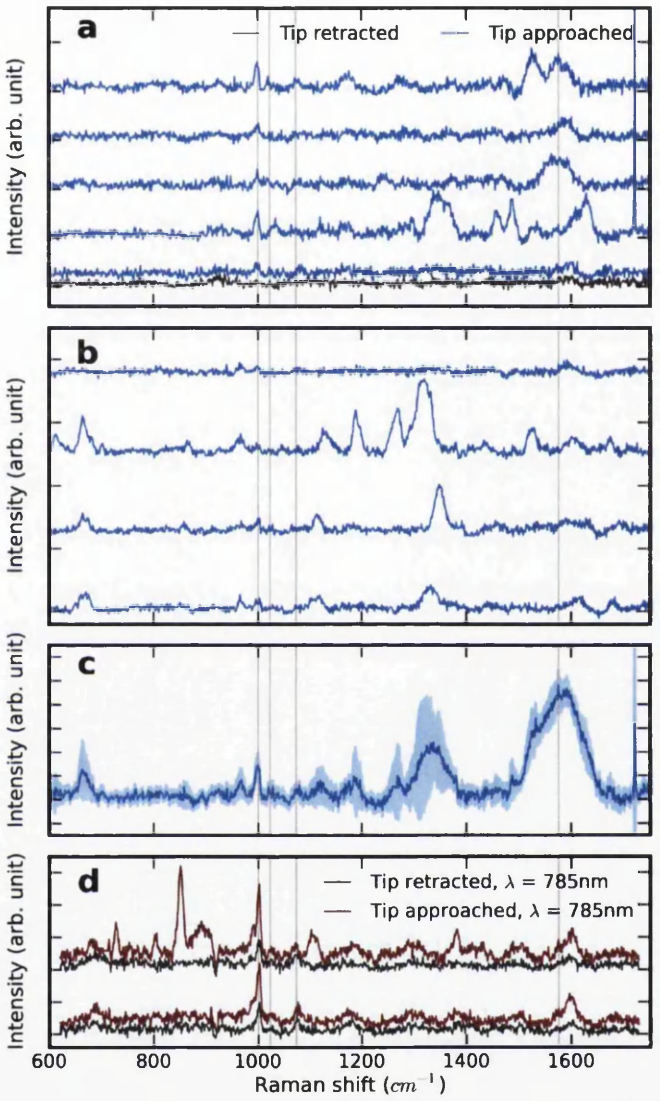

Figure 7.11: Tip T.2. Repeated TERS measurements on thiophenole collecting for 30s at 10% laser power. a) and b) show the response from two different sample locations. Background subtraction and offset have been applied for clarity. c) The average line shape of the data presented in 7.11a and 7.11b. The 95% confidence band is represented by the light blue shaded region. d) TERS measurements using the same tip with linearly polarised 785 nm illumination. Spectra were acquired over 10s with 50% laser power ($\sim 1.5mW$).

signal intensity in both the far and near-field. Further studies with increased sample sizes are however required before any firm conclusions can be drawn.

7.3.4 Tip T.3

Tip T.3 shown in Figure 7.12 represents a plasmonically active tip that is not producing a repeatable TERS enhancement of the sample structures. This suggests that the hotspot is not located at the apex and the time varying peaks observed in the spectra are a result of contamination occurring at the displaced hotspot. The data demonstrates the presence of a peak at 921 cm^{-1} which would imply that this peak, which is present with other tips, does not originate from TERS enhancement of the thiophenole. In the third spectrum a peak at $1023cm^{-1}$ is present. This can not be considered real since it is only present in one of the four spectra and highlights the danger of searching for specific peaks amongst temporally fluctuating data.

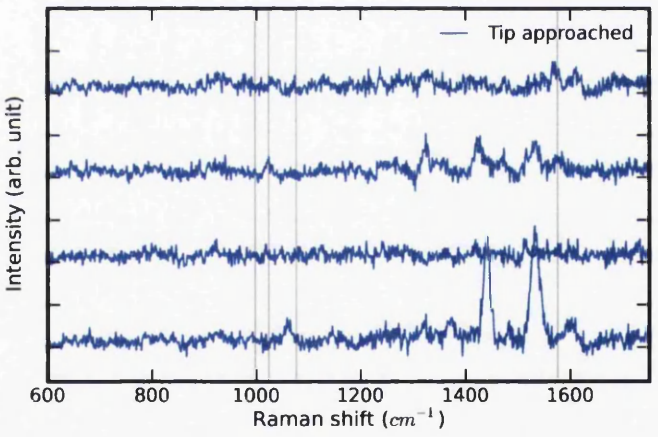

Figure 7.12: Tip T.3. Repeated TERS measurements showing an plasmonically active tip that does not produce a near-field enhancement of the thiophenole signal. Spectra were recorded for 10s at 10% laser power ($\sim 0.7mW$) and have been background corrected.

7.3.5 Tip T.4

Figure 7.13a shows that enhanced activity can occur without the presence of the sample demonstrating that enhanced Raman signatures can originate from local molecules in the vicinity of an active hotspot. This data was taken with a fresh tip that had not approached a sample. No sample was in place and so the signals derived here originate from solely the optical interaction of the metal tip in the laser focus. Figure 7.13b shows the averaged profile of the spectral series shown in part a, the 95% confidence bands are represented by the shaded region. The level of uncertainty is again far greater at the upper end of the spectrum and the activity peaks at 1600 cm^{-1} indicating the presence of carbon based structures. This highlights the fact that the enhanced response is highly sensitive to carbon contaminants that are either left on the surface of the tip from the fabrication process or are found in the local ambient environment of the hotspot.

7.3.6 Silver coated AFM tip

TERS was attempted with a silver coated AFM tip. The SiNi tip was coated with 20 nm of silver using PVD. An SEM of the tip surface can be seen in Figure 4.13. The TERS spectra are shown in Figure 7.14. The tip is demonstrating plasmonic activity since the signal changes when the tip is approached and there are transient peaks that indicate an active hotspot within the laser focus. There is however no signal that can be reliably attributed to thiol molecules. This is both the case for the short 30 s acquisitions and the longer 120 s acquisitions.

7.3.7 Discussion of TERS on thiophenole

The thiophenole data presents some important conclusions for TERS experiments involving small Raman signals. The conclusions drawn can be made confidently thanks to the sample which has been carefully designed by the Zurich group to produce a consistent and reliable TERS response. The thiophenole samples are produced in batches and a member of the batch was

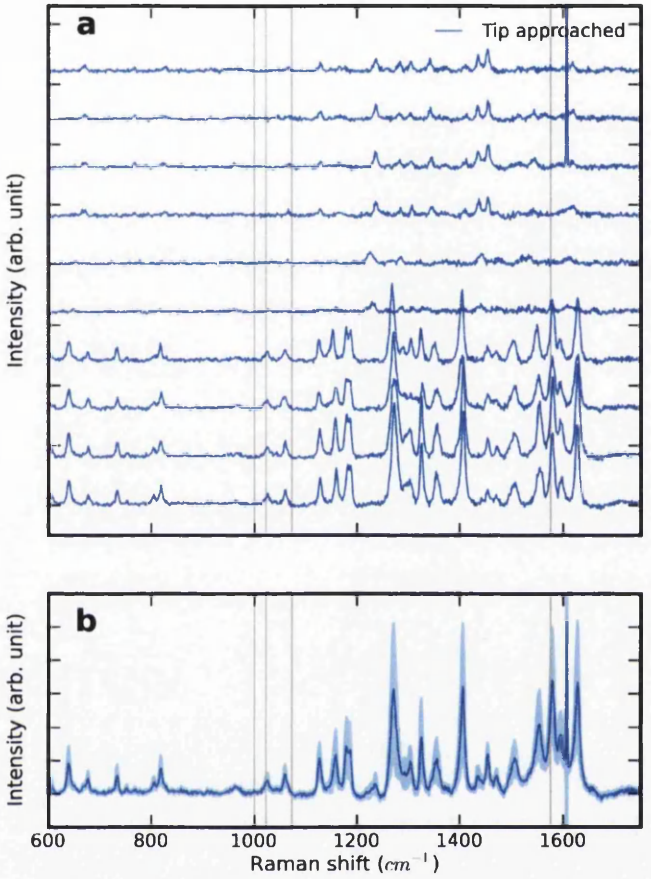

Figure 7.13: Tip T.4. a) Repeated spectra taken of a fresh etched tip positioned in the centre of the laser focus with no sample present. Spectra were collected for 10s at 5% laser power ($\sim 0.7mW$) and have been background corrected. b) The averaged line shape of the spectra presented in 7.13a, the light blue shaded region indicates the 95% confidence band.

characterised on the Zurich TERS system to ensure that the samples being sent out, and that we have been fortunate enough to use in this study, are active and of sufficient quality.

Our system clearly has some issues with contamination signals which become particularly noticeable when searching for small signals. Despite this we have been able to use multiple tips and multiple measurements to isolate the signal deriving from the tip-sample interaction from the more

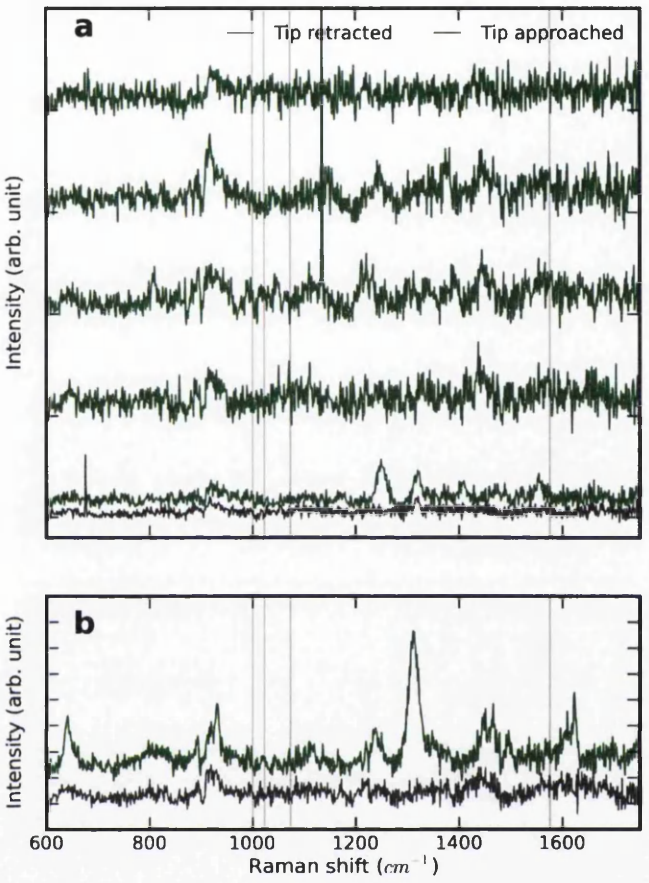

Figure 7.14: Repeated TERS spectra taken using a Ag coated AFM tip, no enhancement is observed of the thiophenole peaks. a) 30s acquisition at 10% laser power b) 120s acquisition at 10% laser power. Background subtraction has been performed for both data-sets.

intense contamination signals that are present. The time varying nature of the carbon signals is highly helpful in their isolation. By statistically analysing repeated measurements the standard deviation that is effectively represented by the confidence bands allows easy identification of fluctuating peaks. This would not be possible if only one long acquisition was taken as the temporal information is lost.

We found that it was possible to identify the two more intense Raman peaks that are present around 1000 cm^{-1} prior to knowing the peak locations. Since we did not have a bulk sample we did not know the exact thiophenole Raman

peaks that we expect to see with our system. Following an inspection of the data, peaks were selected that appear repeatable across each of the enhancing tips that have been studied and that also demonstrated repeatability across multiple measurements illustrated by a narrow confidence band at the peak. These peak positions were allocated before referring to the literature and so are considered to be a blind assignment. This is important since the transient peaks make it possible to identify spectra that match the required activity and can thus lead to biased data selection which could lead to the identification of spectra that are not representative of a true stable enhanced signal from the sample. Transient peaks can be identified by a wide confidence band in the spectral region of interest; the confidence band indicates the level of variation between repeated spectra.

The peaks identified as consistent between active tips and repeated measurements were located at 921, 964, 997 and 1076 cm^{-1}. From this list of peaks we determined that only the peak at 997 and 1076 cm^{-1} can be confidently assigned to near-field enhancement of the thiophenole molecules. The peak at 921 cm^{-1} is observed in the far-field and exhibits little enhancement and so is thought to originate from the bulk properties of the sample. The peak at 964 cm^{-1} is present when no sample is in place and only the tip is positioned in the focus and as such this peak does not originate from near-field enhancement of the thiophenole molecules.

The literature was subsequently referred to and the expected peak positions were found as presented in Table 7.5. From this we can see that the two peaks we identified, albeit with slight shifts, are present in the literature. There are two further peaks at 1023 and 1576 cm^{-1} that we were unable to identify in our data. The 1023 cm^{-1} peak was not identified because it is the weaker of the 3 peaks around 1000 cm^{-1} and the enhancements that have been recorded provide very weak signal that do not show a clear and statistically significant peak at this location across the repeat measurements, some spectra do however show subtle evidence of this peak. The $1576cm^{-1}$ peak lies in the upper spectral range where large transient peaks mask the activity at this wavenumber.

These results are reinforced by the enhanced signals that were recorded by

tips T.3 and T.4 which show enhanced contamination signals however tip T.3 showed no thiol signal when on the surface and tip T.4 was demonstrating temporal fluctuations without the sample in place. The signals produced by these tips did not show evidence of a thiophenole signal and demonstrate similar trends in enhanced contaminant activity with fluctuating signals that are most prevalent at higher wave numbers around 1350 and 1580 cm^{-1} which are the positions where amorphous carbon can be seen to be most active.

The work on thiophenole films was experimentally the last work to be conducted for this thesis and so represents the most optimised configuration of the system and procedure. Out of the 4 etched tips used for TERS measurements on this sample two showed enhancement of the thiophenole signature (tips T.1 and T.2), one showed signs of plasmonic activity through enhanced contaminant peaks but no enhancement of the thiophenole peaks (tip T.3). The final tip, for which no data has been presented here, showed no enhancement of the thiophenole signal and no signs of activity in the form of any unrelated or temporally unstable peaks when the tip was in feedback. Microscope images for these 4 tips are presented in Figure 7.15. These images show that the etches are fairly consistent across each of the tips and on the microscopic scale there are no obvious differences that might have allowed us to determine which of these tips would be active or inactive. A 50% success rate is however fairly acceptable especially considering the weak response of this sample which requires a reasonably large enhancement for the peaks to be observed.

7.4 Summary

TERS enhancements have been realised on ultra-thin rhodamine films, rhodamine monolayers on gold and on thiophenole monolayers. The enhancements are relatively small which indicates that there are still efficiency gains to be made in the instrument however the specific properties and geometries of the tips used in this study may also be a factor. Carbon contamination is present for some tips however this does not prevent the isolation of the enhanced signal that originates from the sample. Contaminant signals have been observed to

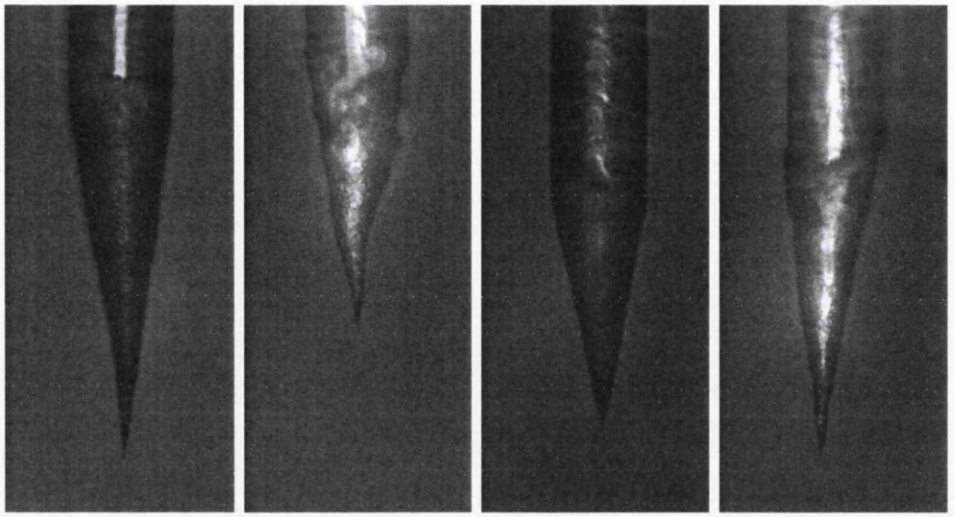

(a) Tip T.1, Enhancing **(b)** Tip T.2, Enhancing **(c)** Tip T.3, Active/Non-Enhancing **(d)** Non Active

Figure 7.15: Microscope images of the four etched tips used for TERS measurements in the thiophenole experiment. a) and b) show tips T.1 and T.2 which produced enhancements of the thiol peaks. c) Show tip T.3 which showed signs of plasmonic activity but no enhancement of the thiophenole peaks. d) shows a non active tip that did not display TERS enhancement of the thiophenole peaks or other signs of plasmonic activity when approached to the surface.

not be temporally stable and so can be isolated by analysing the variance over multiple short acquisitions. Other experimental configurations were trialled which include the use of coated AFM probes and 785 nm illumination wavelength. Enhanced activity was observed with the AFM probes however there was no signal that could be directly attributed to the thiophenole. Randomly fluctuating peaks indicate that some enhanced effects were occurring and so the trial of further coated AFM tips is recommended. The 785 nm laser demonstrated some promise however the limited data set does not allow us to incontestably attribute the observed enhancements to thiophenole and some questions are raised by inconsistent contrast factors across the thiophenole peaks, it does however show promise and this wavelength should be considered for further work.

Chapter 8

TERS on Graphene

8.1 Selective enhancement of lattice defects

Understanding the role of defects in graphene is key to tailoring its properties and promoting the development of graphene-based devices. This chapter presents TERS data that shows preferential enhancement of the D band on multilayered graphene and on ultra-thin graphitic films. Heightened defect sensitivity has been demonstrated on certain defect types on both variants of the material. These observations are discussed with reference to theory and other experimental publications; the discussion draws upon the detailed understanding of the physical properties of the material that was developed in Chapter 2.

Graphene is a remarkable material that has shown great potential in the field of nano-electronic gigahertz [Lin et al., 2009] and terahertz devices [Chen et al., 2012]. Current developments in graphene indicate that its intrinsic properties could secure a road map to future disruptive technologies and innovation [Geim and Novoselov, 2007]. In graphene, defects play an important role in manipulating the properties of the material, enabling a wider range of promising applications.[Banhart et al., 2011] Crystallographic defects occur when the hexagonal symmetry of the crystal lattice is broken, such as at topological point defects [Hashimoto et al., 2004] and at edge boundaries [Casiraghi et al., 2009].

By their nature defects have the potential to scatter electrons and so influence the conduction properties of the material [Chae et al., 2012]. For example, defect dominated structures such as nano-ribbons can be tuned to be either metallic or semiconducting [Terrones et al., 2010]. The presence of defects, of the correct type and geometry, can dramatically increase the local surface reactivity of the material [Zhang et al., 2009]. Moreover point defects can introduce spin-1/2 magnetic moments that can generate paramagnetism within graphene [Nair et al., 2012]. To maximise the potential of graphene, tools must be adapted and developed to quantify and characterise the distribution of defects on the nanoscale.

Raman spectroscopy, which looks at the inelastic scattering of light to measure the vibrational modes in a sample, has been one of the principle characterisation tools of graphene from the outset. It provides a rapid and robust method for identifying single layer graphene due to clear changes in spectral response between graphene and graphite [Malard et al., 2009, Pimenta et al., 2007]. Whilst Raman can also determine the quality of the graphene, it is diffraction limited. Hence the key signatures measured come from an ensemble average of features present and so contributions from small structures are often undetectable.

TERS can combine the chemical sensitivity of Raman with the spatial resolution of a scanning probe microscope. Much TERS work has been carried out on carbon nanotubes where sensitivity to defects on length scales of 10's of nm is well documented [Georgi and Hartschuh, 2010]. There is a limited scope to TERS publications on graphene [Pettinger, 2009, Saito et al., 2009, Snitka et al., 2011, Stadler et al., 2011a, Wang et al., 2012] and few studies have targeted their attention towards defects. Stadler et al demonstrated high resolution mapping of defects and CH stretching modes with $< 12nm$ resolution on CVD and exfoliated graphene. Their studies utilised a gap-mode TERS configuration which further enhances the graphene response but requires preparation on an appropriate metallic substrate [Stadler et al., 2011a].

This chapter investigates the sensitivity of TERS to isolated defects on graphene and ultrathin graphite flakes. We present the strong D-peak

enhancements that can be derived from the TERS signal and discuss the optical response as a function of illumination volume and sample dimensions. The chapter examines the TERS response on multilayer graphene to a range of physical structures including, edges, overlap regions and wrinkled creases. We analyse the results in context with the theoretical predictions of Raman signatures that arise due to defects and highlight the distinct advantages that the TERS technique possesses in achieving a localised response on defects.

8.2 Preparation of graphene

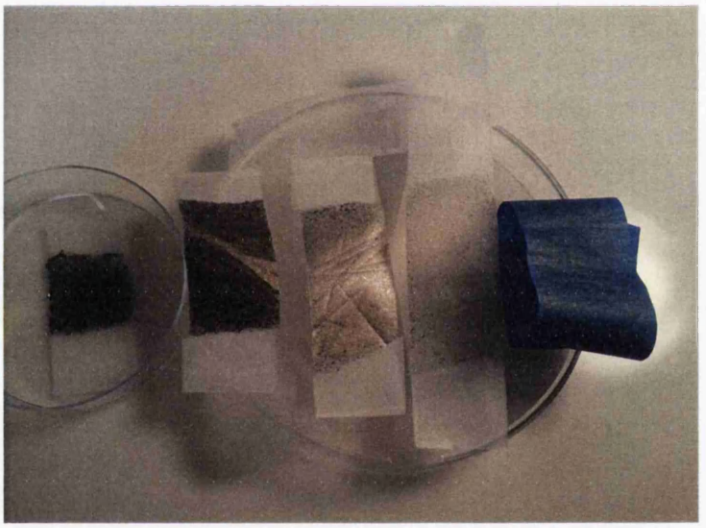

Figure 8.1: Exfoliatiated graphene preparation using the scotch tape method. Graphitic material is exfoliated from HOPG producing thick graphitic material (left). Multiple pieces of scotch tape are used to thin the graphitic flakes before transfer to a substrate using low tack masking tape (right).

Samples were prepared using the scotch tape method Novoselov et al. [2005], scotch tape is used to exfoliate HOPG and pull apart the weakly held graphitic planes. In practice we found that this required multiple pieces of tape. The tape is applied to the HOPG and removed peeling off a thick layer of graphite in the process. The tape is then folded on itself and pulled apart to transfer the graphitic flakes around the tape. Once even coverage has been

achieved over an area the size of the coverslip a fresh piece of tape is applied to the first piece of tape in order to further thin the graphitic flakes. This process is repeated 4 or 5 times with a fresh piece of tape at each stage. The resulting pieces of tape can be seen in Figure 8.1 which shows the extent of the coverage on each piece of tap and the reduced thickness of the graphite flakes as each new piece is introduced. The final piece of tape has a light grey covering of graphite. Finally the thinned graphite flakes were transferred onto a piece of low tack masking tape, this tape is used to transfer the graphene flakes onto a coverslip since it leaves less glue residue.

The flakes are transferred by pressing the tape onto the surface of the glass coverslip. Flakes adhere to the glass and are pulled off in the process. Glue residue is a problem, two methods were produced to overcome this. The first was using multiple applications of the masking tape. This had the tendency to initially deposit glue residue and then the subsequent applications pulled the glue that had previously been deposited back off the coverslip. The second method was to conduct a solvent wash and to dry under nitrogen. This was used when the first method was unsuccessful however it was generally avoided as the wash process often left its own residues behind.

An example of flakes deposited on the surface is shown in Figure 8.2. The flake marked by the green box is multilayered graphene and has been used for TERS measurements which are discussed in Section 8.5 of this chapter. The primary challenge that was faced was how to isolate suitably thin material. The limitations of the experimental setup restrict the sample to transparent substrates and so the Si/SiO_2 substrates that are typically used in graphene research to allow straightforward identification of single and few layer material could not be used. The optical contrast of thin material viewed in the white light image is small. A combination of the white light image, far-field Raman mapping and AFM was used to identify suitable flakes. It was found that the most favourable places to look were the torn edges of thicker flakes that often feature thin layers at their extremities.

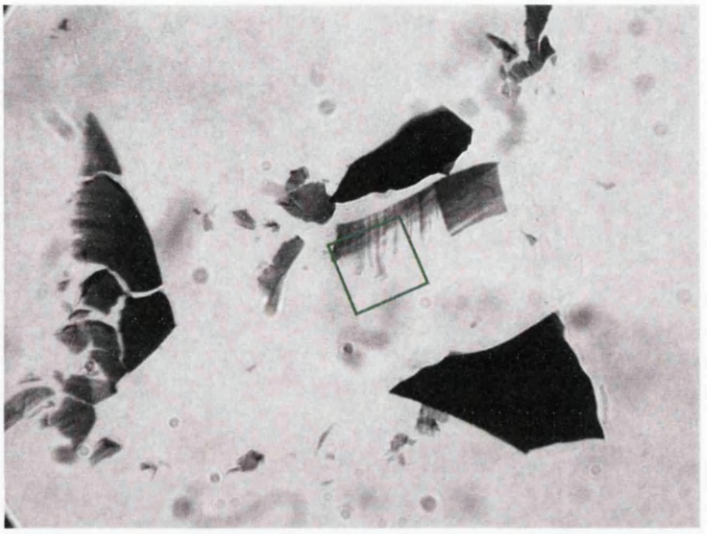

Figure 8.2: Microscope image of exfoliated graphitic flakes of various thicknesses on a glass coverslip. The region marked by the green square contains multilayer graphene flakes. These flakes are used in TERS measurements in Section 8.5

8.3 Experimental Configuration

Optical alignment of the tip to the laser focus was achieved by scanning the tip through the laser spot and recording the reflection intensity on an avalanche photodiode. TERS line measurements were recorded with spectra taken both whilst the tip was in-feedback (approached) and out-of-feedback (retracted) at multiple positions along the line. If background subtraction was applied to the spectra it was performed using a rolling-circle filter [Brandt et al., 2006]. All spectra were taken with 532 nm radially polarised laser illumination. Graphite measurements were conducted with a 63x, 0.9 NA objective and 1.4 mW laser power at the sample. Graphene measurements utilised a 100x, 1.25 NA oil-immersion objective with $200\mu W$ at the sample.

8.4 TERS on HOPG

Figure 8.3 illustrates an example of the TERS response from the edge of an ultra-thin HOPG flake. The enhanced spectral response is shown (tip

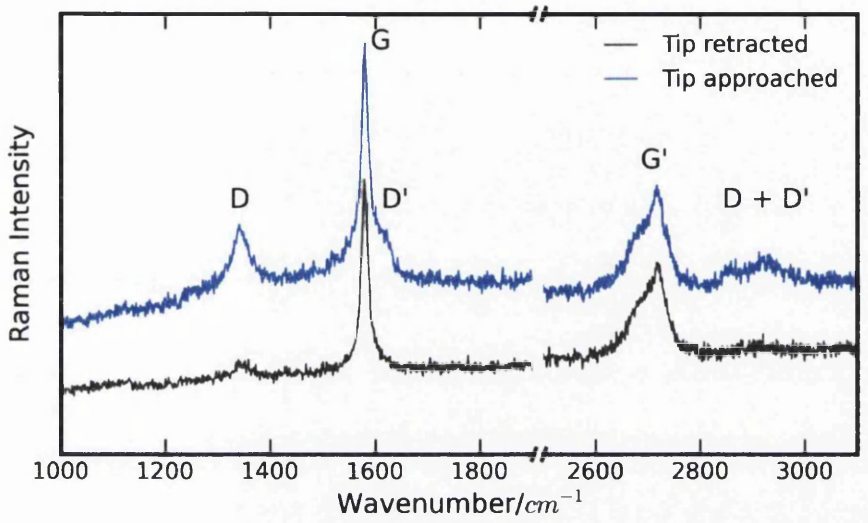

Figure 8.3: A TERS measurement with tip located at the edge boundary of an ultrathin HOPG flake ($\sim 25nm$ in thickness). The main Raman modes of Graphite are labeled. Spectra were acquired using a 200 s acquisition time.

approached) alongside the far-field Raman response (tip-retracted). The Raman spectra of graphite and graphene can share four main peaks D, G, D' and G' at, $1350cm^{-1}$, $1600cm^{-1}$, $1620cm^{-1}$ and $2700cm^{-1}$ respectively and these can be clearly observed from the HOPG flake, in particular the enhanced peaks related to defective lattice sites.

The G band is present in all carbon spectra and is a first order process attributed to the stretching of the C-C bond. The G' peak is a second order double resonance process whose lineshape indicates the number of graphene layers in the sample [Ferrari et al., 2006, Stadler et al., 2011a]. Multilayers of graphene that exceed 10 layers possess a G' peak whose shape resembles that of HOPG, as shown in Figure 8.3.

The defect induced D band occurs due to a double resonance process that requires elastic scattering from a defect and inelastic scattering by a phonon. It is attributed to the ring breathing modes of sp^2 rings and is activated only where structural disorder is present in the lattice, such as at edge boundaries or lattice faults. Whilst the D band is an intervalley

process, the D' peak is an intravalley double resonant process which also occurs due to defects. A combination mode of D + D' is also observed at higher wavenumber, $\sim 2900cm^{-1}$.

The intensity ratio of I_D/I_G is often used to quantify defect concentrations [Jorio et al., 2010] and domain size [Ryu et al., 2011]. The intensity of the D band is however dependent on edge type, such as whether it takes a zigzag or armchair conformation, and also the incident polarisation [Jia et al., 2011]. D band intensity is maximised when the polarisation is aligned parallel to the edge.

TERS enhancement can be observed in Figure 8.3 but the response is not uniform across all peaks. Strong enhancement is observed in the D, D' and D+D' peaks, with an increased contrast in the D band of ~ 4. Contrast is a measure of the ratio between the near field intensity and the far-field intensity of a particular peak. The contrast associated with the D' and D+D' peaks is significant but not assigned, since there is no resolvable signal in the far-field. Both these peaks become prominent when the tip is approached, with the D' peak rising to 16% of the height of the G peak. Very slight enhancement is observed in the G and G' bands with an average contrast factor of ~ 0.08 in the bands.

Figure 8.4a presents an AFM image of a HOPG flake which consists of a folded sheet with a number of flat planes and creases. An edge boundary was selected for detailed study which can be seen in Figure 8.4a and 8.4b. TERS point spectra measurements were conducted across the edge boundary at 200 nm intervals, as indicated by the green line on Figure 8.4b.

A cross-sectional line-profile across the flake edge is shown in Figure 8.4c and indicates that the flake is $\sim 25nm$ thick. Graphene has an interlayer stacking height of $0.335nm$ [Obraztsova et al., 2008, Pimenta et al., 2007], hence the HOPG flake contains around 70 graphene monolayers. The cross section shows the edge is not abrupt but tapers off gradually over a lateral distance of $\sim 1\mu m$. As a result it exposes a large number of individual, layer, lattice terminations producing a broad spatial area expressing defect activity. The spectral series in Figure 8.4d shows the development of the D band as the tip moves over and across the edge. The TERS enhancement is most

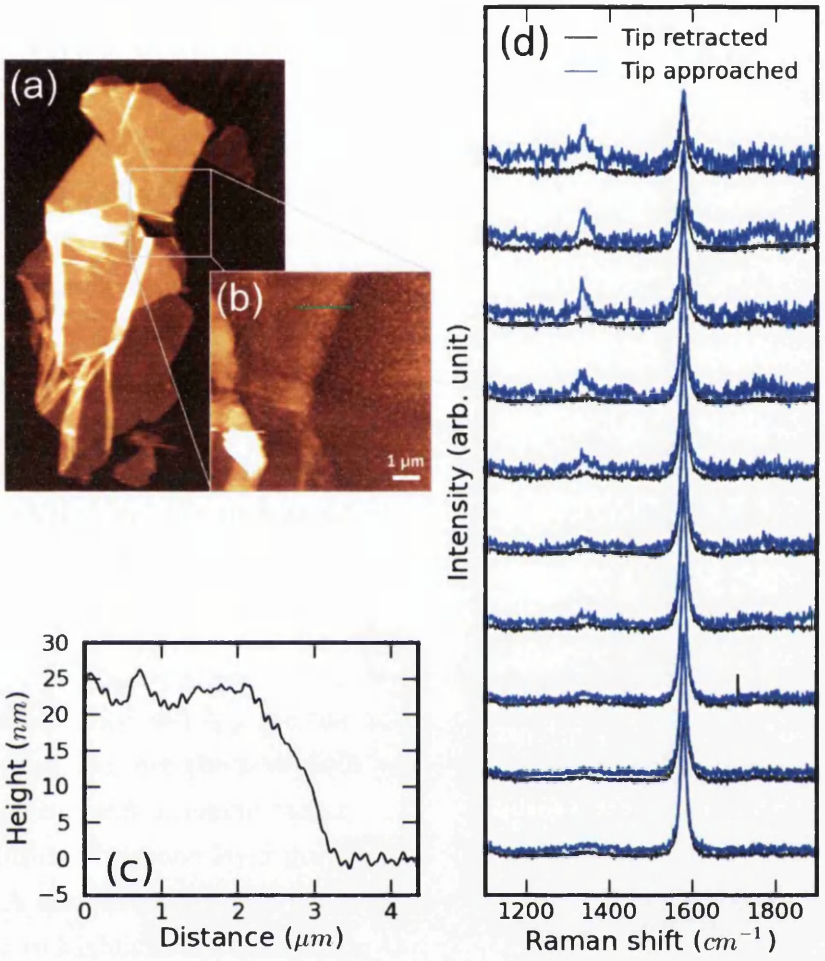

Figure 8.4: (a) Contact mode AFM image of Graphite flake. (b) Shear-force image of measurement region using TERS tip. Position of TERS measurement line is marked in green. (c) Cross-section through flake edge shows the flake profile at the measurement location. (d) TERS spectra acquired at $200nm$ intervals along measurement line. The series extends from the interior of the flake (bottom spectra) out across the edge boundary up until the furthest extent of the edge (top spectra). Spectra were acquired for 30s and have been background corrected.

prominent for the D peak derived from the edge of the flake, with a mean contrast of 3.41, whilst the G band from the same region shows a mean contrast of 0.035. The absolute peak heights have been plotted in Figure 8.5a.

A clear switching-on of the D band TERS response can be seen when the tip reaches the tapered edge region at the 1000 nm position, whilst the G band signal decreases as the layer thickness decreases.

The discontinuity in TERS response for the D band demonstrates that there are 2 distinct regions of the sample; we define region (I) as the flat, non-defective graphite surface and region (II) as the tapered edge of the flake which reveals a defect response.

The overall enhancement factor is dependent on the relative illumination volume in the near-field and far-field regimes. This allows the variations in TERS contrast to be accounted for by considering the specific volumes determining the signal and thus can explain the increase in TERS contrast for localised features such as defects on 2D graphene [Maximiano et al., 2012]. The relationship between intensity and volume is presented in equation 8.1

$$\frac{I_{NF}}{I_{FF}} = \gamma \frac{V_{NF}}{V_{FF}} \tag{8.1}$$

Where I_{NF} and I_{FF} are the near-field and far-field intensities respectively, V_{NF} and V_{FF} are the near-field and far-field volumes respectively and γ is the overall enhancement factor.

Unlike for mono-layer graphene the graphite flake must be considered in 3D. A simple model was constructed based upon illumination volumes in order to highlight the underlying trends in the optical response. To calculate the enhancement factor, region (I) has been modelled as a flat $25nm$ thick layer. Region (II) is modelled by a wedge with constant gradient descending from $25nm$ to $0nm$ over $1\mu m$.

For the G peak the far-field signal will originate from the full volume illuminated by the laser, the far-field volume was approximated by a cylinder with diameter equal to the spot diameter ($300nm$) and height equivalent to the thickness derived from the model. The near-field volume was considered as a hemisphere with a radius of $10nm$, the reduction in optical volume when the flake height < tip radius was accounted for. This definition of the optical volumes apply for both regions (I) and (II) for the G band.

The D band has a different dependence. We ignore region (I) since we

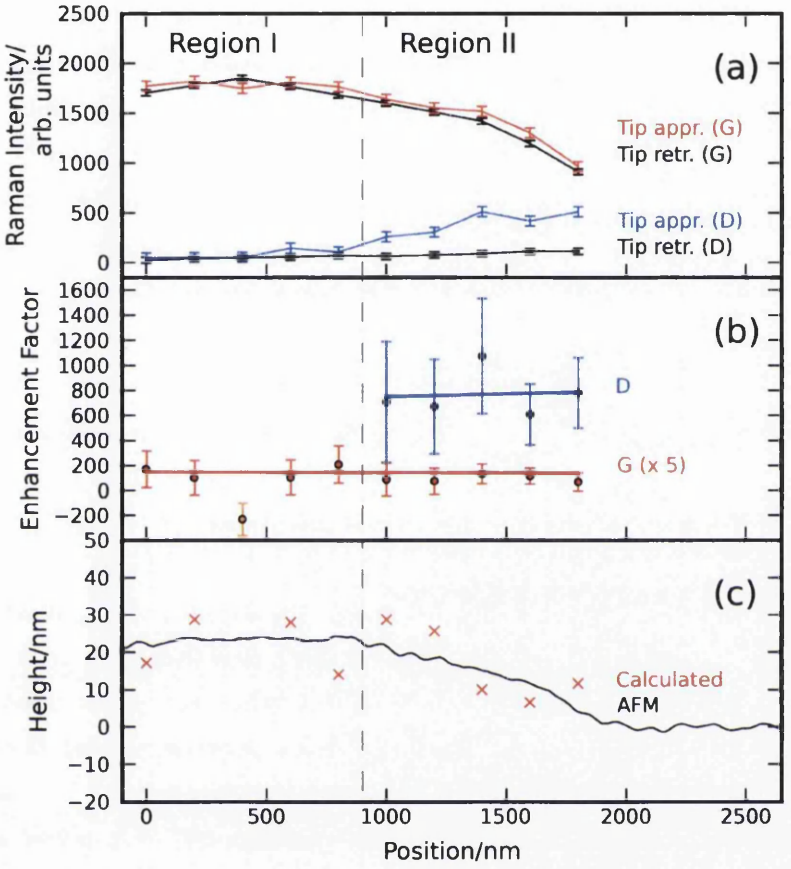

Figure 8.5: TERS and topographic data taken from the ultra thin graphitic flake presented in Figure 8.4. (a) Absolute peak intensities of the Graphite's G band (red) and D band (blue) as a function of position along the edge of the graphite flake. The coloured lines indicate the tip approached signals whilst the black lines indicate the corresponding tip retracted signals. (b) Enhancement factor calculated for the D (blue) and G (red) band as a function of position. The orange marker indicates an anomalous point that was removed for fitting. (c) Modelled flake thickness (red crosses) derived from the G band near- and far-field intensities, the G band enhancement factor and the relative illumination volumes. The AFM height profile (black trace) is plotted for comparison.

cannot observe a defect D band in this region due to low defect density. The D band is measurable in region (II) due to the staggered distribution of individual or small groups of layer edges. In order to calculate the enhancement factor we have assumed these edges are distributed evenly, giving a lateral separation of $14nm$ between each edge along the taper. The staggered edges form a two dimensional plane along the top surface of the wedge. As a result, the illumination volumes for the D peak are approximated by two dimensional circles, with a diameter of $20nm$ for the near-field and $300nm$ for the far-field based upon an approximate beam waist. In reality the edge density is not high enough to ensure that the full area will produce defect scattering, however this is not a critical consideration for this calculation since the percentage of the illumination area occupied by defects will be roughly equal in both the near- and far-field.

Figure 8.5b shows the enhancement factor calculated at each location in region (I) and (II) for the G band and for region (II) for the D band. A linear fit has been plotted which shows a gradient close to zero for both Raman bands. This demonstrates that the enhancement factor remains constant however the magnitude differs dramatically between the G and the D band with the D band expressing a substantially larger enhancement factor. Using equation 8.1, a mean enhancement factor of ~ 24 was found for the G band, whilst a factor of ~ 768 was determined for the D band, thus demonstrating preferential TERS enhancement of the D band.

The TERS contrast of the G band is dependent on changes to the relative volume of the flake, i.e. the flake thickness. Hence, relationship 8.1 can be used to derive the flake thickness as a function of contrast. The result of this calculation is plotted in Figure 8.5c whereupon crosses indicating flake thickness are plotted as a function of tip position along the flake edge. The calculated thickness is overlaid with the AFM cross-section of the flake edge and gives a respectable correlation demonstrating that it is appropriate to analyse the enhancement factor in terms of illumination volume and that our definitions provide a reasonable representation of the G peak in graphite.

The outcome of this analysis is that the increased contrast observed in the D band cannot be explained by compensating for illumination volumes since

the resultant enhancement factor of the D band is significantly (30 times) greater than that of the G band. Arguments presented in the literature often assume that the TERS enhancement factor is the same for the G and D band. This data demonstrates that this assumption is not valid for this case and that there must be additional mechanisms occurring to produce the preferential enhancement apparent in this measurement.

8.5 Multilayered graphene

We move on to discuss TERS measurements from a multilayered graphene sample on glass. The flake primarily used in this study is shown in Figure 8.6 and features step edges of between 2 and $4nm$. Graphene exhibits a stacking height of $0.335nm$ per layer which can be greater with disordered stacking [Pimenta et al., 2007] and influences from the substrate. The AFM topography gives an upper limit of 12 layers of graphene based on the layer stacking height. The colour scale for this image represents an approximate height range of 0-30 nm, with high topographic features corresponding to creases in the flake. The cross sectional line profile along the green line in area (ii) is shown in Figure 8.7. Two specific areas were explored in detail and are outlined on Figure 8.6 as area (i) and area (ii).

TERS measurements were conducted at 100 nm intervals along the indicated line in Figure 8.8a. The intensity map overlaid along the measurement line is representative of the binned intensity of the tip-enhanced D band response derived from the spectra, examples of which are given in Figure 8.8c. Dark shading indicates a strong D band response and white is indicative of a weak response. Various features of the graphene flake were surveyed by this measurement and distinct differences in the TERS response were observed that show a clear dependence on the underlying sample structure.

Flat regions away from the edges or structural distortions typically show no enhancement of the D peak and a small enhancement in the G peak with a TERS contrast of ~ 0.1. The spectra in Figure 8.8e is representative of a TERS spectrum from such a location, with this particular spectrum acquired from the green marker cross indicated on Figure 8.6. This result reinforces

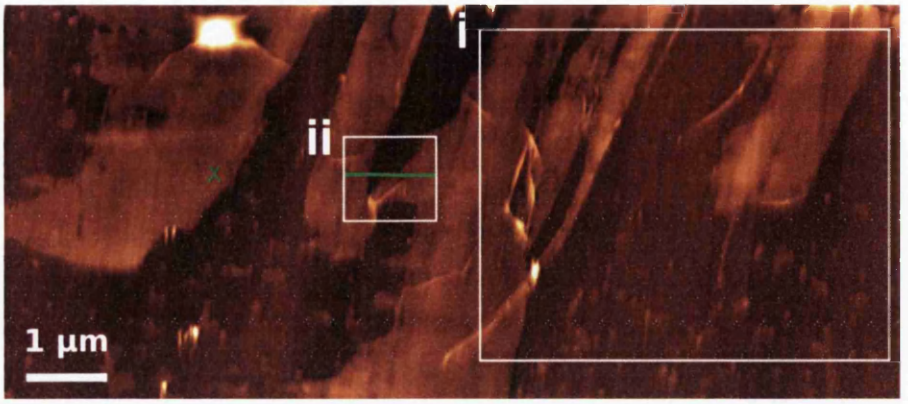

Figure 8.6: Contact mode AFM image of torn edges of ML graphene flake. A TERS measurement line is marked in green. TERS spectra were taken at 100 nm intervals across the graphene strands. TERS from area (i) is analysed in detail in Figure 8.8, and the complex spectra generated in area (ii) is summarised in Figure 8.9.

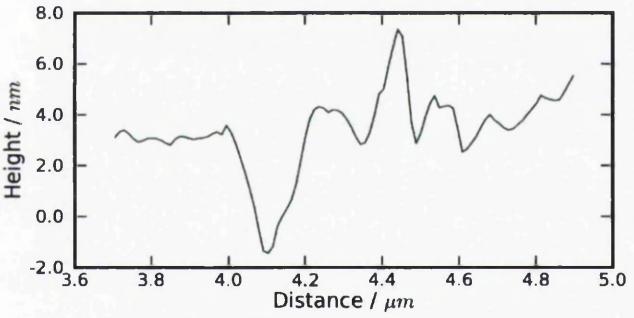

Figure 8.7: Topographic cross-section of the flake taken along the green line in Figure 8.6 using contact mode AFM. The line profile demonstrates the scale of the sample features seen in area (ii).

our previous observations from the defect free ultra-thin graphite flake (region (I)). At structural deformations a D band enhancement is observed with a mean contrast of 1.2 and this is also accompanied by an increase in the upper wing of the G band, revealing the D' band response. An enhancement of the G band with a mean contrast of 0.16 is also observed.

The strongest TERS response was recorded when the tip was positioned

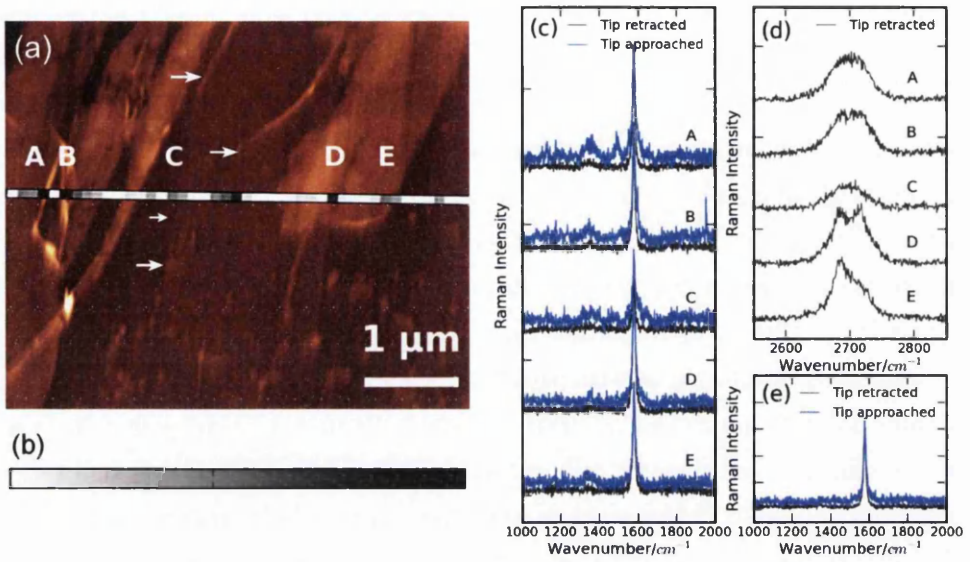

Figure 8.8: (a) AFM topography of area (i) from Figure 8.6, overlaid with contrast line-map showing the binned D band intensity. Specific spectral locations, selected due to high defect activity are indicated (A-E). The white arrows highlight small steps that are only just resolved by the AFM and imply the presence flake edges. (b) The colour scale used to represent the binned D band intensity where black indicates high intensity and white low intensity. (c) TERS spectra from the marked locations are displayed to demonstrate the TERS enhancements in the D/G range. (d) Spectra showing the G' lineshape in the far-field at the selected locations. (e) TERS spectra demonstrating typical graphene response where no defects are present. Spectra were taken with 15s acquisition and have been background corrected.

on the sharp creases in the graphene indicated by locations A and B in Figure 8.8a. Enhancement at the creases may be a direct indicator of a large number of lattice defects induced by this type of deformation. Additionally, increased sensitivity may occur on this feature due to the change in orientation of the sample relative to the tip and polarisation.

Location D shows enhancement in response to a torn edge on the layer. This indicates TERS is sensitive to edge structures. Location E is another clear example of edge related enhancement of the D band. However edges do not consistently produce a D band response. There are several defined edges shown in the AFM image between locations B and D which do not produce D

band enhancement. The lack of sensitivity to edges is likely to be a result of insufficient measurement density along the line and the coherence length. The spatial extent of the D band away from the defective structure is determined by the average distance that the photo-excited electron or hole can travel before it is inelastically scattering by a lattice phonon. This length, known as the coherence length, has been measured to be 3 nm at room temperature [Beams et al., 2011]. With a step size of 100 nm it is likely that there are examples where the tip did not land with sufficient proximity to the edge structure to see the D-band response. White arrows on Figure 8.8a indicate less clear topographic features which are likely to be responsible for some of the binned D band activity seen in location C and between locations C and D. The thin nature of the graphene flake in this region makes it harder to resolve a clear topographic distinction between the substrate glass and the graphene layer, i.e. the thinner flakes become much harder to distinguish from the glass. The fact that the signals vary considerably in their D band contribution confirms that tip contamination is not likely to be a contributing factor.

Using equation 8.1 we estimate the ratio of the enhancement factor of the D band versus the G band (γ_D/γ_G) to be > 1 for positions A and B and to be < 1 for positions C, D and E. This calculation has assumed 2 dimensional volumes, defined for the D peak by a line defect 10 nm wide with a length of 300 nm and 20 nm for the far- and near-field calculations respectively. For the G band circular illumination volumes were used with a diameter of 300 nm and 20 nm for the far- and near-field respectively. The atomic level defect distribution at the active positions on this sample are however poorly defined due to the types of structure and the limited AFM resolution. Additionally there is a large uncertainty in the contrast due to poor signal-to-noise of the Raman spectra. Despite the approximations of the model, the lack of any clear evidence to support preferential enhancement of the D band at all defect locations, as seen in graphite, indicates that the mechanism leading to increased D band response must be dependent upon the specific defect structure.

The phonon properties of graphitic films are dominated by the planar

symmetry of the material. The plasmonic tip creates an enhanced field that is polarised perpendicular to the graphitic planes. As a result the G and G' phonons are relatively inaccessible to this field leading to a weak TERS response when the tip is normal to the graphitic surface. Our data shows preferential D band enhancement occurs on graphite, but that on graphene preferential enhancement of the D band only seems to occur at certain features. Preferential enhancement has been briefly touched upon in the literature; Stadler et al. [2011a] note that the D band is less sensitive to the TERS excitation direction and suggest this may be a result of broken symmetry at defects. Thus while the G and G' bands are only weakly enhanced the defect peaks can respond more readily to the enhanced field.

Defects alter the hybridisation of the carbon atoms and produce dangling bonds. This can introduce out of plane components, such as interlayer bonds, that are no longer orthogonal to the incident field producing a stronger TERS response. For the Graphite this could explain the disparity between D and G enhancement since the G band signal is dominated by weakly enhanced in plane components whilst the D band signal is dominated by the strongly enhanced out of plane components. In graphene the strongest preferential D band enhancement was recorded at a crease in the flake which suggests that the angle of illumination relative to the local flake topography may be a key factor in producing a preferential enhancement.

Further point spectra were taken across the indicated green line of area (ii) outlined in Figure 8.6. These produced a different spectral response, a representation of which is displayed in Figure 8.9. This area of the sample has a highly distorted topography. It lies at the junction of a torn graphene strand whereby the sample has been forced to twist, overlap and crease, whilst it is also in close proximity to an edge. It is thus representative of a heavily stressed region of graphene and the TERS response shown in Figure 8.9 presents a complex set of Raman peaks that are generated.

The spectra display a large amount of activity around 1350 and 1620 cm^{-1} but also exhibit a number of other peaks that are challenging to attribute. The peak distribution is particularly hard to allocate to specific topographical properties of the sample due to limited nanoscale resolution of our AFM.

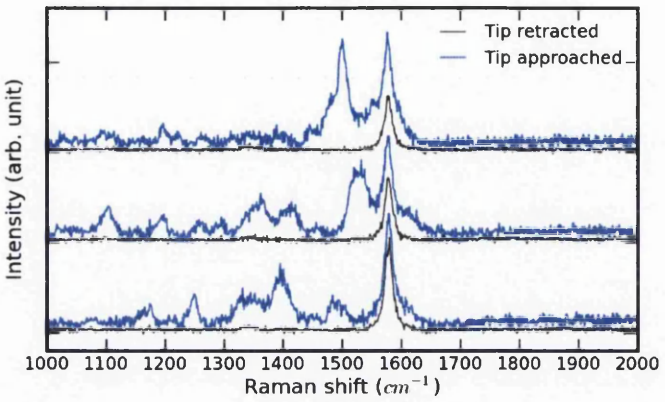

Figure 8.9: Selected TERS spectra illustrating the diversity and complexity of peak structure from the physically distorted and overlapping graphene from area (ii) in Figure 8.6.

The fact that these signals were repeatedly present within this region of the sample and not elsewhere indicates that it is highly unlikely that the tip was the source of a contamination signal. However, localised contamination of the surface feature could not be ruled out. Signatures of this nature have been presented in the TERS literature and can be attributed to carbon contaminants [Domke et al., 2007]. This attribution is due to the diverse set of bond configurations that carbon can form and its ability to reconfigure. The broad peak shape of amorphous carbon represents the range of Raman modes that are potentially accessible when the regular sp^2 order is broken and thus complex carbon Raman signatures which originate from the sample are not unexpected.

It is also expected that the distorted nature of the graphene in this region could produce a combination of stacking faults, dislocations, point defects and interlayer rotational disorder; all of which would introduce contributions towards this complex lineshape. In multilayered graphene Bernal stacking faults influence the Raman spectra causing a broadening of the peaks and an alteration of the line shape. Rotational stacking faults introduce additional peaks (R and R') either side of the G band [Carozo et al., 2011], the positions of which are dependent on the angle of rotation between the multiple layers. Geim

[2009] commented that the strain and curvature introduced by nanometer-scale corrugations can alter the local reactivity. This would be seen to manifest itself as a more complex spectral signature.

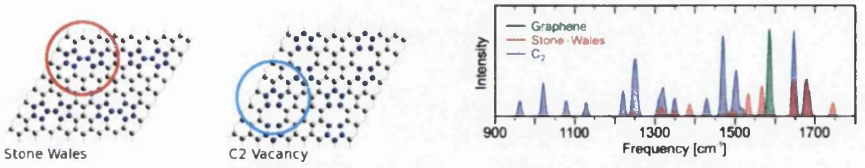

(a) Point defect configurations (b) Theoretical specta

Figure 8.10: Examples of two possible point defects (a) and their theoretically predicted Raman spectra (b) [Kudin et al., 2008]

The hybridised nature of carbon allows it to support a varying number of nearest neighbours and hence there are a range of stable, exotic structures that could be present in non-pristine graphene, such as Stone-Wales defects and C2 vacancies [Banhart et al., 2011, Zsoldos, 2010]. These topologies, illustrated in Figure 8.10, can possess a mixture of sp^2 and sp^3 bonds. Theoretical calculations show a number of additional Raman peaks may be introduced by these types of lattice configuration within the spectral range examined here [Kudin et al., 2008]. Although our spectra do not produce a direct match, many other topologies of point defects exist each with their own Raman signature and which are likely to also display a complex peak distribution. Without the TERS technique the signals in the far-field are not detectable and hence TERS offers significant promise in studying atomic defects. The spectral features we observe merit an extended investigation whereupon the allocation the lattice configuration and defect type are correlated to specific features in the TERS spectra. However due to a combination of factors such as; scanning probe resolution, tip apex geometry and the defect coherence length, more efforts are required to experimentally improve the performance of TERS so that point defects can be fully differentiated.

8.6 Summary

We found enhanced defect sensitivity on a range of topographic features. Certain structure types demonstrate preferential enhancement of the D band whereby the magnitude of the Raman enhancement is not uniform across all spectral peaks. TERS enhancements on the Raman D band were a factor of 30 greater than the G band responses for some of the sample structures studied. Our measurements illustrate what is experimentally achievable on graphene and thus promotes the use of TERS for the study of various types of defects on both ultrathin graphite and graphene multilayers. This is becoming particularly important when such defects are governing the operation of graphene-based devices. Additionally as devices become smaller to utilise quantum confinement effects (such as in nano-graphene ribbons) micro-Raman no longer offers sufficient spatial resolution for individual characterisation and so techniques such as TERS present a vital advancement. The rich spectral response acquired from some defect features supports the complexity of spectral signatures that have been theoretically proposed in the literature and indicate that atomic resolution is now required in TERS systems to underpin our understanding and characterisation of specific atomic defects.

Chapter 9

Conclusion

9.1 Overview

The primary aim of this project was to develop a new system for tip-enhanced Raman spectroscopy (TERS) measurements. The data presented in this thesis demonstrates that this has been resolutely a success with enhanced spectra recorded on resonant and non-resonant monolayer molecular films, ultra-thin graphitic films and on multilayered graphene. The secondary aim was to investigate a new application for TERS that is relevant to the field of material science. This thesis has presented results that demonstrate the potential of TERS for the characterisation of defects in graphene and has shown that our TERS configuration exhibits heightened sensitivity to defects through preferential enhancement of the defect induced D band. A characterisation technique of this nature would be of great benefit in the rapidly expanding field of graphene based devices. Currently there are few publications using TERS to study defects in graphene making this work an interesting addition to the field. We have shown that TERS exhibits heightened sensitivity to the D band on multilayered graphene and on ultra-thin graphitic films. This sensitivity could be of great use to researchers looking to further understand the role of defects for the manipulation of the electronic properties of graphene.

Moving forward follow up work is required to realise the full potential of TERS on graphene. TERS offers optical spatial resolution of 10's of

nanometers; the absolute limit of achievable resolution has yet to be fully established and even at the limit deconvolution techniques have been proposed to probe further reduced length scales [Treffer and Deckert, 2010]. Accordingly there is no strict reason to prevent optical mapping of individual lattice defects on the nano-scale. This work has shown that our TERS setup is sensitive to graphene defects, the nature of TERS means that these signals are localised to the tip apex, variations in spectra across a line map on graphene have shown that the spectral response is dependant on the lattice structure that is probed by the tip. To capitalise on these exciting results experiments need to be conducted that test the limits of spatial resolution achievable on graphene samples.

This becomes a more complex challenge; the limitation of the methodology presented in this thesis is in the scanning control. There are two factors to be aware of when testing the limits of scan resolution, the first is positional drift between the stage and head which will occur in all systems to greater or lesser extents. The influence of drift can be limited by reducing measurement times. The second limitation is scan sensitivity. This thesis has shown that our implementation of shear-force scanning is capable of sufficient feedback sensitivity to reliably image DNA. This is however still a fairly large structure compared to atomic-scale point defects in the graphene lattice. Adapted shear-force techniques have achieved atomic resolution [Seo et al., 2003] however a more straightforward approach would be to utilise scanning tunnelling microscopy (STM). An STM module can be fitted to the JPK system which would allow TERS measurements to be combined with atomic resolution topography images and enable the TERS response to be directly correlated with the physical topology of the defects. STM requires a conductive substrate and so this also introduces the benefits of gap-mode TERS to provide greater enhancement levels. If the spectral signatures of different defect types could be determined TERS would become a highly valuable member of the nanotechnology toolkit.

Alternative graphene preparation techniques must be explored since we have yet to reliably demonstrate heightened defect sensitivity on mono-layer graphene. The illumination geometry of the system has hindered the isolation

of single layered graphene; identification of mono-layered material, when utilising the exfoliation technique, is a challenge since the yield of thin flakes is small compared to thicker flakes. The optical contrast of single-layered material is not great enough to be readily visible in the optical microscope and so considerable luck is required to isolate single-layered material on glass. A more sensible approach would be to use either epitaxial graphene floated onto a substrate or by depositing graphene-oxide sheets from solution. Both of these methods would allow a gold-coated substrate to be used enabling both gap-mode TERS and STM imaging.

Despite not being able to achieve the full realisation of this application, the experimental gains accomplished through the development of the system and the demonstration of the capability and potential of our equipment applied to this important application are a pivotal contribution to the research work conducted by the Swansea nano-optics group. The work has built strong foundations for the groups ongoing progress in this field. Collaborations formed with ETH as part of this project and publications extend the reach of the work to the wider scientific community.

9.2 Development milestones

The development of the system has featured many step changes in capability. Each step has progressed the system from one that was incapable of TERS measurements towards the final configuration that can successfully achieve reliable, repeatable and complex TERS measurements.

9.2.1 Imaging

The initial hurdle was to achieve sensitive tip-sample distance control. This involved working with JPK to tune and adapt the feedback mechanisms available in order to obtain stable and reliable imaging conditions when using our solid etched tips in shear-force configuration. We now have access to two feedback systems which both offer sufficient surface sensitivity. The primary feedback system is *Hyperdrive* mode which operates on phase feedback;

through testing a number of protocols we have found that damping is required, using Q control, to improve phase stability of the tuning fork response. This mode is effective for high Q factor tuning fork assemblies. Lower Q fork assemblies, or certain coated samples, require *tuning fork* mode which operates on the phasor mixing of amplitude and phase as its feedback mechanism. Shear-force imaging sensitivity has been demonstrated on strands of DNA and on graphene flakes.

9.2.2 Software

The software shipped with the system has been adapted to suit the specific needs of TERS measurements and works within the limitations presented by the manufacturers individual software packages. Improvements have been made through bug fixes and the extension of scripts to provide greater capabilities. For point spectroscopy much of these advances are not a necessity however the use of scripts present significant gains when coordinating complex mapped measurements. It is now straightforward to collect large datasets with both tip in and tip out measurements. A greater range of measurements can be conducted such as synchronously moving the sample with the tip to map a laser spot on an in-homogeneous sample. Furthermore the speed of the TERS procedure has been improved by introducing concepts such as separate sample and laser reference frames with automated conversion between the two allowing the tip to be repositioned without requiring a full rescan of the sample.

To manage the large datasets a database has been set up to collate the data from the two sides of the TERS system onto one computer. From here automated processing can be conducted that correlates the TERS results with the sample position, applies filtering and does calculations on enhanced peaks. An output is provided which facilitates rapid review of the data. The processing software is closely linked to the measurement scripts to ensure that all relevant parameters are stored and that the integrity of the data is maintained.

There is still further scope for software development. The Renishaw

WIRE software is the biggest restriction to the measurement possibilities. It is currently not possible to produce a live analysis of the data. Data has to be exported from the Renishaw software and run through the custom processing software. It would be beneficial to bypass the Renishaw software and collect the spectral data directly from the CCD using a LabView or equivalent interface. The networked TCP/IP communication would operate between this interface and the JPK machine, the Renishaw software would then only be required to setup measurement paths. This approach would offer the most flexible and powerful solution. It would enable live analysis of the TERS data plus present an interface that is tailored to TERS making it more user friendly to non TERS specialists. The flexibility would open up a greater range of measurement possibilities making it a stronger development system.

The JPK system presents one major limitation which currently creates a bottle neck that significantly slows mapped measurements. The SPM has no capabilities of moving between measurement points in-feedback and so a full retract and approach must be conducted with each new measurement point. Shear-force requires a slow approach and so this leads to a delay of $\sim 5s$ for each measurement point in a grid. This is substantial, TERS publications presenting mapped data often utilise collection times of a fraction of a second per point with highly active tips. The overall measurement time is highly important for high resolution measurements in order to minimise the effects of drift and to limit the influence of the degradation in the enhanced tip response over time. It is not beyond the potential of the system to move from point to point in feedback and further work should be conducted with the JPK engineers to realise this.

9.2.3 TERS enhancement

The samples presented in this thesis have been divided into two categories thin molecular monolayers and crystalline films. Chronologically enhancements were first observed on a low quality Graphitic film yielding broad, poorly defined peaks, this data has not been presented in the thesis but inspired

future work on better quality graphitic films. This lead on to the HOPG work and subsequently the work on multilayer graphene presented in Chapter 8. These samples enabled the development of topographic scanning, TERS procedures and TERS alignment on challenging in-homogenous samples. Mapping techniques and the corresponding data processing were refined on these sample systems. Graphene has also allowed us to demonstrate a new and valuable purpose for the TERS technique.

To further try and understand and optimise the optical efficiency of the system we then moved to thin films, firstly Rhodamine 6G since it was considered an easy and responsive sample however we only managed to achieve modest, stable enhancements from it. Large enhancements were obtained from contaminant peaks. This work was followed up by the enhancements on a self assembled thiophenole monolayer.

The experimental configuration has progressed throughout this study and it has adapted according to the needs of the individual samples and as a result of continued optimisation. Table 9.1 details a summary of the main configuration changes that have occurred with each of the presented datasets. The illumination path and radial polariser have been the most fundamental changes to the system. Moving from path I1 to I2 (see Figure 4.3) improved optical efficiency by removing a beamsplitter that was dumping half the collected Raman signal. The radial polariser position was moved to match this path and then subsequently moved to achieve better beam conditioning at the focus by positioning it before the pinhole. This has produced a much cleaner focus and so it is thought to have improved the polarisation conditions at the focus through cleaner cancelling of the transverse polarisation components.

Table 9.1: Experimental configuration and measurement parameters for the main results detailed in this thesis. Path and radial polariser (RP) position are defined in Figure 4.3

Sample	Path	RP position	Power at tip $[\mu W]$	Objective	TERS contrast	Section
HOPG	I1	RP 1	1400	63×	D=4, G=0.08	8.4
ML graphene	I1	RP 1	200	100×	D=1.2, G=0.16	8.5
Rhodamine 6G	I2	RP 2	35	63×	0.6	7.2.5
Thiophenole	I2	RP 3	700	63×	NA	7.3

Two objective lenses have been used in this study a 100× (1.25NA) and

a 63× (0.90NA). On paper the 100× objective features a higher NA and so would be the better choice. This lens was however lower quality than the 63× (0.90NA) and the oil immersion presented operational difficulties that were not outweighed by the optical gains provided by the higher magnification objective. This is still an area of concern since the 63× objective features an NA of 0.90 which lies at the lower bound of what is deemed effective for TERS in bottom illumination. A good quality high NA objective would be a sensible and recommended upgrade to the system.

The laser power used for enhanced measurements is dependant in part on the sample. In general the power utilised is matched to the tolerance of the sample. Higher laser powers produce more signal but also cause heating effects at the tips which can lead to reduced enhancement and lead to damage to the sample or tip. Measurements on new samples always start with a low laser power and work upwards to establish the minimum laser power that produces a resolvable signal. The power utilised is thus a rough convolution of the collection efficiency and responsiveness of the sample.

The Rhodamine 6G dye molecules are resonant Raman scatterers and require only a low laser power whilst the weak response of the thiophenole molecules demanded higher powers. Carbon contamination has been discussed in detail in Chapter 7 it would be a sensible assumption that the intensity of any contamination signal is related to the laser power used. Contamination effects were seen more prevalently on the thiophenole sample than on the R6G sample. The presence of contaminant signal was however not observed on the HOPG sample which featured the highest incident laser power but there were some signs of a contamination style signal on the graphene sample at certain regions of the sample. This would imply that it has to do with the particular local resilience of the sample and that contamination signals may originate from carbon that has been released due to damage to the sample molecules from the laser illumination. Thus on certain regions of the graphene sample, where residue has been left from the sticky tape, it may be that the breakdown of molecules in the residue contribute the carbon for the observed transient carbon peaks as discussed in the graphene chapter. The signal may alternatively originate from a range of defect types present in the graphene

lattice and we have shown publications that support this however further work is required to clarify this issue.

9.3 Enhancement levels

We are achieving an acceptable level of repeatability with roughly 1 in 2 of the tips selected for use producing a TERS enhancement however the observed contrast factors are still fairly modest. In reality the magnitude of the enhancement is not critical as long as it provides sufficient enhancement to be seen above the far-field background. Increased signals do however help to decrease collection times which is particularly important for mapped measurements plus it allows the technique to be extended to weakly scattering samples which is the case in the majority of biological applications. Any observable near-field enhancement reports on a localised response and so gives information that is not accessible by far-field observation. This section comments on factors that may be influencing the magnitude of the enhanced response. The discussion splits into three parts; collection efficiency; polarisation at the tip; and tip geometry.

9.3.1 Optical efficiency

The collection efficiency of the spectrometer is now as optimised as possible without undertaking any major overhauls of the instrument. A high NA objective, however, would improve the optical collection and produce stronger z polarisation conditions at the tip. Both the illumination conditions and collection efficiency would benefit from utilising a high NA objective. There is also scope to improve beam quality and polarisation conditions at the tip which can be achieved by addressing issues in the beam expansion, pinhole and radial polariser utilised in path I2. The radial polariser could be replaced with an 8 segment or etched non segmented radial polariser to achieve better beam conditioning, this however I do no believe is pivotal. Beam expansion prior to the radial polariser is of importance in order to minimise the proportion of the beam that is dominated by the glued segments at the centre of the optic.

The beam must be focused through a pinhole to create the doughnut mode and lead to clean cancelation of the transverse components of the polarisation when the beam is focused at the sample. The current pinhole optic combines beam expansion and so a new pinhole arrangement is required utilising a 1:1 lens configuration. Finally polarisation rectifying optics could be introduced to compensate for a degradation in the polarisation quality that occurs at each mirror.

9.3.2 Tip geometry

The tip geometry is still a notable cause for concern. We are manufacturing tips that are TERS active and have an acceptable level of repeatability but it is likely that tip geometry is limiting the TERS enhancement. The typical geometry of our tips is dominated by grain boundaries and as such may not be fully exploiting the lightning rod effect as discussed in Chapter 7. Moving to a new etch method based upon perchloric acid may be a sensible development as this etch is known to be less aggressive and produce smoother less grain dominated tips. A comparison with gold tips may also prove valuable, we have produced gold tips in the past and so know that we can fabricate smooth, sharp gold tips; gold tips have not yet been tested in the new TERS system.

9.3.3 Tip-sample separation

A further cause of low enhancement may be too great a tip-sample separation. Shear force is sensitive to long range interactions and tends to operate within 15 nm from the sample. It is possible that even with a heavy setpoint the tip is not being held close enough to the sample. This hypothesis is backed up by the fact we saw no observable improvement in enhancement levels when operating in gap-mode configuration. Gap-mode requires a separation of around 5 nm. Since the near-field decays exponentially getting the separation control correct is vital in order to maximise the enhancement factor. To establish whether this is the case a direct comparison with STM would be recommended. The SPM can be operated in STM mode with the appropriate

tip module. The more precise tip-sample distance control would be useful for aiding to calibrate the shear-force setup.

9.3.4 Speed

The speed of the TERS procedure is an important consideration. Every effort has been made to minimise the time between fabrication and the TERS measurement to ensure that the tip is in its most active state when measurements are conducted. Further alterations can still be made to improve the speed of mounting and of the TERS procedure. Moving to an STM module would allow glue-less mounting of the tip and remove a highly delicate operation from the mounting procedure. The current mounting method required leaving the etched tip on a very small length of wire. This process is time consuming and introduces a number of steps that could damage or contaminate the tip if a mistake is made. Speed improvements can also be made in the mapping procedure as discussed previously. Speed should be the central consideration for further development of the system as it raises the chances of strong enhancements and makes the TERS measurement procedure more user friendly making it more suitable for routine measurements and allows a greater throughput of tips.

9.4 Outlook

The success delivered in this project would be further fulfilled if the heightened defect sensitivity observed for TERS measurements on graphitic-films could be confirmed on mono-layer graphene. Extensions of this work would look to push spatial resolution and identify the spectral signatures of specific defect types which would enable TERS to become a highly valuable technique for the detection and characterisation of defect structures in graphene.

From here there are many exciting avenues that are left to explore. Our TERS system features significant adaptability and offers the ability to change a range of key parameters that have only been briefly touched upon in this work such as laser wavelength; tip material; solid and coated probes and

alternative feedback systems including AFM and STM. There is still much debate about the most optimal conditions for TERS and the flexibility of this system allows experiments to be conducted that directly compare the different materials, fabrication processes and illumination conditions.

The broad range of measurements supported by this system stretches beyond TERS to include SNOM, fluorescence, TIRF, kelvin probe AFM and STM amongst many others. The sample conditions can be controlled with modules enabling SPM in liquid and full temperature control. This creates the possibility to look at a massive diversity of samples and to carry out a range of complimentary measurements on the same system. The breadth of TERS measurements being published is growing and more work is being conducted on complex biological samples which generally are less resilient, more challenging to image and exhibit a weak Raman response compared to crystalline materials. This system is a suitable test-bed for moving on to biological samples, the work on thiophenole mono-layers shows that we can observe enhancements on structures with a low Raman cross section and the development of procedures on graphene has provided the control required for negotiating complex, inhomogenous samples.

Bibliography

V Abramova, A S Slesarev, and J M Tour. Meniscus-Mask Lithography for Narrow Graphene Nanoribbons. *ACS Nano*, 7(8):6894–6898, 2013.

P M Ajayan and J M Tour. Materials Science: Nanotube composites. *Nature*, 447(7148):1066–1068, 2007.

M Antognozzi, M D Szczelkun, A D L Humphris, and M J Miles. Increasing shear force microscopy scanning rate using active quality-factor control. *Applied Physics Letters*, 82(17):2761, 2003.

P Avouris, Z Chen, and V Perebeinos. Carbon-based electronics. *Nature Nanotechnology*, 2(10):605–615, 2007.

E Bailo and V Deckert. Tip-enhanced Raman scattering. *Chemical Society Reviews*, 37:921–930, 2008.

R Bakry, R M Vallant, M Najam-ul Haq, M Rainer, Z Szabo, C W Huck, and G K Bonn. Medicinal applications of fullerenes. *International Journal of Nanomedicine*, 2(4):639, 2007.

F Banhart, J Kotakoski, and A V Krasheninnikov. Structural Defects in Graphene. *ACS Nano*, 5(1):26–41, 2011.

R Beams, L G Cançado, and L Novotny. Low Temperature Raman Study of the Electron Coherence Length near Graphene Edges. *Nano Letters*, 11(3): 1177–1181, 2011.

A Bek, R Vogelgesang, and K Kern. Apertureless scanning near field optical microscope with sub-10 nm resolution. *Review Of Scientific Instruments*, 77(4):043703, 2006.

E Betzig and J TRAUTMAN. Near-field optics- Microscopy, spectroscopy, and surface modification beyond the diffraction .... *Science*, 257:189–195, 1992.

C Blum, T Schmid, L Opilik, S Weidmann, S R Fagerer, and R Zenobi. Understanding tip-enhanced Raman spectra of biological molecules: a combined Raman, SERS and TERS study. *Journal Of Raman Spectroscopy*, 43(12):1895–1904, 2012.

R Böhme, M Richter, D Cialla, P Roesch, V Deckert, and J Popp. Towards a specific characterisation of components on a cell surface - combined TERS-investigations of lipids and human cells. *Journal Of Raman Spectroscopy*, 40(10):1452–1457, 2009.

N N Brandt, O O Brovko, A Y Chikishev, and O D Paraschuk. Optimization of the Rolling Circle Filter for Raman Background Subtraction. *Applied Spectrocopy*, 60(3):288–293, 2006.

L G Cançado, A Hartschuh, and L Novotny. Tip-enhanced Raman spectroscopy of carbon nanotubes. *Journal of Raman Spectroscopy*, 40:1420–1426, 2009.

V Carozo, C M Almeida, E H M Ferreira, L G Cançado, C A Achete, and A Jorio. Raman Signature of Graphene Superlattices. *Nano Letters*, 11 (11):4527–4534, 2011.

C Casiraghi, A Hartschuh, H Qian, S Piscanec, C Georgi, A Fasoli, K S Novoselov, D M Basko, and A C Ferrari. Raman Spectroscopy of Graphene Edges. *Nano Letters*, 9(4):1433–1441, 2009.

A H Castro Neto, F Guinea, N Peres, K S Novoselov, and A K Geim. The electronic properties of graphene. *Reviews of Modern Physics*, 81(1):109–162, 2009.

J Chae, S Jung, S Woo, H Baek, J Ha, Y J Song, Y W Son, N B Zhitenev, J A Stroscio, and Y Kuk. Enhanced Carrier Transport along Edges of Graphene Devices. *Nano Letters*, 12(4):1839–1844, 2012.

J Chen, M Badioli, P Alonso-González, S Thongrattanasiri, F Huth, J Osmond, M Spasenović, A Centeno, A Pesquera, P Godignon, A Z Elorza, N Camara, F J G de Abajo, R Hillenbrand, and F H L Koppens. Optical nano-imaging of gate-tunable graphene plasmons. *Nature*, 487(7405):77–81, 2012.

Z Chen, Y M Lin, M J Rooks, and P Avouris. Graphene nano-ribbon electronics. *Physica E-Low-Dimensional Systems & Nanostructures*, 40(2): 228–232, 2007.

X Cui, W Zhang, B Yeo, and R Zenobi. Tuning the resonance frequency of Ag-coated dielectric tips. *Optics Express*, 15(13):8309–8316, 2000.

C de las Casas and W Li. A review of application of carbon nanotubes for lithium ion battery anode material. *Journal of Power Sources*, 208:74–85, 2012.

Django Framework. Django Software Foundation. www.djangoproject.com, 2013.

K F Domke, D Zhang, and B Pettinger. Enhanced Raman Spectroscopy: Single Molecules or Carbon? *ACS Publications*, 111(24):8611–8616, 2007.

R Dorn, S Quabis, and G Leuchs. Focusing a radially polarized light beam to a significantly smaller spot size. *Physics Review Letters*, 91(23), 2003.

A Downes, R Mouras, M Mari, and A Elfick. Optimising tip-enhanced optical microscopy. *Journal Of Raman Spectroscopy*, 40(10):1355–1360, 2009.

M S Dresselhaus, A Jorio, and R Saito. Characterizing Graphene, Graphite, and Carbon Nanotubes by Raman Spectroscopy. *Annual Review of Condensed Matter Physics*, 1(1):89–108, 2010.

EasyGui. S R Ferg. easygui.sourceforge.net, 2013.

H Esmaeilzadeh, E Blem, R St Amant, K Sankaralingam, and D Burger. Dark silicon and the end of multicore scaling. *Computer Architecture (ISCA)*, pages 365–376, 2011.

A C Ferrari, J C Meyer, V Scardaci, C Casiraghi, M Lazzeri, F Mauri, S Piscanec, D Jiang, K S Novoselov, S Roth, and A K Geim. Raman Spectrum of Graphene and Graphene Layers. *Physical Review Letters*, 97 (18):187401, 2006.

K Furusawa, H Ishitobi, and S Kawata. Deep UV tip enhanced Raman scattering. *Journal of Raman Spectroscopy*, 40:1324–1330, 2009.

A K Geim. Graphene: Status and Prospects. *Science*, 324:1530–1534, 2009.

A K Geim and K S Novoselov. The rise of graphene. *Nature Materials*, 6: 183–191, 2007.

C Georgi and A Hartschuh. Tip-enhanced Raman spectroscopic imaging of localized defects in carbon nanotubes. *Applied Physics Letters*, 97(14): 143117, 2010.

A Hartschuh, N Anderson, and L Novotny. Near-field Raman spectroscopy using a sharp metal tip. *Journal of Microscopy*, 210(3):234–240, 2002.

A Hartschuh, H Qian, C Georgi, M Böhmler, and L Novotny. Tip-enhanced near-field optical microscopy of carbon nanotubes. *Analytical And Bioanalytical Chemistry*, 394(7):1787–1795, 2009.

A Hashimoto, K Suenaga, A Gloter, K Urita, and S Lijima. Direct evidence for atomic defects in graphene layers. *Nature*, 430(7002):870–873, 2004.

J Hass, W A de Heer, and E H Conrad. The growth and morphology of epitaxial multilayer graphene. *Journal of Physics Condensed Matter*, 20 (32):323202, 2008.

N Hayazawa, Y Inouye, Z Sekkat, and S Kawata. Near-field Raman scattering enhanced by a metallized tip. *Chemical Physics Letters*, 335:369–374, 2001.

N Hayazawa, Alvarado Tarun, and Y Inouye. Near field enhanced raman spectroscoy using side illumination optics. *Journal Of Applied Physics*, 92 (12):6983–6986, 2002.

N Hayazawa, Y Inouye, and S Kawata. DFT vibrational calculations of rhodamine 6G adsorbed on silver: Analysis of tip-enhanced Raman spectroscopy. *Journal Of Physical Chemistry B*, 109:5012–5020, 2005.

J Homola, S Yee, and G Gauglitz. Surface plasmon resonance sensors: review. *Sensors & Actuators: B. Chemical*, 54:3–15, 1999.

H Hoppe and N S Sariciftci. Organic solar cells: An overview. *Journal of Materials Research*, 19(07):1924–1945, 2011.

C Höppener, R Beams, and L Novotny. Background suppression in near-field optical imaging. *Nano Letters*, 9(2):903–908, 2009.

P Hoyer, T Staudt, J Engelhardt, and S W Hell. Quantum Dot Blueing and Blinking Enables Fluorescence Nanoscopy. *Nano Letters*, 2010.

A Huber, F Keilmann, J Wittborn, J Aizpurua, and R Hillenbrand. Terahertz near-field nanoscopy of mobile carriers in single semiconductor nanodevices. *Nano Letters*, 8(11):3766–3770, 2008.

T Ichimura, H Watanabe, Y Morita, P Verma, S Kawata, and Y Inouye. Temporal Fluctuation of Tip-Enhanced Raman Spectra of Adenine Molecules. *Journal Of Physical Chemistry C*, 111(26):9460–9464, 2007.

X Jia, J Campos-Delgado, M Terrones, V Meunier, and M S Dresselhaus. Graphene edges: a review of their fabrication and characterization. *Nanoscale*, 3(1):86–95, 2011.

P B Johnson and R W Christy. Optical Constants of the Noble Metals. *Physical Review B*, 6(12):4370–4379, 1972.

A Jorio, E H M Ferreira, M V O Moutinho, F Stavale, C A Achete, and R B Capaz. Measuring disorder in graphene with the G and D bands. *Physica Status Solidi (b)*, 247(11-12):2980–2982, 2010.

Jython Programming Language. Python Software Foundation. www.jython.org, 2013.

K Karrai and R Grober. Piezoelectric tip sample distance control for near field optical microscopes. *Applied Physics Letters*, 66(14):1842–1844, 1995.

K Kordás, T Mustonen, G Tóth, H Jantunen, and M Lajunen. Inkjet printing of electrically conductive patterns of carbon nanotubes. *Small*, 2(8–9): 1021–1025, 2006.

H W Kroto, J R Heath, S C O'Brien, R F Curl, and R E Smalley. C_{60}: Buckminsterfullerene. *Nature*, 318(6042):162–163, 1985.

K N Kudin, B Ozbas, H C Schniepp, R K Prud'homme, I A Aksay, and R Car. Raman Spectra of Graphite Oxide and Functionalized Graphene Sheets. *Nano Letters*, 8(1):36–41, 2008.

L Liao, Y C Lin, M Bao, R Cheng, J Bai, Y Liu, Y Qu, K L Wang, Y Huang, and X Duan. High-speed graphene transistors with a self-aligned nanowire gate. *Nature*, 467(7313):305–308, 2010.

Y M Lin, K A Jenkins, A Valdes-Garcia, J P Small, D B Farmer, and P Avouris. Operation of Graphene Transistors at Gigahertz Frequencies. *Nano Letters*, 9(1):422–426, 2009.

Y M Lin, A Valdes-Garcia, S J Han, D B Farmer, I Meric, Y Sun, Y Wu, C Dimitrakopoulos, A Grill, P Avouris, and K A Jenkins. Wafer-Scale Graphene Integrated Circuit. *Science*, 332(6035):1294–1297, 2011.

M Liu, X Yin, E Ulin-Avila, B Geng, T Zentgraf, L Ju, F Wang, and X Zhang. A graphene-based broadband optical modulator. *Nature*, 474(7349):64–67, 2011.

J Lloyd. *The Development of Tip-Enhanced Raman Spectroscopy.* PhD thesis, Swansea University, 2012.

Lloyd, J S, A Williams, R H Rickman, A McCowen, and P R Dunstan. Reproducible electrochemical etching of silver probes with a radius of

curvature of 20 nm for tip-enhanced Raman applications. *Applied Physics Letters*, 99(14):143108, 2011.

L M Malard, M A Pimenta, and G Dresselhaus. ScienceDirect - Physics Reports : Raman spectroscopy in graphene. *Physics Reports*, 473:51–81, 2009.

R Maximiano, R Beams, L Novotny, A Jorio, and L G Cançado. Mechanism of near-field Raman enhancement in two-dimensional systems. *Physical Review B*, 85(23):235434, 2012.

L Meng, R Wu, L Zhang, L Li, S Du, Y Wang, and H J Gao. Multi-oriented moiré superstructures of graphene on Ir(111): experimental observations and theoretical models. *Journal of Physics: Condensed Matter*, 24(31): 314214, 2012.

N Mermin. Crystalline Order in Two Dimensions. *Physical review*, 176(1): 250–254, 1968.

J C Meyer, A K Geim, M I Katsnelson, K S Novoselov, T J Booth, and S Roth. The structure of suspended graphene sheets. *Nature*, 446(7131): 60–63, 2007.

S A Meyer, E C L Ru, and P G Etchegoin. Quantifying Resonant Raman Cross Sections with SERS. *The Journal of Physical Chemistry A*, 114(17): 5515–5519, 2010.

MySQL. Oracle. www.mysql.com, 2013.

R R Nair, M Sepioni, I L Tsai, O Lehtinen, J Keinonen, A V Krasheninnikov, T Thomson, A K Geim, and I V Grigorieva. Spin-half paramagnetism in graphene induced by point defects. *Nature Physics*, 8(3):199–202, 2012.

C Neacsu, S Berweger, and M Raschke. Tip-Enhanced Raman Imaging and Nanospectroscopy: Sensitivity, Symmetry, and Selection rules. *Nanobiotechnology*, 3:172–196, 2007.

C C Neacsu, S Berweger, Robert L Olmon, L V Saraf, C Ropers, and M B Raschke. Near-Field Localization in Plasmonic Superfocusing: A Nanoemitter on a Tip. *Nano Letters*, 2010.

U Neugebauer, P Rosch, M Schmitt, J Popp, C Julien, A Rasmussen, C Budich, and V Deckert. On the way to nanometer-sized information of the bacterial surface by tip-enhanced Raman spectroscopy. *ChemPhysChem*, 7(7):1428–1430, 2006.

K S Novoselov. Electric Field Effect in Atomically Thin Carbon Films. *Science*, 306(5696):666–669, 2004.

K S Novoselov. Nobel Lecture: Graphene: Materials in the Flatland. *Reviews of Modern Physics*, 83(3):837–848, 2011.

K S Novoselov, D Jiang, F Schedin, T J Booth, V V Khotkevich, S V Morozov, and A K Geim. Two-dimensional atomic crystals. *Proceedings of the National Academy of Sciences*, 102(30):10451–10453, 2005.

L Novotny and B Hecht. *Principles of Nano-Optics*. Cambridge University Press, 2006.

E A Obraztsova, A V Osadchy, Ea D Obraztsova, S Lefrant, and I V Yaminsky. Statistical analysis of atomic force microscopy and Raman spectroscopy data for estimation of graphene layer numbers. *Physica Status Solidi B-Basic Solid State Physics*, 245(10):2055–2059, 2008.

OpenCV. itseez. opencv.org, 2013.

PeakDetect. sixtenbe. gist.github.com/sixtenbe/1178136, 2011.

N Peica, S Röhrig, A Rüdiger, K Brose, C Thomsen, and J Maultzsch. Characterization of dye molecules and carbon nanostructures by tip-enhanced Raman spectroscopy. *Physica Status Solidi B-Basic Solid State Physics*, 246(11-12):2708–2712, 2009.

B Pettinger. Tip-enhanced Raman spectroscopy of 6H-SiC with graphene adlayers: selective suppression of E1 modes. *Journal Of Raman Spectroscopy*, 40:142–1433, 2009.

B Pettinger, B Ren, G Picardi, R Schuster, and Ertl Gerhard. Tip-enhanced Raman spectroscopy (TERS) of malachite green isothiocyanate at Au (111): bleaching behavior under the influence of high electromagnetic fields. *Journal of Raman Spectroscopy*, 36:541–550, 2005.

B Pettinger, K Domke, D Zhang, G Picardi, and R Schuster. Tip-enhanced Raman scattering: Influence of the tip-surface geometry on optical resonance and enhancement. *Surface Science*, 603:1335–1341, 2009.

M A Pimenta, G Dresselhaus, M S Dresselhaus, L G Cançado, A Jorio, and R Saito. Studying disorder in graphite-based systems by Raman spectroscopy. *Physical Chemistry Chemical Physics*, 9(11):1276–1290, 2007.

D W Pohl, W Denk, and M Lanz. Optical stethoscopy: Image recording with resolution lambda/20. *Applied Physics Letters*, 44(7):651–653, 1984.

Python 2.7 Documentation. Python Software Foundation. docs.python.org/2, 2013.

Python Programming Language. Python Software Foundation. www.python.org, 2013.

S Quabis, R Dorn, M Eberler, O Glöckl, and G Leuchs. Focusing light to a tighter spot. *Optics Communications*, 179:1–7, 2000.

C V Raman. A Change of Wave-length in Light Scattering. *Nature*, 121 (3051):619–619, 1928.

A Rasmussen and V Deckert. Surface- and tip-enhanced Raman scattering of DNA components. *Journal Of Raman Spectroscopy*, 37(1-3):311–317, 2006.

A Reina, X Jia, J Ho, D Nezich, H Son, V Bulovic, M S Dresselhaus, and J Kong. Large Area, Few-Layer Graphene Films on Arbitrary Substrates by Chemical Vapor Deposition. *Nano Letters*, 9(1):30–35, 2009.

A Ruiter, J Veerman, K Van der Werf, and N F van Hulst. Dynamic behavior of tuning fork shear-force feedback. *Applied Physics Letters*, 71(1):28–30, 1997.

M J Rust, M Bates, and X Zhuang. Sub-diffraction-limit imaging by stochastic optical reconstruction microscopy (STORM). *Nature Methods*, 3(10):793–796, 2006.

S Ryu, J Maultzsch, M Y Han, P Kim, and L E Brus. Raman Spectroscopy of Lithographically Patterned Graphene Nanoribbons. *ACS Nano*, 5(5): 4123–4130, 2011.

Y Saito, P Verma, K Masui, Y Inouye, and S Kawata. Nano-scale analysis of graphene layers by tip-enhanced near-field Raman spectroscopy. *Journal Of Raman Spectroscopy*, 40(10):1434–1440, 2009.

M Scarselli, P Castrucci, and M De Crescenzi. Electronic and optoelectronic nano-devices based on carbon nanotubes. *Journal of Physics Condensed Matter*, 24(31):313202, 2012.

F Schedin, A K Geim, S V Morozov, E W Hill, P Blake, M I Katsnelson, and K S Novoselov. Detection of individual gas molecules adsorbed on graphene. *Nature Materials*, 6:1–10, 2007.

T Schmid, A Messmer, B S Yeo, W Zhang, and R Zenobi. Towards chemical analysis of nanostructures in biofilms II: tip-enhanced Raman spectroscopy of alginates. *Analytical And Bioanalytical Chemistry*, 391(5):1907–1916, 2008.

T Schmid, B S Yeo, G Leong, J Stadler, and R Zenobi. Performing tip enhanced Raman spectroscopy in liquids. *Journal Of Raman Spectroscopy*, 40(10):1392–1399, 2009.

Z D Schultz, S J Stranick, and I W Levin. Tip-Enhanced Raman Spectroscopy and Imaging: An Apical Illumination Geometry. *Applied Spectroscopy*, 62 (11):1173–1179, 2008.

Y Seo, H Choe, and W Jhe. Atomic-resolution noncontact atomic force microscopy in air. *Applied Physics Letters*, 83(9):1860, 2003.

V Snitka, R D Rodrigues, and V Lendraitis. Novel gold cantilever for nano-Raman spectroscopy of graphene. *Microelectronic Engineering*, 88(8): 2759–2762, 2011.

J Stadler, C Stanciu, C Stupperich, and A Meixner. Tighter focusing with a parabolic mirror. *Optics Letters*, 33(7):681–683, 2008.

J Stadler, T Schmid, and R Zenobi. Nanoscale Chemical Imaging Using Top-Illumination Tip-Enhanced Raman Spectroscopy. *Nano Letters*, 10: 4514–4520, 2010.

J Stadler, T Schmid, and R Zenobi. Nanoscale Chemical Imaging of Single-Layer Graphene. *ACS Nano*, 5(10):8442–8448, 2011a.

T Stadler, P Opilik, P Kuhn, P S Dittrich, and R Zenobi. Tip-enhanced Raman spectroscopic imaging of patterned thiol monolayers. *Beilstein Journal of Nanotechnology*, 2:509, 2011b.

M Stalder and M Schadt. Linearly polarized light with axial symmetry generated by liquid-crystal polarization converters. *Optics Letters*, 21:1–3, 1996.

J Steidtner and B Pettinger. High-resolution microscope for tip-enhanced optical processes in ultrahigh vacuum. *Review Of Scientific Instruments*, 78:103104, 2007.

R Stöckle, Y Suh, V Deckert, and R Zenobi. Nanoscale chemical analysis by tip-enhanced Raman spectroscopy. *Chemical Physics Letters*, 318:131–136, 2000.

S J Stranick and L Novotny. Near-field optical microscopy and spectroscopy with pointed probes. *Annual Review of Physical Chemistry*, 57:303–331, 2006.

E H Synge. A suggested method for extending the microscopic resolution into the ultramicroscopic region. *Phil. Mag.*, 6(356), 1928.

M Terrones, A R Botello-Méndez, J Campos-Delgado, F López-Urías, Y I Vega-Cantú, F J Rodríguez-Macías, A L Elías, E Mu~noz-Sandoval, A G Cano-Márquez, J C Charlier, and H Terrones. Graphene and graphite nanoribbons: Morphology, properties, synthesis, defects and applications. *Nano Today*, 5(4):351–372, 2010.

S Thompson and S Parthasarathy. Moore's law: the future of Si microelectronics. *Materials Today*, 9(6):20–25, 2006.

R Treffer and V Deckert. Recent advances in single-molecule sequencing. *Current Opinion in Biotechnology*, 21(1):4–11, 2010.

F Varchon, R Feng, J Hass, X Li, B N Nguyen, C Naud, P Mallet, J Y Veuillen, C Berger, E H Conrad, and L Magaud. Electronic structure of epitaxial graphene layers on SiC: effect of the substrate. *arXiv.org*, 2007.

B M Venkatesan and R Bashir. Nanopore sensors for nucleic acid analysis. *Nature Nanotechnology*, 6(10):615–624, 2011.

P Wang, D Zhang, L Li, Z Li, L Zhang, and Y Fang. Reversible Defect in Graphene Investigated by Tip-Enhanced Raman Spectroscopy. *Plasmonics*, pages 1–7, 2012.

W H Weber and R Merlin. Raman Scattering in Materials Science. *Springer*, page 316, 2000.

B Yeo, J Stadler, T Schmid, R Zenobi, and W Zhang. Tip-enhanced Raman Spectroscopy - Its status, challenges and future directions. *Chemical Physics Letters*, 472(1-3):1–13, 2009.

B S Yeo, T Schmid, W Zhang, and R Zenobi. Towards rapid nanoscale chemical analysis using tip-enhanced Raman spectroscopy with Ag-coated dielectric tips. *Analytical And Bioanalytical Chemistry*, 387(8):2655–2662, 2007.

R Zenobi and V Deckert. Scanning near-field optical microscopy and spectroscopy as a tool for chemical analysis. *Angewandte Chemie International Edition*, 39:1746–1756, 2000.

W Zhang, B S Yeo, T Schmid, and R Zenobi. Single Molecule Tip-Enhanced Raman Spectroscopy with Silver Tips. *Journal Of Physical Chemistry C*, 111(4):1733–1738, 2007.

Y H Zhang, Y B Chen, K G Zhou, C H Liu, J Zeng, H L Zhang, and Y Peng. Improving gas sensing properties of graphene by introducing dopants and defects: a first-principles study. *Nanotechnology*, 20(18):185504, 2009.

J Zhao, C He, R Yang, Z Shi, M Cheng, W Yang, G Xie, D Wang, D Shi, and G Zhang. Ultra-sensitive strain sensors based on piezoresistive nanographene films. *Applied Physics Letters*, 101(6):063112–063112, 2012.

Y Zhu, W Cai, R D Piner, A Velamakanni, and R S Ruoff. Transparent self-assembled films of reduced graphene oxide platelets. *Applied Physics Letters*, 95(10):103104–103104–3, 2009.

I Zsoldos. Effect of topological defects on graphene geometry and stability. *Nanotechnology, Science and Applications*, 3:101–106, 2010.